CHEMICAL REVIEWS

Review

pubs.acs.org/CR

Small Angle X-ray Scattering for Nanoparticle Research

Tao Li, Andrew J. Senesi, and Byeongdu Lee*

X-ray Science Division, Argonne National Laboratory, 9700 South Cass Avenue, Lemont, Illinois 60439, United States

ABSTRACT: X-ray scattering is a structural characterization tool that has impacted diverse fields of study. It is unique in its ability to examine materials in real time and under realistic sample environments, enabling researchers to understand morphology at nanometer and angstrom length scales using complementary small and wide angle X-ray scattering (SAXS, WAXS), respectively. Herein, we focus on the use of SAXS to examine nanoscale particulate systems. We provide a theoretical foundation for X-ray scattering, considering both form factor and structure factor, as well as the use of correlation functions, which may be used to determine a particle's size, size distribution, shape, and organization into hierarchical structures. The theory is expanded upon with contemporary use cases. Both transmission and reflection (grazing incidence) geometries are addressed, as well as the combination of SAXS with other X-ray and non-X-ray characterization tools. We conclude with an examination of several key areas of research where X-ray scattering has played a pivotal role, including in situ nanoparticle synthesis, nanoparticle assembly, and operando studies of catalysts and energy storage materials. Throughout this review we highlight the unique capabilities of X-ray scattering for structural characterization of materials in their native environment.

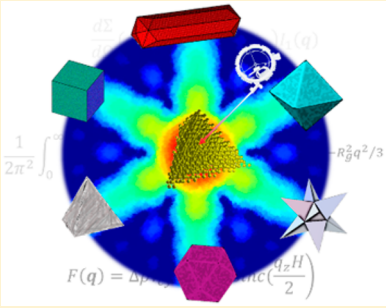

CONTENTS

1. Introduction B
2. Data Measurement and Processing B
2.1. Data Reduction C
2.2. Background Subtraction C
2.3. Absolute Intensity Calibration C
2.4. Software Packages for SAXS Analysis D
3. Particle Scattering D
3.1. General Theory D
3.2. Form Factor Analysis E
3.2.1. Form Factor of Solid Particles E
3.2.2. Particle Size Distribution Analysis F
3.2.3. Guinier, Porod, and Invariant Analysis H
3.2.4. Model Analysis: Morphology I
3.3. Structure Factor Analysis L
3.3.1. Pair Distribution Function L
3.3.2. Isotropic Homogenous Liquid-Like Structures M
3.3.3. Isothermal Compressibility N
3.3.4. Crystalline Assemblies N
3.3.5. Structure Determination O
3.3.6. Peak Shape Analysis P
3.4. Limited-Sized Structures P
3.4.1. Supraparticles or Particle Clusters P
3.4.2. Porous Particles S
3.4.3. Aggregates S
4. Correlation Function Approach T
4.1. Correlation Function from Experimental Data U
4.1.1. Comparing Correlation Function with Simulations U
4.1.2. Model Analysis with Atomic PDF U
4.2. Particle Positional Correlation Analysis V
4.3. Analytical Correlation Function Model V
4.3.1. Arbitrary Shaped Particles V
4.3.2. Fractal Particles W
4.3.3. Correlation Functions with Structure Factor W
5. Combination of Scattering with Model Simulations W
5.1. SAXS Simulation Using Atomistic Models W
5.2. SAXS and WAXS: Total Scattering Simulations X
6. GISAXS X
6.1. Reflection and Refraction in GISAXS X
6.2. Indexing with Two-Beam Diffraction Y
6.3. Distorted Wave Born Approximation (DWBA) Analysis Z
6.3.1. Two-Dimensional (2D) Structures Z
6.3.2. Three-Dimensional (3D) Superlattices AA
7. Applications AB
7.1. Colloidal Nanoparticle Synthesis AB
7.1.1. SAXS Analysis Tools AC
7.1.2. Experimental Techniques for In Situ Measurements AC
7.1.3. Early Stage: Nucleation and Growth of Nanoparticles AE
7.1.4. Later Stage: Ostwald Ripening vs Smoluchowski Aggregation AF
7.2. Nanoparticle Assembly AF
7.2.1. Assemblies Controlled by Soft Materials AG

Special Issue: Nanoparticle Chemistry

Received: November 26, 2015

 © XXXX American Chemical Society

DOI: 10.1021/acs.chemrev.5b00690
Chem. Rev. XXXX, XXX, XXX−XXX

7.2.2. Assemblies Formed through Solvent Evaporation AJ
7.3. Operando Characterization Using in Situ SAXS and Combined Techniques AL
7.3.1. Fuel Cells AL
7.3.2. Heterogeneous Catalysts AM
7.3.3. Battery Electrodes AN
8. Conclusion and Outlook AN
Author Information AN
Corresponding Author AN
Notes AN
Biographies AN
Acknowledgments AO
References AO

1. INTRODUCTION

The structural characterization of nanoscale systems is an intensively active area of research, enabling numerous fundamental studies and technological advances in a variety of scientific disciplines.[1−7] These systems can be studied with real space imaging or reciprocal space scattering techniques. Like electron microscopy, X-ray scattering makes use of the variation of a sample's electron density to generate contrast. Both techniques provide the same information; however, the former yields real space images while the latter provides reciprocal space data. As "reciprocal" implies, a spatial variation of electron density at nanometer length scales will scatter an X-ray beam to low angles while that in the atomic scale will scatter to high angles. Small angle X-ray scattering (SAXS) is a therefore a technique to study material structures at large distances, or small angles. Conversely, wide angle X-ray scattering (WAXS) is used to measure the scattering intensity at large angles, or small distances.

Nanoscale density variation may stem from a variety of sources, including suspensions of colloidal particles,[8] thermal density fluctuation in liquids,[9] microphase separated block copolymers,[10] porous materials,[11] or periodic arrangements of nanoparticles.[12] Such characterization has played a key role in the analysis of complex fluids,[13] polymers,[14] heterogeneous catalysts,[15] and biological systems.[16] In this review, we have chosen to focus on the use of X-ray scattering, in particular SAXS, for the characterization of nanoparticle systems. We aim to provide a theoretical and technical foundation for the use of SAXS and WAXS, and provide a contemporary review of state-of-art nanoparticle research using SAXS. When appropriate, complementary scattering techniques such as small angle neutron scattering (SANS) or the combination of SAXS with other X-ray and non X-ray characterization tools will be discussed. For these reasons, this review is primarily intended for those interested in using X-ray scattering for nanoscale characterization.

SAXS has been used to study nanoparticles since the dawn of the technique in the 1950s.[17] In those early days, the term "nanoparticle" was not yet invented; nanoparticles dispersed in solvent were referred to colloidal materials. The first SAXS data on monodisperse metal particles was in fact reported in 1951 by Turkevich and co-workers, not surprisingly on a sample called "colloidal gold" or "gold sol" synthesized via the Turkevich reaction.[18] In this historical context, SAXS treatment of colloidal particles has typically considered nanoparticles to be solid objects with simple mathematical shapes, not much more complex than a sphere, ellipsoid, or rod. At the individual particle level, SAXS is an immensely powerful method to determine an object's size, size distribution, shape, and surface structure.[19] In addition, it is useful to determine the relative positions of particles, from which one may infer their pair potential and, further, the equations of state.[20,21] The definition of a particle in SAXS is somewhat broader than the nanoparticle or nanocrystal often used in the nanoscience community. Thus, SAXS has been frequently used to study other types of particles such as aerosols, micelles, minerals and particles synthesized through sol−gel reactions, etc.[22] Because SAXS measures only the electron density difference, a nanopore can be regarded as an "inverse" nanoparticle, allowing one to adapt the same principles and theory for colloidal particles to examine nanoporous structures.[23] The definition of a particle for SAXS can then be unified under a broader concept of morphology, meaning that it is not the composition of the material but its structure that is used to classify particulate and nonparticulate systems.

In recent years, the development of synchrotron X-ray sources with high flux and high energy, as well as new detectors, has led to the increasing popularity of X-ray scattering for nanoparticle research.[24] It is instructive to compare SAXS to other characterization techniques, such as transmission electron microscopy (TEM). TEM is limited in terms of analysis area, and is not suitable for bulk measurements. Further, there is a tendency in TEM toward sample bias, or the selection of a single nice image as a representation of the entire sample. In contrast, SAXS is nondestructive, and provides structural data averaged over macroscopic sample volumes.[25] Because of the tunable flux and energy at modern synchrotrons, SAXS is also capable of structural characterization in realistic sample conditions.[15] This is of particular importance for nanoparticle research, where SAXS is routinely used to study colloidal systems in their native, solution environments, which can be challenging using TEM. When combined with short (pico-seconds to seconds) data collection times, SAXS becomes ideally suited for in situ or operando experiments.

Herein we intend to show how SAXS is uniquely positioned to study nanoparticle systems in their native environments. We begin with a discussion of transmission SAXS, briefly outlining data acquisition and processing in section 2. In sections 3 and 4, we review the theory of scattering, breaking our discussion into an analysis of colloidal SAXS form factor and structure factor, as well as the correlation function approach, respectively. Examples of common types of data analysis will be described. In section 5, we will introduce works that integrate computer simulation with SAXS data analysis. The scattering in reflection mode, or grazing incidence geometries (GISAXS), is an important and growing area of research for the examination of nanostructured films, and will be addressed in section 6. In section 7, we review several key areas of research where SAXS has been influential, including in situ nanoparticle synthesis, nanoparticle assembly, and operando studies of catalysts and energy storage materials.

2. DATA MEASUREMENT AND PROCESSING

SAXS beamlines are typically equipped with multiple types of detectors. This includes a two-dimensional (2D) area detector and at least two beam monitors, m_1 and m_2 (see Figure 1). The upstream beam monitor, m_1, is used to correct for any variation of incoming flux, while the downstream monitor, m_2, is typically mounted on the beamstop and is used to normalize the transmittance of the sample.

DOI: 10.1021/acs.chemrev.5b00690
Chem. Rev. XXXX, XXX, XXX−XXX

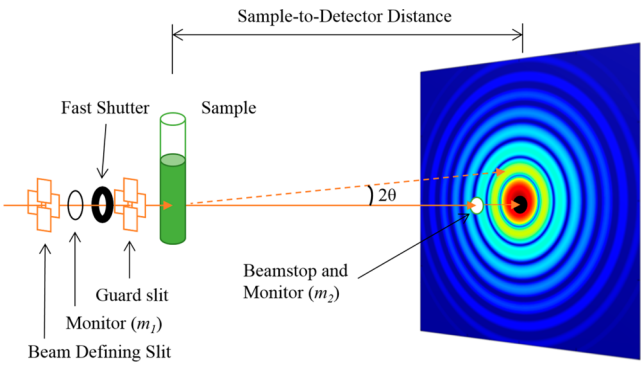

Figure 1. Schematic for the optical components of the 12ID-B SAXS beamline at the Advanced Photon Source (APS).

The 2D area detector is used to collect the angle-resolved SAXS signal that is elastically scattered (that is, without any change in wavelength) by the sample. Standard calibrants should be measured each time the setup is changed, including silver behenate[26] to determine the sample-to-detector distance, and glassy carbon[27] or water[28] to determine the absolute intensity.

2.1. Data Reduction

Once the scattering signal is collected on the 2D detector, a series of standard 2D data correction procedures may be performed, depending on the type of detector used. These include dark current subtraction, image distortion and linearity correction, and flat field correction. Next, the position of each pixel on the SAXS image is converted into the scattering angle 2θ or the scattering vector $\boldsymbol{q}$ (its modulus is $q = 4\pi \sin(\theta)/\lambda$, where λ is the wavelength of the X-ray) with the choice of an appropriate coordinate system. This conversion is accomplished using experimental parameters that include the sample-to-detector distance (often abbreviated SDD) and the pixel size of the detector. For an image that is isotropic along the azimuthal direction, polar coordinates are typically used. This is applicable to the majority of nanoparticle systems in solution, as they are typically randomly oriented and therefore have isotropic scatterings (Figure 1). The 2D images are then azimuthally averaged to give a one-dimensional (1D) scattering curve. When the image is no longer isotropic along the azimuthal direction, it may be represented in other coordination systems such as Cartesian[3] or ellipsoidal polar,[29] depending on the orientation of the nanostructures. Linecuts of the data may then be taken to yield 1D scattering curves. Additional details of this procedure are found in a recent review.[30]

2.2. Background Subtraction

In a typical SAXS experiment, the count value on a pixel of the 2D detector, J, or the 1D averaged data is typically normalized by the value of the second beam monitor, m_2, located downstream of the sample

$$\frac{J}{m_2} \equiv I \tag{1}$$

where counts on both detectors are collected for a given exposure time. The data I contains a background signal that originates primarily from air, the beamline optics including the X-ray windows, and the sample cell. This contribution can be removed by subtracting the scattering intensity of the empty container, I_{cell}, from that of the sample in the same container, $I_{sample/cell}$.

$$I_{sample} = I_{sample/cell} - I_{cell} \tag{2}$$

When particles are dispersed in a solvent, the scattering contribution from the particles can be obtained as

$$I_{particle} = I_{particle/solv} - \phi_{solv} I_{solv} \tag{3}$$

where ϕ_{solv} is the volume fraction of solvent. $I_{particle/solv}$ and I_{solv} are the scattering intensities, corrected for the empty cell scattering, of solution and solvent, respectively. For a dilute solution, ϕ_{solv} is assumed to be 1, and thus

$$I_{particle} = I_{particle/solv/cell} - I_{solv/cell} \tag{4}$$

One typical example of background subtraction for solution SAXS is displayed in Figure 2.

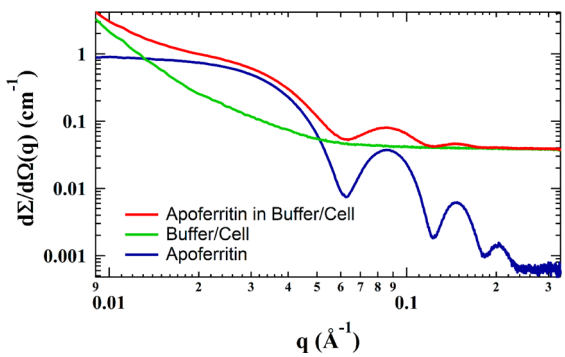

Figure 2. SAXS data of 10 mg/mL apoferritin on an absolute intensity scale. Apoferritin is a protein cage with a diameter of 12 nm. Apoferritin in buffer in a quartz capillary (red), buffer in the same quartz capillary (green), and background subtracted data (blue).

2.3. Absolute Intensity Calibration

The units of I are arbitrary, but it is a quantity proportional to the number of X-ray photons arriving at a particular pixel of the 2D detector. It is therefore possible to convert I into absolute intensity units with the help of a known absolute intensity calibration sample such as a glassy carbon[27] or water.[28] When the background subtracted intensity I for a standard sample with thickness d_S at a given scattering angle is I_S, and its precalibrated absolute intensity is $\frac{d\Sigma}{d\Omega_S}$, the intensity of a sample in absolute units, $\frac{d\Sigma}{d\Omega}$ is then

$$\frac{d\Sigma}{d\Omega}(\boldsymbol{q}) = \frac{d\Sigma}{d\Omega_S} \frac{d_S I(\boldsymbol{q}) m_{1S}}{d I_S m_1} \tag{5}$$

where d is the thickness of the sample. Equation 5 makes use of the value of the first monitor located upstream of the sample, m_1. Here, m_{1S} is the monitor value obtained when the standard sample is measured. The differential cross section $\frac{d\Sigma}{d\Omega}$ is given in units of cm^{-1}. When it is not necessary to describe scattering intensity in absolute units, we will use $I(\boldsymbol{q})$ instead of $\frac{d\Sigma}{d\Omega}(\boldsymbol{q})$.

There is significant benefit in determining the absolute scattering intensity of nanoparticle systems. For example, the concentration of nanoparticles can be obtained, which can then be used for a variety of experiments. This can include determining molar extinction coefficients, the porosity of a sample, or the fraction of precursor reactants that are reduced

DOI: 10.1021/acs.chemrev.5b00690
Chem. Rev. XXXX, XXX, XXX−XXX

during in situ nanoparticle synthesis. See section 7.1 and subsections therein for several applications using absolute intensity for nanoparticle research.

2.4. Software Packages for SAXS Analysis

There are numerous software packages available for a variety of applications related to SAXS. Most of them can be found online for free and are open source or run on platforms such as Igor Pro and MATLAB. These packages are typically designed for specific purposes. For example, Fit2D[31] or Nika[32] may be used for data reduction (section 2.1). Many beamlines also have their own software packages for data reduction. Form factor analysis (section 3.2.4) can be performed using SASfit,[33] Irena,[34] WillItFit,[35] Scatter,[36] or SasView.[37] Each may be better suited for different particle morphologies such as anisotropic shapes or core−shell structures. Solution SAXS profiles can also be calculated if atomic coordinates are known, for example from the Protein Data Bank, using software programs such as Crysol[38] (section 5.1). Ab initio structural refinement algorithms to determine the shape of a protein molecule using a molecular envelope have also been developed.[16] Structure factor analysis (section 3.3) including indexing and model fitting may be performed with several software packages such as simSAXSLee,[39] Irena,[34] or Scatter.[36] For GISAXS analysis, GIXSGUI,[40] IsGISAXS,[41] GISAXSshop,[42] or FitGISAXS[43] may be used for analysis and modeling of both form and structure factors (section 6). This is not a comprehensive list, but it can provide a starting point for those who are just becoming acquainted with SAXS. For a more comprehensive discussion of SAXS software packages, we refer the interested readers to several Web sites.[44,45]

3. PARTICLE SCATTERING

A typical SAXS profile depicting spherical particles in a solution is shown in Figure 3. As we will show, the profile can be split into two components, including (1) the form factor, which provides information regarding the mean structural properties of the individual particles (i.e., size and shape), and (2) the structure factor, which provides the positional correlation of the particles. In the following section, we briefly review basic X-ray scattering theories that can be used to analyze the SAXS profile, discussing both form factor and structure factor.

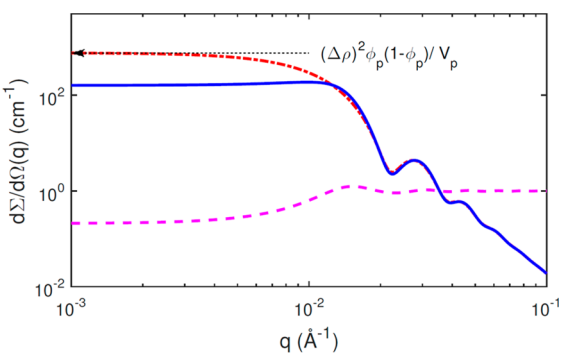

Figure 3. Simulated SAXS intensity of polydisperse spheres with 10% polydispersity using a Schultz−Zimm size distribution function. The absolute intensity $d\Sigma/d\Omega(q)$ is shown as a blue solid line, and the form factor $P(q)$ scaled to $d\Sigma/d\Omega(q)$ is shown as a red dash−dotted line. The structure factor $S(q)$ is shown as a magenta dashed line. The particle mean radius is 20 nm, the volume fraction is 0.2, $\Delta\rho/r_e = 0.04$ Å^{-3}, and the calculated mean particle volume $V_p = 3.452 \times 10^4$ nm^3.

3.1. General Theory

According to SAXS theory, the scattering from N_p identical particles in a volume V is given as

$$\frac{d\Sigma}{d\Omega}(\boldsymbol{q}) = \frac{\phi_p(1-\phi_p)}{V_p} I_1(\boldsymbol{q}) \tag{6}$$

where ϕ_p and V_p are the volume fraction of particles and the volume of an individual particle, respectively. The quantity q is the modulus of the scattering vector $\boldsymbol{q}$.

$$I_1(\boldsymbol{q}) = \frac{1}{N_p}\left|\sum_{l=1}^{N_p} F_l(\boldsymbol{q}) e^{-j\boldsymbol{q}\boldsymbol{r}_l}\right|^2 \tag{7}$$

where $F_l(\boldsymbol{q})$ and $\boldsymbol{r}_l$ are the form factor amplitude and position of particle l, respectively. The exponential term $e^{-j\boldsymbol{q}\boldsymbol{r}_l}$ is called the phase factor and $I_1(q) = \langle I_1(\boldsymbol{q})\rangle$, where $\langle\,\rangle$ denotes the orientational average. When particles are randomly oriented, $\frac{d\Sigma}{d\Omega}(q) = \left\langle \frac{d\Sigma}{d\Omega}(\boldsymbol{q})\right\rangle$ is used.

For a dilute concentration,[17] $1 - \phi_p \approx 1$ and $\frac{\phi_p}{V_p} = \frac{N_p}{V} \equiv f_p$, which is the particle number density. Thus, eq 6 becomes

$$\frac{d\Sigma}{d\Omega}(\boldsymbol{q}) = f_p I_1(\boldsymbol{q}) \tag{8}$$

For a set of particles whose positions are known, $I_1(\boldsymbol{q})$ can be simply calculated with eq 7. When the particles have a spherical symmetry like an atom, the orientational average of eq 7 may be performed analytically, yielding

$$I_1(q) = \frac{1}{N_p}\sum_{l=1}^{N_p}\sum_{l'=1}^{N_p} F_l(q)\, F_{l'}(q)\frac{\sin(qr_{ll'})}{qr_{ll'}} \tag{9}$$

where $r_{ll'}$ is the distance between the lth and l'th particles. Equation 9 is called the Debye formula.

The form factor amplitude $F(\boldsymbol{q})$ of a geometric object like a nanoparticle can be either analytically or numerically calculated. By definition[17,25]

$$F(\boldsymbol{q}) = \int_V \Delta\rho(\boldsymbol{r}) e^{-i\boldsymbol{q}\boldsymbol{r}}\, d\boldsymbol{r} \tag{10}$$

where $\Delta\rho(\boldsymbol{r}) = \rho(\boldsymbol{r}) - \tilde{\rho}$, and $\rho(\boldsymbol{r})$ and $\tilde{\rho}$ are the scattering length density at position $\boldsymbol{r}$ and the mean scattering length density of the solution, respectively. For X-rays the scattering length density is $r_e\rho_e(\boldsymbol{r})$, where r_e is the classical electron radius, 2.818×10^{-5} Å, and $\rho_e(\boldsymbol{r})$ is the electron density at position $\boldsymbol{r}$. Here, the center-of-mass position of the particle is at the origin of the coordinate system. This equation dictates that $F(\boldsymbol{q})$ is the Fourier transform of $\Delta\rho(\boldsymbol{r})$. For a dilute solution, when the differential cross section is defined as in eq 6, $\Delta\rho(\boldsymbol{r}) = \rho(\boldsymbol{r}) - \rho_s$, where ρ_s/r_e is the solvent electron density. The units of electron density are Å^{-3}.

When a particle has a uniform scattering length density with ρ in the resolution of small angle scattering, called the solid object in this review, $\Delta\rho = \rho - \rho_s$ and then

$$F(\boldsymbol{q}) = \Delta\rho \int_V e^{-i\boldsymbol{q}\boldsymbol{r}}\, d\boldsymbol{r} \tag{11}$$

where the volume integral is called the particle shape function $\Sigma(\boldsymbol{q})$ as

DOI: 10.1021/acs.chemrev.5b00690
Chem. Rev. XXXX, XXX, XXX−XXX

$$\int_V e^{-i\boldsymbol{q}\boldsymbol{r}}\, d\boldsymbol{r} \equiv \Sigma(\boldsymbol{q}) \tag{12}$$

When the center-of-mass position of the particle is at position $\boldsymbol{X}$, a phase factor $e^{-i\boldsymbol{q}\boldsymbol{X}}$ must be multiplied to $F(\boldsymbol{q})$. The form factor $P(\boldsymbol{q}) = |F(\boldsymbol{q})|^2$ and

$$P(q) = \langle |F(\boldsymbol{q})|^2 \rangle \tag{13}$$

For a solid object, $P(q) = (\Delta\rho)^2 \langle |\Sigma(\boldsymbol{q})|^2 \rangle$.

When the relative positions of the particles are random, for example when they are in a dilute solution, the interference between the scatterings from two different particles is neglected, as is the phase factor. When the particles come closer to each other for any reason, perhaps because their concentration increases or there is some attractive interaction, their relative interparticle distance may no longer be random. For example, when all N_p particles are identical, eq 7 becomes

$$I_1(\boldsymbol{q}) = \frac{1}{N_p} P(\boldsymbol{q}) \left| \sum_{l=1}^{N_p} e^{-j\boldsymbol{q}\boldsymbol{r}_l} \right|^2 \tag{14}$$

and the sum of the absolute square of the phase factor is defined as the structure factor:

$$S(\boldsymbol{q}) = \frac{1}{N_p} \left| \sum_{l=1}^{N_p} e^{-j\boldsymbol{q}\boldsymbol{r}_l} \right|^2 \tag{15}$$

Then

$$S(q) = 1 + \frac{1}{N_p} \langle \sum_{l=1}^{N_p} \sum_{l' \neq 1}^{N_p} e^{-j\boldsymbol{q}(\boldsymbol{r}_l - \boldsymbol{r}_{l'})} \rangle \tag{16}$$

where the second term on the right is called the interference function $i(q)$.

$$S(q) = 1 + i(q) \tag{17}$$

The interference function $i(q)$ vanishes to 0 when the distances between any two particles $(\boldsymbol{r}_l - \boldsymbol{r}_{l'})$ are random, as in the case of a dilute solution of particles.

Finally, for identical particles with spherical symmetry, $P(q) = P(\boldsymbol{q})$ and thus

$$I_1(q) = P(q)\, S(q) \tag{18}$$

When particles are neither identical nor spherical objects, ideally speaking, it is not possible to split the intensity into a product of the form factor and the structure factor as in eq 18 without the help of commonly used approximations. Note that according to eq 14, in vector format $S(\boldsymbol{q}) = I_1(\boldsymbol{q})/P(\boldsymbol{q})$, but $S(q)$ is not necessarily $I_1(q)/P(q)$. These include the decoupling of position and individual particle properties, such as size and shape, known as the decoupling approximation (DA)[17,46] and local monodisperse approximation (LMA).[47] The former assumes that particles' intrinsic properties, such as size and shape, are not correlated with their positions, and the latter assumes that, at short ranges, all particles are identical. While both approximations have been successfully used in the literature, the latter may not be appropriate in the description of crystalline assemblies where binary particles can form a crystal.[39] However, the DA has its own limitations. It often overestimates diffuse scattering for polydisperse, binary, or polyhedral particles.[39,47−49] In addition, when the particles have some attractive potential, such as entropic interactions,[50−53] charge,[54−56] or (bio)chemical recognition,[54,57,58] particles may segregate according to size or shape,[56,59−61] suggesting that in this case the LMA may be more appropriate. Uses of the DA and LMA are found in section 3.3.

3.2. Form Factor Analysis

Nanoparticles, either naturally occurring or synthesized in the lab, typically have some finite size distribution. They also have some type of shape. The analysis of SAXS spectra then typically begins with form factor analysis to understand these intrinsic physical characteristics of the particles. As will be discussed, the analysis of SAXS spectra typically requires some type of prior sample knowledge to impart one or more constraints; a given spectrum may have multiple solutions if one allows for all possible combinations of particle shape and size. In this section, we discuss methods to determine the size distribution followed by processes to analyze morphology. In general, there are two pathways to analyze particle morphologies from form factor scattering. The first is an empirical process that seeks to understand the asymptotic behavior of SAXS spectra using Guinier and Porod laws, as well as integral quantities. The second makes use of direct model analysis to find a best fit of the data. New methods including shape reconstruction are of interest and will be discussed in the following subsections.

3.2.1. Form Factor of Solid Particles. SAXS is an extraordinarily useful tool for structural characterization of nanoparticles in their native environment. To determine the size and shape of a particle sample from scattering data, one typically takes a model dependent approach that assumes a particular form of the form factor scattering.

3.2.1.1. Geometrically Simple Particles. For a spherical particle whose center of mass is at the origin with radius R, its form factor is

$$F(q) = \Delta\rho V_{sp} \frac{3(\sin(qR) - qR\cos(qR))}{(qR)^3} \tag{19}$$

where $V_{sp} = 4\pi R^3/3$ and $\Delta\rho = \rho_p - \rho_s$. The subscripts "p" and "s" stand for particle and solvent, respectively. Note that the sphere scattering is only dependent on the magnitude of $\boldsymbol{q}$ because it scatters isotropically (Figure 4a,c). When a cylinder whose center of mass is at the origin is oriented parallel to z, its form factor is calculated as

$$F(\boldsymbol{q}) = 2\Delta\rho V_{cy} J_1(q_{||}R)\, \mathrm{sinc}\left(\frac{q_z L}{2}\right) \tag{20}$$

and $V_{cy} = \pi R^2 L$, where R and L are the radius and height of the cylinder, respectively. J_1 is the first order Bessel function, $\mathrm{sinc} = \sin(x)/x$, $q_{||} = \sqrt{q_x^2 + q_y^2}$, and q_x, q_y, and q_z are x, y, and z direction components of $\boldsymbol{q}$. Because a cylinder is anisotropic, its radial and axial scattering will be different (Figure 4b). For randomly oriented particles in solution, orientational average must be applied to eq 20 through eq 13 to make a direct comparison with the scattering data (Figure 4d). Form factors of other simple shaped objects such as ellipsoids, cubes, thin rods, thin plates, and so on are well documented.[25,62] Numerous software programs providing various form factor models are available.[33−35]

3.2.1.2. Polyhedral Particles. Recently, methods to calculate the form factors of polyhedral shapes were proposed by Li et al.[63] for platonic solids, and us[64] for more general polyhedra including regular or semiregular polyhedral particles and ones that have been truncated or stellated from those "mother"

DOI: 10.1021/acs.chemrev.5b00690
Chem. Rev. XXXX, XXX, XXX−XXX

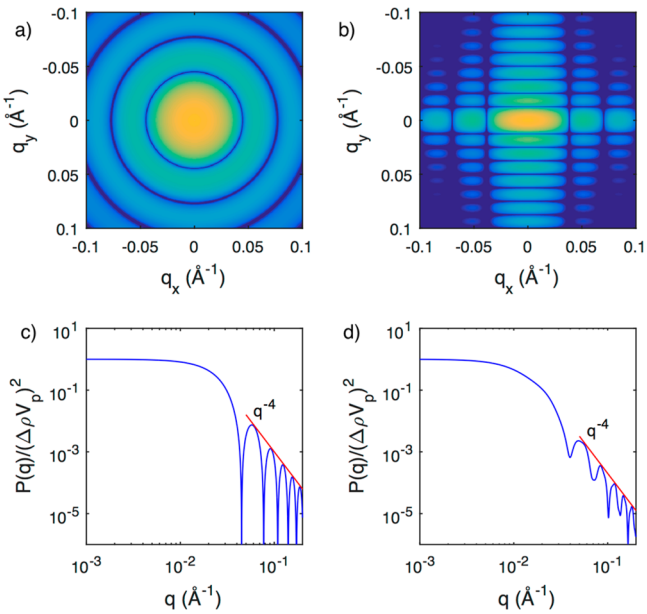

Figure 4. Two-dimensional (2D) scattering images (intensities are in log scale) of (a) sphere and (b) cylinder, where the axis of the cylinder is parallel to the *y*-axis. The 1D SAXS curves in (c) and (d) are the scatterings from randomly oriented spheres and cylinders, respectively. Intensities are normalized so that $P(0) = 1$. The radius of the sphere is 10 nm, and the radius and length of the cylinder are 10 and 50 nm, respectively.

polyhedra. Significantly, our results suggested that the periodicity of the form factor oscillation of a polyhedral particle is inversely proportional to the distance between its parallel faces (Figure 5). Therefore, polyhedral particles without

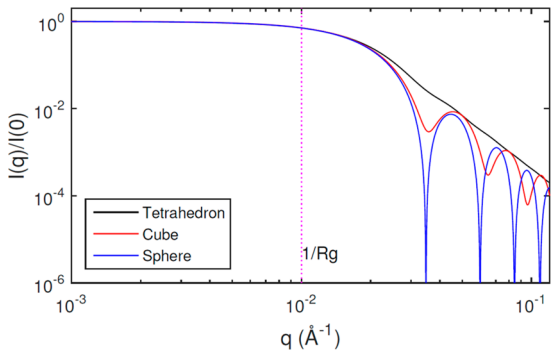

Figure 5. Normalized SAXS curves of a sphere, cube, and tetrahedron with the same radius of gyration, R_g (10 nm). The R_g of each particle is calculated from ref 71.

parallel faces, such as tetrahedra, do not present a form factor oscillation. This information can be helpful in determining particle shape from SAXS data.[64] When computational speed does not matter, it is possible to compute the scattering of any particle shape using the Debye formula (eq 9)[65,66] from a set of atomic coordinates,[67] vertices and faces,[68] or the Monte Carlo method.[69,70]

3.2.1.3. Shape Reconstruction. The shape of a single particle has been reconstructed from coherent SAXS data.[72−74] Here, the particle is fixed in space without rotation or translation. The use of a coherent X-ray beam can help to determine the phase of F($\boldsymbol{q}$), the amplitude of which is the square root of the measured intensity I($\boldsymbol{q}$).[73] Then, the real space structure or $\Delta\rho$ can be obtained from the inverse Fourier transform of eq 10. Barke et al. experimentally verified the 2D scattering of a single Ag nanoparticle by directly comparing experimental data with calculated 2D scattering images, including particles with 5-fold symmetry and anisometric shapes.[74] Takahashi et al. reconstructed a three-dimensional (3D) electron density map of 200 nm size Ag/Au core−shell nanoparticles from a series of 2D SAXS data with a resolution of 4.2 nm. Not only surface structures such as small pits, but also internal density distributions, for example the Au-rich region, were clearly identified.[75] Robinson et al. have shown that stress distribution in a nanocrystal can be determined by analyzing the shape of a given WAXS diffraction peak using a coherent X-ray beam. The fine features around the diffraction peak are similar to the SAXS around the direct beam.[76] Watari and Robinson et al. later studied 300 nm size faceted gold nanoparticles with the same technique and showed that lattice contraction occurs due to adsorption of propanethiols, as determined by monitoring the gold nanoparticle [111] diffraction peak before and after thiol dosing.[77]

There is also a method to retrieve the shape of a particle from typical solution SAXS data without using a coherent beam; however, it is often of lower resolution than coherent SAXS. This method assumes that the particles in solution are identical in size and shape, and are randomly oriented. This assumption has been accepted for biological molecules such as proteins and RNA, but may or may not be true for synthetic nanoparticle systems depending on polydispersity. The ab initio model-free shape retrieval method, called DAMMIN, developed by Svergun,[16,78] has been successfully used to calculate the shape functions of biological particles. This method utilizes a dummy atom model to fit SAXS data or the pair distance distribution function outlined in section 4.1. The envelop function, or low-resolution shape of a protein, often provides good agreement with the overall shape of the atomic crystal structure. There is also a reconstruction algorithm based on a Monte Carlo method.[79] These two approaches attempt to reconstruct the 3D shape of molecules or particles, though they suffer from the loss of some detailed information regarding particle shape due to orientational averaging. There are efforts to overcome this shortcoming, e.g. by combining SAXS with other complementary techniques[16] or computer simulations.[80] Encouragingly, there have been efforts to apply these methods to nanocrystal systems.[81,82]

3.2.2. Particle Size Distribution Analysis. Different decoupling approximations, DA and LMA, discussed in section 3.1 lead to different forms of the structure factors (see, e.g., section 3.3.4 or ref 47); however, in either case the form factor is defined as

$$P(q) = \int n(R)\langle |F(\boldsymbol{q}, R)|^2\rangle \, dR \tag{21}$$

where R is the radius (or edge length for a polyhedral particle), $n(R)$ is the size distribution function, and $\int n(R)\, dR = 1$. Mathematically, when attempting to fit the form factor from scattering data, either $n(R)$ or $F(\boldsymbol{q},R)$ (that is particle shape) must be known. If one assumes a functional form of $F(\boldsymbol{q},R)$ (typically irregular shaped particles are assumed to be spherical), there are several methods to determine the size distribution function, including either model dependent or model independent paths. The most common approach is model dependent, by assuming a functional form for $n(R)$. Often, the Schultz−Zimm distribution function is used, which

DOI: 10.1021/acs.chemrev.5b00690
Chem. Rev. XXXX, XXX, XXX−XXX

allows analytical integration of eq 21.[83] The Schultz–Zimm distribution function is

$$n(R) = \frac{\left(\frac{z+1}{R_0}\right)^{z+1} R^z}{\Gamma(z+1)} \exp\left(-\frac{z+1}{R_0}R\right) \tag{22}$$

where $z = (R_0/\sigma)^2 - 1$. Two parameters, R_0 and σ, are the number-averaged radius and root-mean-square deviation of the size distribution, respectively. Figure 6 shows the variation of the form factor scattering as a function of polydispersity (σ/R), clearly showing how the form factor oscillations smear out as size polydispersity increases. Borchert et al. compared TEM, SAXS, and XRD peak width analysis for CoPt nanoparticles with about 8% polydispersity and confirmed they all agree very well.[84] Other size distribution functions such as log-normal distributions and Gaussian distributions can be used. It is worth noting that the Schultz–Zimm distribution is identical to a Gaussian function when its width is narrow and becomes asymmetric as its width gets broader. If any functional form is available, i.e. from some nucleation and growth theory, it can be used as well, as shown in section 7.1.4.

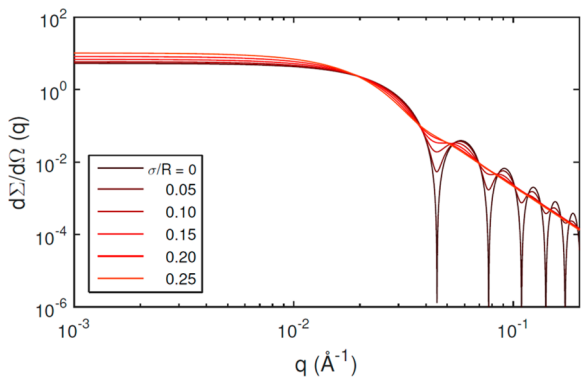

Figure 6. Form factor scatterings of spherical particles with varying degree of polydispersity. The radius is 10 nm, volume fraction is 0.01, and $\Delta\rho/r_e = 0.04$ Å^{-3}. A rule of thumb is that when the particles have a size polydispersity of ≥15%, the form factor oscillations smear out.

There are several model independent methods to obtain the size distribution including the indirect Fourier transform method using Glatter's approach[85,86] or the maximum entropy approach.[85] A Monte Carlo method has also been developed.[87] These methods become more useful as the size distribution broadens or is multimodal.[85] Wang et al.[88] used a method based on the Guinier approximation developed by Jellineck and Fankuchen.[89] When particles are highly polydisperse, a Guinier plot will show a curvature instead of a straight line. By applying Guinier fits along the tangential of the Guinier plot, the relative number of particles can be obtained from $d\Sigma/d\Omega(0)$ values. This method is in principle a conversion of a curvature in a Guinier plot to the size distribution. Since the Guinier law is used, this method does not assume a particular particle shape. Examples of these analyses are found later in sections 7.1 and 7.2.2.1.

3.2.2.1. Statistical Quantities from the Size Distribution Function. In general, for a polydisperse system, $d\Sigma/d\Omega(0)$ is

$$\frac{d\Sigma}{d\Omega}(0) = (\Delta\rho)^2 \phi_p (1-\phi_p) \frac{\overline{V_p^2}}{\overline{V_p}} \tag{23}$$

Thus, it is clear that SAXS intensity varies as a function of particle concentration and size. The data from SAXS provides statistical mean values of the sample irradiated by the X-ray beam. Once the size distribution is determined, these mean values can be computed from the distribution. For example, for a system of polydisperse spheres with a certain size distribution function,[83] it is possible to calculate mean quantities analytically as below:

The radius of gyration is

$$R_g = \sqrt{\frac{3R_8R_7}{5}} \tag{24}$$

The mean surface area of the particles is

$$\overline{S_p} = 4\pi R_2 R_1 \tag{25}$$

The mean volume of the particles is

$$\overline{V_p} = \frac{4\pi}{3} R_3 R_2 R_1 \tag{26}$$

The mean square of the particle volumes is

$$\overline{V_p^2} = \left(\frac{4\pi}{3}\right)^2 R_6 R_5 R_4 R_3 R_2 R_1 \tag{27}$$

where

$$R_x = \frac{z+x}{z+1} R_0 \tag{28}$$

These quantities can be compared with values measured with WAXS. One example is the size of a nanocrystal, which can be estimated from the breadth of the first order WAXS diffraction peak using the Scherrer formula (see section 3.3.6). Assuming no additional peak broadening, which may result from instrumental resolution and lattice imperfection due to dislocation, stacking faults, twinning or micro strain, the Scherrer size is the same as the volume-weighted particle size determined by SAXS:[90]

$$D_{\text{Scherrer}} = 2\sqrt{R_8R_7} = 2R_g\sqrt{5/3} \tag{29}$$

So far these quantities are derived for a spherical particle. Quantities for polyhedral particles can also be calculated by applying a proper shape factor.[64]

3.2.2.2. Cautions for Size Distribution Determination. In practice, determining the size distribution function $n(R)$ can be challenging, especially when experimental constraints require dilute particle concentration and/or short exposure time, which may be necessary for in situ experiments or when sample beam damage can occur. This difficulty stems from the weaker intensity in the higher q region (Figure 7), corresponding to scattering intensities of the smaller particles.[47,87,91] Because of the poor data statistics at higher q, the uncertainty in $n(R)$ is greater for smaller size particles. Further, SAXS intensity is proportional to the square of the volume of a particle, or R^6. Consequently, slight variations of $n(R)$ for small R will not have a significant effect on the scattering, meaning that the shape of $n(R)$ at smaller R may be less meaningful than at larger R. Thus, in the literature, instead of $n(R)$, the volume distribution $n(R)$ $V_p(R)$ is more commonly presented. When reporting size, it is useful to plot either R_g or R_0 and σ. Presenting only the number-average radius R_0 may be misleading because R_0 is very sensitive to the quality of data fitting, especially in the high q region. On the other hand, R_g is a z-averaged value determined

DOI: 10.1021/acs.chemrev.5b00690
Chem. Rev. XXXX, XXX, XXX–XXX

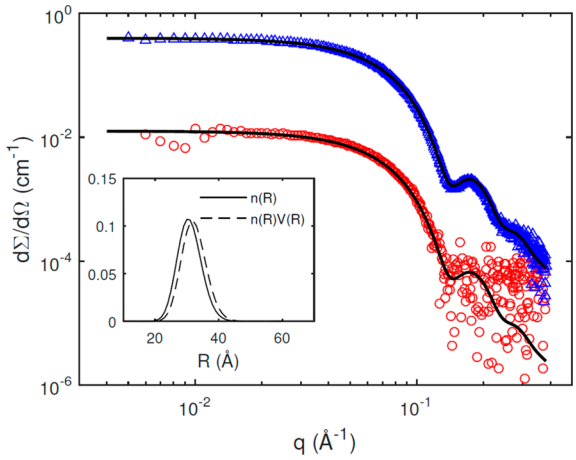

Figure 7. Size distribution function fits (black solid line) for Pt nanoparticles with concentrations of $\phi_p = 5.66 \times 10^{-8}$ (red circles) and 1.79×10^{-6} (blue triangles). Inset is the size distribution function for the fit.

primarily from the small q region, where intensities are stronger and have better statistics.

Often, in this analysis, $F(\boldsymbol{q},R)$ is assumed to be a solid object such as a sphere. However, this may not always be true. One may be able to obtain some information about the particle shape from the asymptotic behavior in the Porod region (see section 3.2.3.2). If the data in the high q region decays as q^{-4} (Figure 4c,d), a solid object model such as a sphere can be used. If the data shows a slope larger than −3, any solid object model may not provide a good fit since this power law can be attributed to a fractal object, which would require a fractal form factor (see section 4.3.2 and reference therein).

Since the form factor oscillation is highly sensitive to polydispersity, it is necessary to fit the oscillation to obtain a more accurate size distribution function. However, as we have shown above (see section 3.2.2 and Figure 5), nonspherical shaped particles such as polyhedra will also smear the form factor minima. While the polydispersity will lead to greater damping at higher q, the shape effect is dominant at lower q (Figure 5 vs Figure 6). In some cases, the instrumental resolution function is required for SAXS,[30,59,92] although it may be less of an issue with modern synchrotron X-ray sources unless particles are highly monodisperse and large (larger than about 100 nm with less than about 5% polydispersity, as a rule of a thumb).

3.2.3. Guinier, Porod, and Invariant Analysis. The analysis of particle morphology typically begins with a coarse inspection of the asymptotic behavior of each SAXS spectrum. Depending on the level of analytical complexity to which one would like to commit, as well as the information one hopes to obtain, there are several paths forward, including empirical modeling and integrating intensities. These simplified methods are discussed in the following sections. After obtaining some knowledge of the sample, one may build a complex model with which to fit the data.

3.2.3.1. Guinier Approximation. The Guinier approximation describes asymptotic behavior in the small q region, and states that any form factor function can be approximated to a Gaussian function in the small angle limit. This provides the most important simple but accurate method to determine the size of a particle using SAXS. It requires scattering data that contains no structure factor, a condition that can typically be met for dilute solutions. In addition, the data must be measured to sufficiently small angles, $q < 1/R_g$. The radius of gyration R_g is the root-mean-square (RMS) of the scattering length density weighted distances from the center of mass to each atom of the particle. For X-ray analysis, R_g can be thought of as the mass-weighted RMS radius. According to Guinier, SAXS intensity in the small angle limit is

$$\frac{d\Sigma}{d\Omega}(q) = \frac{d\Sigma}{d\Omega}(0)e^{-R_g^2 q^2/3} \tag{30}$$

Equation 30 suggests that, regardless of particle shape, it is possible to determine the mean particle size from the very small angle region data. For a system of monodisperse spheres, $d\Sigma/d\Omega(0) = (\Delta\rho)^2 N_p V_{sp}^2/V$ and $R_g = R\sqrt{3/5}$.

3.2.3.2. Porod Approximation. The Porod approximation describes asymptotic behavior at high q. When particles are randomly oriented 3D solid objects with sharp interfaces, the intensity in the high q region, $q \gg \pi/R_g$, follows a power law decay of q^{-4}.

$$\lim_{q\to\infty} q^4 \frac{d\Sigma}{d\Omega}(q) = P \tag{31}$$

where P is the Porod constant. Porod showed that $P = 2\pi(\Delta\rho)^2 S/V$, where S is the total surface area in the sampling volume V.[25,93] Considering $S = N_p\overline{S_p}$, one obtains

$$\frac{P}{\frac{d\Sigma}{d\Omega}(0)} = \frac{2\pi\overline{S_p}}{\overline{V_p^2}} \tag{32}$$

where N_p is the number of particles; $\overline{S_p}$ and $\overline{V_p^2}$ are the mean surface area and mean square volume of the particles, respectively. This concept is important for calculating the surface area of particle systems or porous materials.

3.2.3.3. Dimensionality. It is well-known that the Porod exponents, or the power law exponents, of a one-, two-, or three-dimensional object, such as an infinitely thin rod, an infinitely thin disk, or a sphere, are −1, −2, or −4, respectively.[25] It is also well-known that the Fourier transform of a delta function (which describes a zero-dimensional (0D) object) is a constant, and thus its Porod exponent is 0. It should be noted that this analysis is only applicable to systems with sharp interfaces; otherwise please see the discussion regarding fractals, section 4.3.2. This concept can be illustrated with a simple object: consider a rod, for example. When viewed from a short distance (in real space) or in the high q region (in reciprocal space), the rod appears to be a 3D object (Figure 8, region III). However, from a distance larger than its diameter D but less than its length L, or intermediate q range, it would look like a 1D object (Figure 8, region II). When it is viewed at an even farther distance larger than L, it will appear to be a 0D object, resulting in a flat intensity region at low q (Figure 8, region I). Consequently, the shape of the scattering curve for a rod,[94] and thus the Porod exponent, will vary depending on the observed q range; $I(q) \propto q^{-4}$ when $q > 2\pi/D$, $I(q) \propto q^{-1}$ when $2\pi/L < q < 2\pi/D$, and $I(q) \propto q^0$ when $q < 2\pi/L$ (Figure 8).

The scattering of the rod may be compared to a disk with thickness T and diameter D. Its form factor, shown in Figure 8, displays an $I(q) \propto q^{-2}$ power law decay when $2\pi/D < q < 2\pi/T$ (Figure 8, region II) and $I(q) \propto q^{-4}$ when $q > 2\pi/T$ (Figure 8, region III). A sphere has only one Porod region, $q > 2\pi/D$ with an exponent −4.

DOI: 10.1021/acs.chemrev.5b00690
Chem. Rev. XXXX, XXX, XXX−XXX

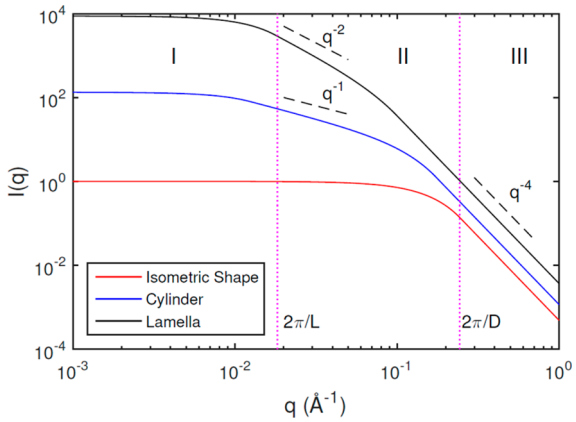

Figure 8. Calculated form factor scatterings of objects with various dimensions and sharp interfaces. The R_g of the isometric particle is 1 nm. The cylinder has a diameter of 2.8 nm (R_g of 1 nm) and length 34.5 nm (overall R_g of 10 nm). The thickness and width of the lamella are 3.4 nm (R_g of 1 nm) and 34.5 nm, respectively (overall R_g of 10 nm). These data were calculated from the Guinier−Porod model.[95]

Oriented systems may show different behavior. When a rod and disk are oriented so that their cylinder axis is parallel to the q_z-direction, the power law along $q_{\|}$ is −3 at $q_z = 0$, as expected from the cylinder form factor equation (see section 3.2.1).

3.2.3.4. Empirical Models. There are several empirical models that do not require analytical derivation using eq 10. Instead, only the asymptotic behavior of the SAXS data is analyzed; in this case, the data may be represented with Porod type power law scattering at high q and Guinier scattering at low q.[95] These empirical models are useful for samples that have significant size and/or shape polydispersity, or objects that have mass/surface fractal nature. Their form factor scattering will likely not display any oscillating intensity or q^{-4} decay. Beaucage et al. employed the unified scattering theory, which employs multiple sets of Guinier and Porod equations,[96] to show how the polydispersity index can be obtained from the model without computing the size distribution. This makes the analysis easier and yields faster computations.[97] Further examples of this model are found in sections 3.4 and 4.3.

3.2.3.5. Invariant. The invariant is the volume integration of the entire reciprocal space scattering, which can be written for an isotropic scattering pattern as

$$Q = \int_V \frac{d\Sigma}{d\Omega}(\boldsymbol{s})\, d\boldsymbol{s} = \frac{1}{2\pi^2}\int_0^\infty q^2 \frac{d\Sigma}{d\Omega}(q)\, dq \tag{33}$$

where $\boldsymbol{s} = \boldsymbol{q}/2\pi$ is the scattering vector used in crystallography. As its name implies, the invariant is proportional to the total excess scattering length density (or electrons for X-rays). Therefore, regardless of the size, shape, number of particles, or their relative positioning, if the total number of excess electrons in the sampling volume remains constant, Q will remain constant.

For a solid object in solution

$$\frac{1}{2\pi^2}\int_0^\infty q^2 P(q)\, dq = (\Delta\rho)^2 \overline{V}_p \tag{34}$$

Therefore, for a dilute particle solution

$$Q = (\Delta\rho)^2 \phi_p \tag{35}$$

For a nondilute particle solution

$$Q = (\Delta\rho)^2 \phi_p (1 - \phi_p) \tag{36}$$

With these equations, one can obtain particle volume concentrations without model fitting. This type of analysis is important when the concentration of particles is of interest, for example in determining extinction coefficients or porosity, or for in situ nanoparticle synthesis studies. For crystalline nanoparticles, the molar concentration of atoms comprising the particles is $N_A \phi_p N_u / V_u$, where N_A, N_u, and V_u are Advogadro's number, the number of atoms in a unit cell, and the unit cell volume for the particle, respectively.

If one employs model fitting using eq 8, it is possible to determine the particle number concentration f_p. These two values f_p and Q are useful, for example, to study nucleation and growth of metal nanoparticles synthesized by reduction of metal precursors. When particles nucleate, both f_p and Q will increase. During the growth phase, f_p will remain constant while Q will continue to increase. When the particles coarsen, f_p will decrease while Q remains constant. Further examples are found in section 7.1.3.

3.2.4. Model Analysis: Morphology. When a particle is composed of a random mixture of two components, or it is alloyed, its scattering length density is the mean of each component scaled by its volume fraction. When the components are segregated into different domains, a shape function for each domain can be developed based on eq 12. The form factor amplitude for the entire particle (which includes both components) is a sum of the shape functions scaled by their respective excess scattering length densities. For example, when there are two domains 1 and 2 of a single particle, with excess scattering length densities and size parameters, $\Delta\rho$ and R, respectively, the form factor amplitude of the overall particle that includes both domains is

$$\begin{aligned} F(\boldsymbol{q}, \Delta\rho_1, \Delta\rho_2, R_1, R_2) \\ = \Delta\rho_1 \Sigma(\boldsymbol{q}, R_1) e^{-i\boldsymbol{q}\cdot\boldsymbol{X}_1} + \Delta\rho_2 \Sigma(\boldsymbol{q}, R_2) e^{-i\boldsymbol{q}\cdot\boldsymbol{X}_2} \end{aligned} \tag{37}$$

where $\boldsymbol{X}_1$ and $\boldsymbol{X}_2$ are the center-of-mass positions of domain 1 and 2, respectively. Then

$$\begin{aligned} P(q, \Delta\rho_1, \Delta\rho_2, R_1, R_2) = (\Delta\rho_1)^2 \langle |\Sigma(\boldsymbol{q}, R_1)|^2 \rangle \\ + (\Delta\rho_2)^2 \langle |\Sigma(\boldsymbol{q}, R_2)|^2 \rangle + 2\Delta\rho_1 \Delta\rho_2 \langle |\Sigma(\boldsymbol{q}, R_1)\Sigma(\boldsymbol{q}, R_2) \\ e^{-i\boldsymbol{q}\cdot(\boldsymbol{X}_1+\boldsymbol{X}_2)}| \rangle \end{aligned} \tag{38}$$

When the sizes of components 1 and 2 are polydisperse and their positions are irregular, the cross term may be smeared out by averaging $P(q)$ for many particles.

For systems where the shape of each component can be easily described mathematically, it may be possible to derive a form factor formula for the model. The following sections make use of analytical models to analyze form factor scattering of multicomponent structures. Numerous models have been developed for various materials, such as inorganic nanoparticles[63,64] as well as particles that self-assemble from small molecules, including micelles[98] and phospholipid nanodisks.[99] While these types of organic multicomponent particles are outside the scope of this review, the models are available in various software packages.[33−35] We have already discussed the scattering from solid objects, i.e. spherical and polyhedral particles. Thus, in the following sections we limit discussion to models that are of use for multicomponent inorganic

DOI: 10.1021/acs.chemrev.5b00690
Chem. Rev. XXXX, XXX, XXX−XXX

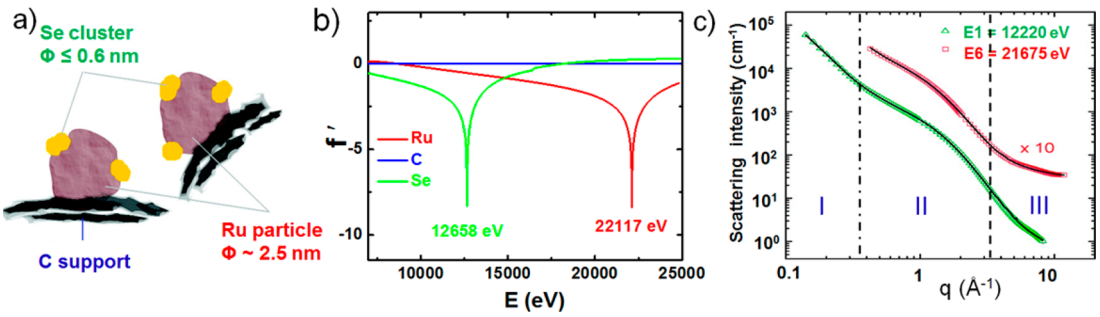

Figure 9. ASAXS studies of carbon supported Ru−Se based catalysts. (a) Schematic drawing of the sample. (b) f' values for three elements, Ru, C, and Se, at $q = 0$. (c) ASAXS data (symbols) and corresponding fits (solid lines) measured at two different X-ray energies. (a, c) Reproduced from ref 113. Copyright 2010 American Chemical Society.

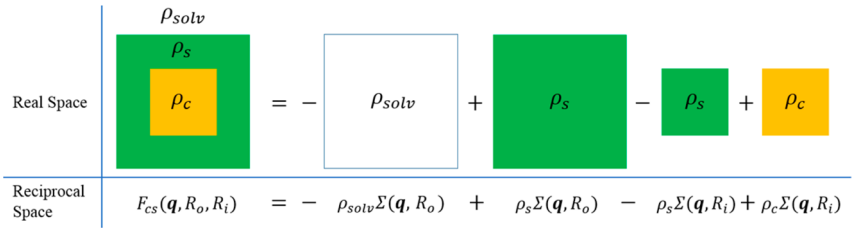

Figure 10. Derivation of the form factor amplitude of a core−shell particle using the linearity property of Fourier transform. See text and eq 39 for definitions of parameters.

nanoparticle research, paying special attention to structures of binary composition.

3.2.4.1. Contrast Variation Methods. When the scatterings from two components are mixed, it may not be easy to distinguish their respective contributions. This problem has been addressed by the small angle scattering (SAS) community (including both X-rays and neutrons) by developing contrast variation methods to vary the scattering length density ρ, which is $r_e\rho_e$ for SAXS and $b_A n_A$ for SANS, where b_A and n_A are the scattering length and atomic number density of the atom, respectively.

For example, when $\Delta\rho_1$ is kept constant and $\Delta\rho_2$ is reduced, the contribution from the second component will decrease (eq 37). Experimentally, this can be achieved in several ways. Anomalous SAXS (ASAXS) can be used to affect this contrast variation by scanning the X-ray energy around the X-ray absorption edge of an element of one or both components. The electron density of an atom is $\rho_e = n_A f_A$, where n_A and f_A are the number density and atomic scattering factor of the atom, respectively. The quantity f_A varies with X-ray energy E such that $f_A(q,E) = f_o(q) + f'(q,E) + if''(q,E)$, where f_o is the kinematic scattering factor that is proportional to the number of electrons in the atom. The resonance terms f' and f'' are the real and imaginary corrections for dispersion, respectively.[100] This means that both amplitude and phase of ρ vary as a function of X-ray energy. We refer interested readers to recent review articles.[100,101] An example will be shown in section 3.2.4.2.

Second, the protein crystallography community has employed a heavy ion replacement method,[102] which may be borrowed by SAS. Third, SANS and SAXS may be performed on the same sample. The scattering length density of an element in SANS is very different from that in SAXS. An element with higher atomic number has stronger X-ray scattering; however, this is not the case for neutron scattering. For example, the b_A of silicon is smaller than that of deuterium. In SANS, the solvent is often replaced with a deuterated or mixed component solvent to vary the contrast. Examples of these second and third methods will be shown in section 3.2.4.3.1.

3.2.4.2. Form Factor of Multicomponent Particles. Two components that phase separate within a single particle can be distributed into various morphologies.[103,104] For example, the growth of spherical Au nanoparticles on the tips of semiconductor nanorods was studied by in situ SAXS. The Au atoms reduced by UV irradiation were found to heterogeneously nucleate and grow on the nanorods.[105] Kwon et al. reported mechanistic studies regarding the growth of Au nanoparticles that heterogeneously nucleated on CoPt nanocrystal seeds. They observed two morphologies, initially a core−shell structure, which transitioned into a dumbbell shape due to lattice mismatch.[106] This transition is similar to classical Stranski−Krastanov growth found in epitaxially grown films.[107] In their work, the morphological transitions were observed by SAXS and lattice constant variations were monitored by WAXS.

Recently, several groups studied nanodroplets that had a Russian doll morphology, which was phase separated from a mixture of water and nonane.[108] Obeidat et al. developed an analytical form factor of a Russian doll particle.[109] This allowed them to calculate the contact angle between the two liquids under various conditions.[110] Similarly, the form factors of Janus particles with spherical and cylindrical shapes were developed.[111] Later, Fütterer et al. developed the form factor of a Janus particle with a core−shell morphology, where the shell had two distinct parts.[112] Their work suggested that contrast variation methods may be needed for these types of morphologies.

Haas et al. analyzed the structure of carbon supported Ru−Se based catalysts using ASAXS.[113,114] The sample has three scattering components—porous carbon supports, Ru particles, and Se particles—as shown in Figure 9a. The system was described using three terms in eq 38, one for each component,

DOI: 10.1021/acs.chemrev.5b00690
Chem. Rev. XXXX, XXX, XXX−XXX

without the cross terms. To distinguish between each component, the authors performed ASAXS at both Ru and Se absorption edges (Figure 9b). Figure 9c presents two representative scattering curves measured slightly below each edge. When SAXS is measured at high energy (21 675 eV) close to the Ru edge, $\Delta\rho_{Ru} = \rho_{Ru} - \rho_{air}$ will decrease. Thus, there is a relative increase in the scattering from the Se particles and porous carbon. At the other edge, $\Delta\rho_{Se} = \rho_{Se} - \rho_{air}$ will decrease and thus the relative contributions from Ru and carbon will increase. The intensity in region III of Figure 9c increased only for the measurement performed at the Ru edge. This result indicated that the contribution from the Se particle dominates at high q, and thus the Se particles are small in diameter. Similarly, the scattering contributions in regions I and II may be attributed to the porous carbon support and Ru particles, respectively.

3.2.4.3. Core–Shell Particles. The most representative phase segregated morphology is a core–shell structure (Figure 10). The form factor of a core–shell particle, whose center of mass is at the origin of a real space coordinate system, is

$$F_{cs}(\boldsymbol{q}, \rho_c, \rho_s, \rho_{solv}, R_c, R_i) = (\rho_s - \rho_{solv})\Sigma(\boldsymbol{q}, R_c) + (\rho_c - \rho_s)\Sigma(\boldsymbol{q}, R_s) \quad (39)$$

where ρ_s, ρ_{solv}, and ρ_c are the scattering length densities of the shell, solvent, and core, respectively. The sizes of the inner (core) and outer (shell) sections of the particle are R_s and R_c, respectively. This formula can be used for any shaped particle.[63] In sections 3.2.4.3.1 and 3.2.4.3.2, we discuss several examples.

3.2.4.3.1. Inorganic Core, Organic Shell. The strong scattering of an inorganic core can be problematic when trying to examine core–shell particles composed of inorganic cores and organic ligand shells. For example, the second contrast variation method mentioned in section 3.2.4.1, heavy ion replacement, was necessary to examine DNA-conjugated nanoparticles (Figure 11a,b).[115] The distribution of cations in the DNA ligand shell has been believed to affect the DNA conformation and cooperative dissociation transition, but direct verification of the cation concentration has been challenging. Kewalramani et al. varied the type of monovalent cation in the DNA ligand shell, and thus the electron density, and measured the corresponding variations in the scattering curves. This methodology of course assumes that replacing light ions with heavier ones will not change the structure. They determined that there is a 10–15 times increase in monovalent cation concentration in the DNA ligand shell compared to the surrounding buffer, validating existing theories. Further, there is a radial distribution, with a higher cation concentration close to the nanoparticle shell that decreases with increasing distances. They were further able to conclude that the conformation of the double stranded DNA section is identical to that of B-form DNA with 0.34 nm rise per base, while that of the single stranded section has a 0.18 nm rise per base.

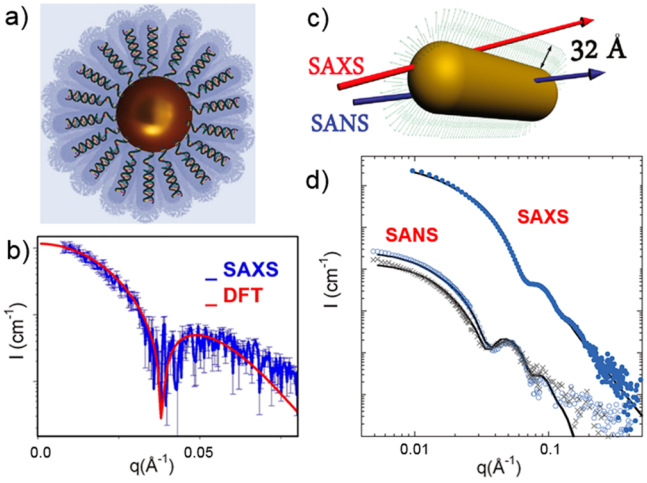

Figure 11. (a) Schematic illustration of a spherical nucleic acid Au nanoparticle conjugate (SNA–AuNPs) and associated counterion cloud. (b) The radial distribution of monovalent cations surrounding SNA–AuNPs is determined by SAXS and classical density functional theory (DFT) calculations. (a, b) Reprinted from ref 115. Copyright 2013 American Chemical Society. (c) Schematic representation of Au nanorods (GNRs) coated with CTAB bilayer. (d) One-dimensional SAXS and SANS patterns of GNRs stabilized by CTAB. (c, d) Modified from ref 116. Copyright 2012 American Chemical Society.

Alternatively, the particles can be measured using both X-ray and neutron sources. Gómez-Graña et al. examined bilayers of CTAB and a gemini surfactant on gold nanorods using SAXS (to determine the nanoparticle size) and SANS (to determine the nanoparticle + ligand size) (Figure 11c,d).[116] They found the bilayer to be 32 ± 2 Å thick, with slight interdigitation of the hydrophobic tails. The molecular packing was approximately 80–100% of the corresponding CTAB or gemini surfactant crystal. Determining the thickness of the surfactant with SANS is not an easy task because of the existence of excess surfactant that forms free micelles, which generates a strong background.[117] Any reduction in the concentration of the free micelle may cause loss of the particle-bound molecules that are in dynamic equilibrium with nonbound surfactant.[118] Donnio and Murray et al. also performed SAXS and SANS measurements on a series of dendritic ligand-coated AuNPs in solution and in dried assemblies.[119] They found that higher generations of the dendritic ligands are less compressible than lower generations or linear analogues, which is known as the dendritic effect. As result, assemblies of particles with higher generation dendritic ligands possess larger unit cell volume due to steric effects.

3.2.4.3.2. Inorganic Core, Inorganic Shell. Podsiadlo et al. studied hollow iron oxide nanoparticles synthesized using the Kirkendall effect.[120] While the core–shell structure was obvious in TEM images (Figure 12a), it was not possible to determine the core density, which may be important to understanding the response of the material under high pressure. A core–shell model fit the SAXS data well (Figure 12b). From the fitting, the density of the core was at least double that of the solvent. When the density difference between core and shell is not significant, such as an Fe_3O_4 core with a Mn_2O_3 shell, ASAXS can be useful.[121,122] From the ASAXS, the contributions of the Fe_3O_4 and Mn_2O_3 were determined separately, as shown in Figure 12c. This allowed the authors to ascertain the compositions of the core and shell, where the pure Fe_3O_4 core was surrounded by a $(Mn_xFe_{1-x})_3O_4$ shell with a graded composition (Figure 12d).

Small angle scattering can also be used to study the interface between the core and shell. For example, Kluthe et al. examined the segregation of hydrogen to the interface of a Ag core and MgO shell nanoparticle. Gas segregation at an interface may influence the chemical structure and therefore material properties. For this type of problem where light elements are of interest, SAXS does not provide enough contrast to

DOI: 10.1021/acs.chemrev.5b00690
Chem. Rev. XXXX, XXX, XXX–XXX

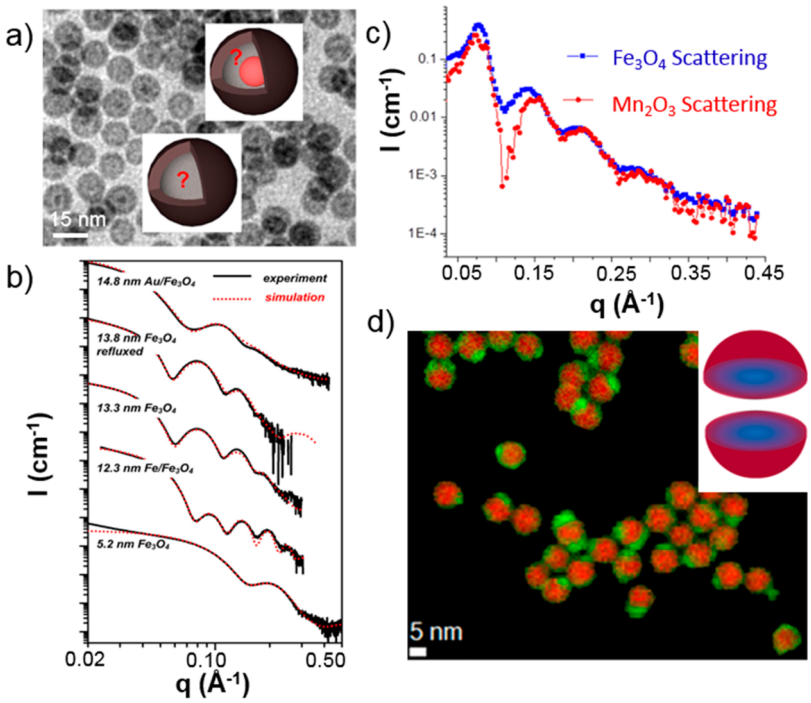

Figure 12. (a) TEM image of as-synthesized Fe_2O_3 nanoparticles. (b) Experimental and simulated SAXS spectra of Fe_2O_3 nanoparticles dispersed in toluene. (a, b) Reprinted from ref 120. Copyright 2013 American Chemical Society. (c) ASAXS of Fe_3O_4 (core)−γ-Mn_2O_3 (shell) nanoparticles measured at both Fe and Mn K-edges. (d) STEM with EELS Fe (red) and Mn (green) elemental mapping for Fe_3O_4 (core)−γ-Mn_2O_3 (shell) nanoparticles. (c, d) Reprinted from ref 121. Copyright 2013 American Chemical Society.

determine the hydrogen distribution, and thus complementary SANS techniques were employed.[123]

Strasser's group monitored the dealloying of alloyed nanoparticles. For example, the electrochemical transformation of alloyed $Pt_{25}Cu_{75}$ into core−shell structures was examined with ASAXS.[124] They further determined the lattice parameter of the shell using anomalous diffraction (AXRD)[125] and concluded that the compressed lattice parameter of Pt due to the PtCu core is caused by the lattice mismatch between core and shell. This result was able to explain the significant improvement in the electrocatalytic activity of the Pt.

3.3. Structure Factor Analysis

While SAXS form factor analysis provides a wealth of information at the single particle level, the structure factor allows one to determine the organization of particle systems. This can range from disordered networks that are primarily characterized by an average distance between particles to crystalline systems with structure factors that are equivalent to those in atomic diffraction.

It is important to understand the differences between various methods used to calculate the structure factor. For example, Figure 13 compares the structure factor of a model system calculated using two methods. $S(q)$ may be directly calculated using eq 15 (black broken line). Alternatively, one may use a procedure more akin to experimental methods, by first calculating $I(q)$ and $P(q)$, and then determining $S(q)$ (recall $S(q) = I(q)/P(q)$, red solid line). The difference between the two curves arises from the difficulty in decoupling $P(q)$ and $S(q)$ when particles are not monodisperse spheres (see section 3.1). The discussion in sections 3.3.1 and 3.3.2 makes the assumption that there is no difficulty in decoupling form and structure factors, even though particles may not necessarily be monodisperse spheres. In sections 3.3.4−3.3.6, the structure factor will be redefined to account for this additional complexity.

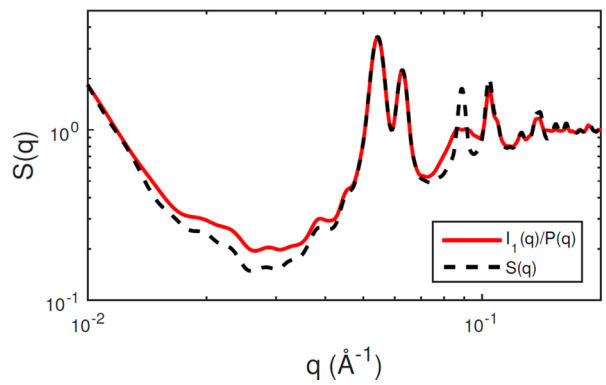

Figure 13. Structure factors may be calculated using two methods, using eq 15 (broken black line) or using an "experimental" method; see text. The model system consists of 1000 spherical particles with mean radius of 5 nm and 10% polydispersity packed into a face-centered-cubic (fcc) lattice with a lattice constant of 20 nm.

3.3.1. Pair Distribution Function. When a set of particles generate isotropic scattering, regardless if they are distributed homogeneously in solution or assembled into a nanoparticle superlattice, one may assume that the system is randomly oriented in all three dimensions. This situation is equivalent to powder diffraction. The isotropic structure factor $S(q)$ of such a system is related to its radial distribution function or pair distribution function $g(r)$ as

$$S(q) = 1 + n_p \int (g(r) - 1)(4\pi r^2)\frac{\sin(qr)}{qr}\,\mathrm{d}r \tag{40}$$

DOI: 10.1021/acs.chemrev.5b00690
Chem. Rev. XXXX, XXX, XXX−XXX

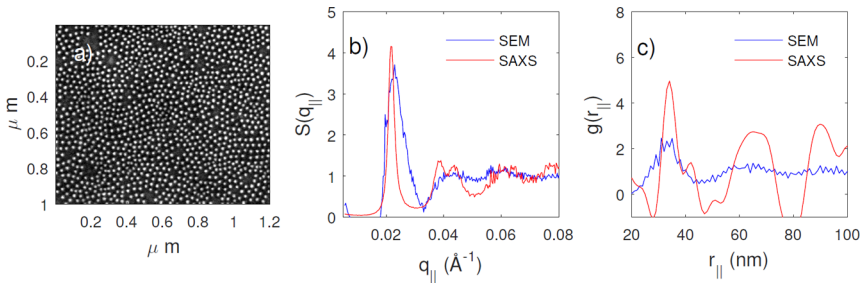

Figure 14. (a) SEM image of 15 nm DNA-conjugated gold nanoparticles (DNA–AuNPs) hybridized to DNA modified substrates. (b) Structure factors calculated from SEM and experimental SAXS data. (c) The pair distribution function calculated from the structure factor in (b) shows sharper peaks and clearer hexagonal symmetry than the pair distribution function calculated from the SEM in (a), likely because of better statistics. Reproduced from ref 129. Copyright 2014 American Chemical Society.

where n_p is the particle number density. It is worth noting that, in section 3.1 and eq 8, we use f_p for the particle number density. When a solution is homogeneously filled with particles, these two should be the same. Otherwise, for example, when particles form assemblies, n_p is the particle number density in an assembly and f_p is that of the entire solution.

Equation 40 suggests that the Fourier transform of $g(r) - 1$ is $S(q) - 1$, allowing one to convert between real and reciprocal space. By making this conversion, even without assuming a symmetry for the particles' arrangement for a given sample, one is able to determine the nearest neighbor distance using SAXS. When the particles are on a 2D plane, for example on the *xy*-plane, the structure factor is

$$S(q_{\parallel}) = 1 + n_p \int (g(r_{\parallel}) - 1)(2\pi r_{\parallel}) \frac{\sin(q_{\parallel} r_{\parallel})}{q_{\parallel} r_{\parallel}} \, \mathrm{d}r_{\parallel} \tag{41}$$

where $r_{\parallel}$ is a distance in the plane.

The inverse Fourier transform of the structure factor will result in the pair distribution function, which is very well established in the atomic pair distribution function (PDF) technique:[126,127]

$$g(r) = 1 + \frac{1}{2\pi^2 n_p} \int (S(q) - 1) q^2 \frac{\sin(qr)}{qr} \, \mathrm{d}q \tag{42}$$

In the atomic PDF literature,[127,128] the reduced pair distribution function $G(r) = 4\pi n_p r(g(r) - 1)$ is typically computed since it does not require prior knowledge of n_p. Thus, when examining superlattice assemblies, SAXS should be able to make use of the same techniques and assumptions.

When the positions of the particles are known, one can calculate the structure factor using these equations. For example, the structure factor shown in Figure 14 is calculated using eq 41, from a pair distribution function obtained from a scanning electron microscopy (SEM) image of 15 nm gold nanoparticles deposited on a substrate.[129] The same sample was examined by X-ray scattering, and the experimental structure factor was extracted from the data. Figure 14, parts b and c, compare structure factors and pair distribution functions from the experimental X-ray data and SEM imaging, respectively. In general, they match well, though the X-ray scattering structure factor shows sharper peaks and more clearly displays the 2D hexagonal symmetry. This is likely because of the relatively small region of interest that one obtains from electron microscopy compared to X-ray scattering.

3.3.2. Isotropic Homogenous Liquid-Like Structures. In the dilute limit, such as in the case of a gas or dilute particle solution, the probability of the relative distance between two particles can be given by the Boltzmann distribution and thus

$$g(r) = \exp\left(-\frac{u(r)}{k_B T}\right) \approx 1 - u(r)/(k_B T) \tag{43}$$

In this case, it is straightforward to compute $g(r)$ for a given $u(r)$, and then $S(q)$ from the $g(r)$ using eq 40.

As the density of the system increases, the position of a particle cannot be determined from a single nearest neighbor interaction. Instead, one must take a many-body system approach, in which a particle interacts with all neighboring particles, which may rebound affecting the original particle, thus requiring examination of next-nearest-neighbor interactions. In 1914, Ornstein and Zernike proposed an integral equation, called the OZ equation, to calculate the pair distribution, or the pair correlation, by splitting the direct correlation and indirect correlation.[130] The OZ equation relates the total correlation function, $h(r) = g(r) - 1$, to a direct two particle correlation function $c(r)$. To solve the OZ equation for a given pair potential function, a closure relation is required. In the nanoparticle literature, several closure relations are found, the simplest of which is the mean spherical approximation (MSA),[131] where $c(r) = -u(r)/(k_B T)$. The OZ equation was also solved with the Yukawa potential under the MSA.[132] Liu et al. studied clustering of proteins using two Yukawa potentials for short-range attraction and long-range Coulombic repulsion.[133] They found that there is an even longer range attraction than the charge repulsion.[134]

When $u(r)$ and a closure relation are chosen, the structure factor can be derived using the following relations.

The Fourier transform of an isotropic system is

$$C(q) = \int c(r)(4\pi r^2) \frac{\sin(qr)}{qr} \, \mathrm{d}r \tag{44}$$

By employing the OZ equation

$$S(q) = \frac{1}{1 - n_p C(q)} \tag{45}$$

The most commonly used closure relation is the Percus–Yevick (PY) approximation, where

$$c(r) = g(r)\left(\exp\left(\frac{u(r)}{k_B T}\right) - 1\right)$$

It has been employed for the hard sphere[20,135,136] and sticky interaction potentials.[13,137−139] A certain pair potential may work better with a particular closure relation than others.[140]

DOI: 10.1021/acs.chemrev.5b00690
Chem. Rev. XXXX, XXX, XXX−XXX

The interested reader is referred to several recent articles for a further discussion of closure relations and the solutions of various pair potentials.[21,141]

Using the relationships above, one may calculate the pair potential, $u(r)$, from the experimental structure factor, $S(q)$. This is possible because one can obtain $C(q)$ from eq 45 and $c(r)$ from the Fourier transform of eq 44. In addition, $g(r)$ can be obtained from eq 42. The microscopy community has used the Boltzmann approximation to calculate the pair potential from the pair distribution obtained from optical images.[142] Korgel et al. later calculated $u(r)$ for silver nanoparticles stabilized with alkanethiols from SAXS data by employing the hypernetted-chain (HNC) closure relation, where $\frac{u(r)}{k_B T} = g(r) - 1 - c(r) - \ln(g(r))$.[143] They examined the face-centered-cubic (fcc) to body-centered-cubic (bcc) transition as a function of the particle size, and used the experimentally obtained pair potentials to calculate the free energy difference.

3.3.3. Isothermal Compressibility. In the low q limit, the structure factor approaches a thermodynamic quantity called the isothermal compressibility, which is a measure of the relative volume change as a response to pressure.

$$S(0) = n_p k_B T \chi_T \tag{46}$$

When the scattering intensity of water is measured in the very small angle region, its intensity at zero angle is $I(0) = r_e^2 \rho_{e,w}^2 S(0)$, where $r_e^2 \rho_{e,w}^2$ is the square of the scattering length density of water and $\rho_{e,w}$ is the electron density of water. This $I(0)$ value is known, which enables water to be used as an absolute intensity reference. To measure the isothermal compressibility of colloidal nanoparticles, it is necessary to measure the solution at very small angles so that any tail of the correlation peak does not affect its measurement, for instance using USAXS.

Recently, Baeza et al.[144] examined silica and polymer nanocomposites using SAXS, where silica particles form hierarchical aggregates (see section 3.4.3). The aggregates consist of clusters composed of a collection of silica particles. As a part of the analysis, they performed Monte Carlo simulations to understand the effect of polydispersity on the $S(q\to 0)$ of the particles. It is worth noting that, for a polydisperse system, the $S(q\to 0)$ value determined from the simulation or measured data is, strictly speaking, not an isothermal compressibility. This is because the experimental $S(q)$ is calculated as $I_1(q)/P(q)$, which still contains the particle size information because of limitations using the decoupling approximation (sections 3.1 and 3.3). Therefore, the obtained $S(q\to 0)$ values from the simulation were compared with the isothermal compressibility of the PY structure factor by adding a factor α:

$$S_{PY}(q \to 0) = \frac{(1 - \alpha\phi_p)^4}{(1 + 2\alpha\phi_p)^2} \tag{47}$$

where $\alpha = 1$ for monodisperse particles. Figure 15 shows measured data and their fits with eq 47, showing higher $S(q\to 0)$ for larger polydispersity. This relation was used to determine the volume fraction of the silica particles in the cluster.

3.3.4. Crystalline Assemblies. Small angle diffraction data of particle assemblies have been obtained and analyzed in many ways.[143,145−150] A 1D scattering profile azimuthally averaged from a 3D randomly oriented sample is equivalent to powder diffraction. Thus, small angle diffraction from assemblies can be indexed as is routinely performed for atomic powder diffraction. Once the peaks are indexed, several types of analyses can be performed, each with varying degrees of complexity and time requirements. The simplest type of analysis relies on line profile decomposition, or the fitting single or multiple diffraction peaks. Peak broadening analysis may include calculations of simple domain size using the Scherrer formula, or both domain size and lattice strain using Williamson−Hall analysis (see section 3.3.6).[61] While simple, this type of analysis requires general assumptions about material imperfections, and may be somewhat less realistic.

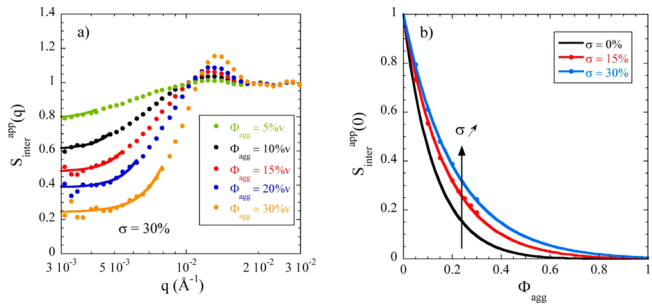

Figure 15. MC simulations of polydisperse systems. Hard sphere repulsive potential is used for the interparticle interaction. (a) Average structure factors of particles with mean radius 20 nm and 30% polydispersity for various volume fractions of particles. The fit in (a) is a polynomial fit to extract $S(0)$. (b) Evolution of $S(0)$ vs the aggregate volume fraction for various particle polydispersities. Adapted from ref 144. Copyright 2013 American Chemical Society.

Fourier synthesis or direct modeling may be performed by analyzing the integrated intensities of multiple peaks. While more realistic, these techniques can also be time consuming. The intensity of each peak is calculated after developing a model of the symmetry and microstructure specific to the material under investigation. Fourier synthesis requires one to make an educated guess as to the phases of individual diffraction peaks, which can be possible in SAS because nanostructures can be highly symmetric.[148,151−155] Direct modeling consists of constructing a unit cell model, calculating the intensities of reflections and comparing these with measured integrated intensities.[150,156] In addition, there are methods utilizing the correlation function that corresponds to the Patterson function in X-ray diffraction. In SAXS, it has been typically used for more or less 1D structures such as lamella stacking.[157] The correlation function is discussed further in section 4.

The degree of ordering for particle superlattices is often inferior to their atomic counterparts. Superlattices often contain a variety of imperfections that originate from the inherent differences between particles and atoms, which may include size polydispersity and orientational disorder of particles within the lattice. Positional fluctuations and lattice distortion (or defects of the first kind and second kind, respectively) exist for both nanoparticle superlattices and atomic crystals, but are often worse for particle systems. These defects weaken and broaden reflections, resulting in peak overlap that can cause significant uncertainty when determining the integrated peak intensity. Thus, for particle assemblies, a full profile analysis that takes into account all peaks as well as form factor and potentially diffuse scattering is more attractive than only analyzing a collection of decomposed peaks because it provides higher

DOI: 10.1021/acs.chemrev.5b00690
Chem. Rev. XXXX, XXX, XXX−XXX

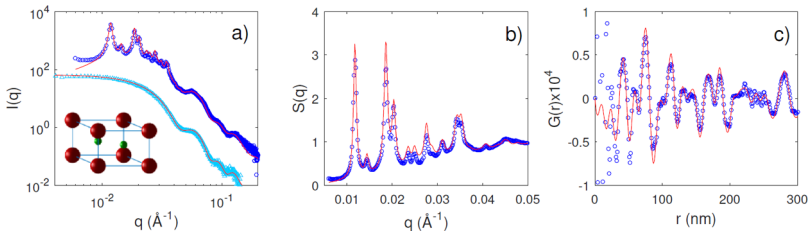

Figure 16. (a) The SAXS profile of a DNA–AuNP superlattice with AlB_2 arrangement (see inset) is shown in blue circular symbols, and the form factor scattering measured above its melting temperature is in sky blue triangular symbols. The red solid lines are fits. (b) Experimental (symbol) and theoretical (line) $S(q)$ for data in (a). (c) Reduced pair distribution functions calculated from the structure factors in (b). The oscillations at $r < 30$ nm are from Fourier noise. Experimental data in (a) were published in ref 12.

accuracy as well as more information. However, it requires analytical formalism. The full scattering profile calculation has evolved based on Hosemann's paracrystal theory with the decoupling approximation (DA).[46] Matsuoka et al. first calculated full intensity profiles for simple cubic (sc), bcc, and fcc superlattices using DA and the paracrystal approach.[145,146,158] Others also used DA to develop a powder diffraction approach.[49] Most of the works in the literature have only dealt with superlattices composed of a single particle type.[49,145]

Recently, the pseudolattice factor method has been developed for multicomponent superlattices and ones that include polyhedral particles.[159] Since then, it has been applied for crystalline assemblies composed of multiple types of spherical particles[12,160] or polyhedral particles.[70,159,161] Complete formalism was recently published[39,162] with approximations to overcome the limitations associated with the DA reported in the literature.[163,164] The intensity is then

$$I(q) = N_p P(q)(1 + (Z(q) - \beta(q))G(q)) \tag{48}$$

where the diffuse scattering, $\beta(q)$, is $|\langle\overline{F(\boldsymbol{q})}\rangle|^2/P(q)$, which has been approximated as a Gaussian function.[49] The isotropic Debye–Waller factor may be written $G(q) = e^{-\sigma_D^2 q_{hkl}^2 d_p^2}$, where d_p is the nearest neighbor distance. The lattice factor $Z(q)$ is obtained as follows:

$$Z(q) = \sum_{hkl} Z_0(q_{hkl})\Pi(q;\, q_{hkl}, \sigma_w) \tag{49}$$

where $\Pi(q;\, q_{hkl}, \sigma_w)$ is the peak shape function (typically a Lorentzian function with full width at half-maximum (fwhm) σ_w and integrated area 1) for a reflection *hkl*. Here, $Z_0(q_{hkl})$ is the sum of the square of the phase factors of the *hkl* reflection normalized by the number of particles in a unit cell, the solid angle of the reciprocal space at q_{hkl}, and the dimensional measure (i.e., length, area, or volume) of the unit cell. For example, Figure 16 shows an SAXS profile of a binary nanoparticle superlattice that was calculated using eq 48. Further details are found in the literature.[39] The formalism can be further extended to grazing incidence small-angle X-ray scattering (GISAXS).[68,129,149,165−170]

3.3.5. Structure Determination. The basics of structure determination for a superlattice using SAXS is to a large part the same as in atomic or molecular diffraction. Consequently, the following section will primarily serve to review features that are unique to superlattices within the broader context of diffraction. A more thorough discussion of diffraction can be found elsewhere.[171]

The first step in structure determination is to index the diffraction peaks, which will reveal the lattice dimensions and space group. Because peaks from superlattices are typically broader than those of atomic crystals and may overlap, care must be taken when indexing. Further, the intensities of some peaks may not appear if they are located in the minima of a particle's form factor oscillation. Some commonly found structures in nanoparticle assemblies are listed in section 7.2. There are reports of diffraction analysis from single crystal nanoparticle superlattices, which are sometimes called a mesocrystal or supercrystal.[172,173] Superlattice thin films grown on a substrate are often polycrystalline, but display a preferred orientation normal to the substrate. In other words, they are oriented in the *z*-direction, and randomly oriented in the *xy*-plane. This manifests as a scattering pattern that shows a 2D powder texture, or fiber symmetry, in GISAXS. There are numerous software programs for indexing these types of superlattices.[39,40,174,175]

Once the indexing is performed, the next step is to determine how densities (particles) are distributed in the newly determined unit cell. For nanoparticle assemblies, similar to molecular crystal analysis, a set of known particles with some predetermined shape should be appropriately placed into a unit cell with a particular space group determined by indexing. The space group will determine the possible positions that a particle can occupy, or Wyckoff positions. This placement of particles into the unit cell is an iterative process, whereby a computed diffraction profile from a hypothetical unit cell is compared with the measured data until a best fit is made. If possible, electron microscopy is a useful complementary technique for structural verification. When a sample contains multiple different types of monodisperse particles with different sizes, it is helpful to know the relative number ratio of particles in a unit cell, which will limit the Wyckoff positions of the particles. The ratio of the particles can be obtained from a linear combination of each particle's form factor by approximating the high q region of $I(q)$ as $P(q)$. This is possible because in the high q region there is little to no structure factor $S(q)$, and thus the $P(q)$ contribution will be dominant (i.e., $q > 3 \times 10^{-2}$ Å^{-1} in Figure 16a). However, in some cases diffuse scattering, resulting from lattice defects, will smear the fine features at high q, preventing this type of analysis. Consequently, it may be necessary to melt the superlattice into its distinct components to obtain this ratio (see $P(q)$ of the melted crystal, Figure 16a). There may be other methods to determine the particle number ratio such as UV–vis, ICP, or other chemical analysis depending on the chemical composition of each nanoparticle building block.

Once $P(q)$ is either measured or determined, $S(q)$ can be calculated by $I(q)/P(q)$ as shown in Figure 16b. Calculation of a PDF from the $S(q)$ (Figure 16c) may be helpful to determine the nearest interparticle distance using eq 42.

DOI: 10.1021/acs.chemrev.5b00690
Chem. Rev. XXXX, XXX, XXX−XXX

3.3.6. Peak Shape Analysis. Often, simplified analysis based on peak shape decomposition is sufficient to understand general trends. As early as 1918, Scherrer discussed the inversely proportional relationship between crystal size and X-ray peak width.[176] Stokes and Wilson later reported that microstrain is a second source of peak broadening.[177] Microstrain may arise from a variety of defects of the second kind, and can be interpreted as a distribution of interplanar distances as compared to their regular or average spacing. These two concepts can be quantified as

$$\beta_{\text{size}} = \frac{k\lambda}{D\cos\theta} \tag{50}$$

$$\beta_{\text{strain}} = 4e\tan\theta \tag{51}$$

where β is the peak integral breadth, split into contributions arising from size and microstrain. The volume weighted domain size in the direction parallel to the diffraction vector is D, and k is the Scherrer constant, typically close to 1, that can be used to approximate shape. For a sphere, $k = 0.9$. Assuming a Gaussian distribution, the root-mean-square microstrain $\langle\varepsilon_0^2\rangle^{1/2}$ can be determined from e, where e is the maximal "apparent" strain: $\langle\varepsilon_0^2\rangle^{1/2} = 2/\pi^{1/2}e$.

Williamson and Hall proposed a method to deconvolute size and strain broadening by noting that the effects are additive, analyzing peak width as a function of 2θ, or q.[178] Over the angular range of the power diffraction profile, size broadening will be uniform, while strain broadening will be angular, or q, dependent. By combining eqs 50 and 51, they obtained

$$\beta\cos\theta = \frac{k\lambda}{D} + 4e\sin\theta \tag{52}$$

Thus, a plot of $\beta\cos\theta$ vs $2\sin\theta$ should result in a line, where the size and strain may be determined from the intercept and slope, respectively. More advanced peak decomposition methods exist, including the Warren−Averbach method, that utilize Fourier transform techniques to determine size and strain broadening, with various types of both size and strain distributions.[176,179,180]

While simple, peak decomposition analysis is a powerful method to quickly study nanoparticle superlattices using SAXS.[176,180,181] Often, the type of analysis is dependent on the quality of the crystal and the resulting diffraction pattern. The Scherrer formula is commonly used for a quick estimation of crystallite size.[57,58,61,106,182,183] While analysis of only a single peak is needed for rough size estimation, care must be used when interpreting data from samples with poor diffraction quality, as physical parameters may be substantially different from the values obtained. Nonetheless, Scherrer analysis may be useful for internal comparisons and to determine general trends.

Williamson−Hall analysis requires a SAXS diffraction pattern (and therefore superlattice) of sufficient quality with multiple higher order nonoverlapping peaks (Figure 17a). Size and strain broadening were recently examined for several nanoparticle superlattices assembled using DNA linkers.[61,161] From the linear Williamson−Hall plot, it was determined that the microstrain was isotropically distributed, and decreased as the annealing temperature increased[61] and the length of the DNA linkers decreased (Figure 17b).[161] These results indicate that the microstrain in these structures is related to positional error propagation. Further, the crystallite size was found to increase with annealing temperature, which could be fit to a power law.[61] Sulyanova et al. later studied defects in polystyrene photonic colloidal crystals as a means to understand the origins of optical degradation mechanisms.[184] Using Williamson−Hall analysis, they observed a significant increase in lattice distortion and domain disorientation upon annealing above 355 K.

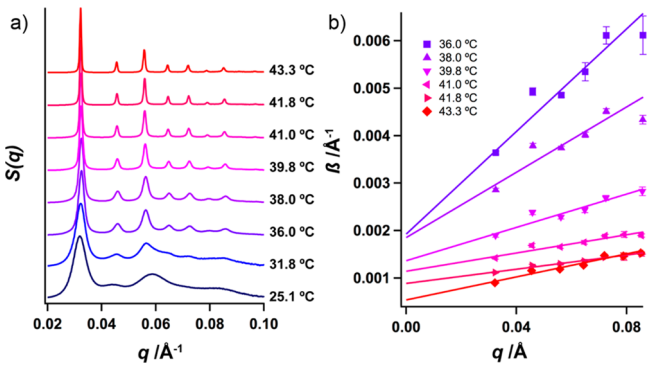

Figure 17. (a) SAXS $S(q)$ for DNA−AuNP superlattices annealed at various temperatures. (b) Williamson−Hall analysis to deconvolute peak broadening arising from grain size (intercept) and microstrain (slope) by plotting β vs peak position (q) for each scattering peak. Adapted with permission from ref 61. Copyright 2014 Wiley-VCH Verlag GmbH & Co. KGaA.

3.4. Limited-Sized Structures

The structures in section 3.3 assumed that the size of the domain is infinite. This may not be true for clusters or aggregates. Even for a colloidal solution, particles with an attractive interaction have been reported to form individual domains.[13] The very small angle scattering from the domains of colloidal nanoparticles is much like a small angle scattering from nanoparticles composed of atoms. Let the mean volume, volume fraction, and mean scattering length density of the domain, or assembly, be $\overline{V}_a$, ϕ_a, and $\overline{\rho}_a$, respectively. The intensity of a finite size superlattice can be approximated by adding the scattering from the external shape of the superlattice to eq 48, yielding[39]

$$\frac{d\Sigma}{d\Omega}(q) \approx \frac{\phi_a(1-\phi_a)(\overline{\rho}_a - \rho_{\text{solv}})^2}{\overline{V}_a}\Sigma_d(q) + \frac{\phi_p(1-\phi_p)}{\overline{V}_p}P(q)\,S_0(q) \tag{53}$$

where $\Sigma_d(q)$ is the shape function of the superlattice. The second term describes the internal structure of the superlattice. When only the tail of the shape function is measured in the experimental q range, the first term on the right side of eq 53 can be represented as the simple Debye−Bueche equation[13] (see section 4.3.1).

In sections 3.4.1−3.4.3, we review the literature of nanoparticle clusters and aggregates. Below, we define both the cluster and aggregate as an assembly of nanoparticles. The cluster is a particle assembly whose size is in the SAXS q range (typically $1 \times 10^{-3} < q < 1$ Å^{-1}). Its internal structure can be described by the structure factors introduced in section 3.3. The aggregate is either a large cluster, whose internal structure is a fractal, or an assembly whose building block is the cluster.

3.4.1. Supraparticles or Particle Clusters. In the literature describing supraparticles or particle clusters, the particles that form a cluster have been called primary particles.[185] Compared to an aggregate, clusters have a more uniform shape, are composed of a smaller number of primary particles, and have a higher packing density with more balanced

DOI: 10.1021/acs.chemrev.5b00690
Chem. Rev. XXXX, XXX, XXX−XXX

interparticle interactions.[186] They may be synthesized using a variety of methods.[185,186] Depending on how the particles attach to each other, their arrangement can be crystalline,[187,188] liquid or plastic crystalline,[189] or amorphous.[190,191]

When primary particles form a cluster, the SAXS form factor of the cluster may be within the observed q range. This scattering would of course be at smaller q than the Guinier knee of the primary particles, $q = \pi/R_{pr}$, where R_{pr} is the radius of the primary particle. It can be seen from eq 7 that, for q close to 0, the intensity becomes

$$I_l(0) = \frac{1}{N_p}\langle|\sum_{l=1}^{N_p} F_l(0)|^2\rangle = N_p P(0) \tag{54}$$

meaning $S(0) = N_p$. In real experiments, the number of particles in a cluster may not be uniform; thus $S(0)$ is statistically

$$S(0) = \frac{\overline{N_p^2}}{\overline{N_p}} \tag{55}$$

Note, this analysis of $I(0)$ is different from the isothermal compressibility described in section 3.3.3 and eq 46. When the cluster size is infinitely large, $S(0)$ scattering becomes a delta function and out of the measurable q range. As the size of the cluster decreases, its form factor scattering, or shape function, will fall in the measured q range (Figure 18). Thus, for a finite sized cluster, $S(0)$ will be comprised of two parts, including both the cluster scattering, which tends to be dominant, and isothermal compressibility, which is typically weaker. Crystalline clusters will show diffraction at higher q, the width of which is dependent on the cluster size (Figure 18).

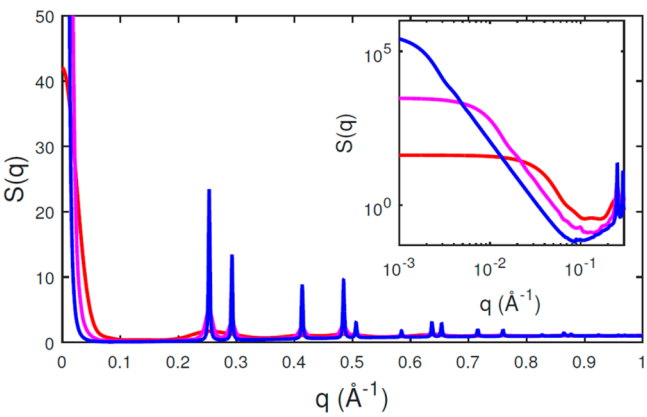

Figure 18. $S(q)$ calculated for several gold nanoparticle fcc superlattices with a lattice constant of 4.3 nm and Debye−Waller factor of 5%. The crystal habit of the superlattice is a tetrahedron with edge lengths of 20 (red), 80 (magenta), and 320 nm (blue). Inset shows enlarged view.

3.4.1.1. Monodisperse Supraparticles. A supraparticle (sometimes referred to as a superparticle)[186] is an ideal example of a particle cluster. Xia et al. studied the self-limited growth of monodisperse supraparticles composed of polydisperse primary CdSe nanocrystals.[190] In this work, both primary particle and supraparticle growth occurred simultaneously, where the particles began to form supraparticles soon after nucleation. From the SAXS data, it was revealed that the supraparticles are more monodisperse in size than their constituents. This was attributed to the fact that charge repulsion increases with the number of primary particles in a supraparticle while van der Waals attraction does not. The internal structure of the cluster did not have any ordering, which may be a result of polydispersity of the primary particles and the dominance of the attractive interaction within the cluster.

In other studies where the primary particles are highly monodisperse, it was observed that smaller clusters tend to have an icosahedral structure, which can be described by an fcc particle packing with twin boundaries. This type of structure occurs in supraparticles[187] as well as gold atomic nanoclusters.[192−194] The diffraction pattern of an icosahedral assembly is almost identical with but slightly different from that of an fcc crystal in terms of relative diffraction intensities. The Cao group fabricated the superparticles using solvophobic interactions from a variety of primary particles including spherical Fe_3O_4 (5.8 nm) and PbSe (8.3 nm), rodlike CdSe/CdS (55.4 nm in length and 4.4 nm in diameter), and cubic Fe_3O_4 (11.0 nm in edge length) nanoparticles, as shown in Figure 19. SAXS and TEM results confirmed that the internal structures of these superparticles were fcc, bcc/fcc, cylindrical disks/stacked-disk arrays, and SC. Chen et al. studied magneto-fluorescent core−shell supernanoparticles, which has a "core" made of close-packed magnetic nanoparticles surrounded by a "shell" of fluorescent quantum dots, and coated with a thin layer of silica for structural support.[188] In this case, the core−shell configuration was formed from a phase separation of quantum dots from magnetic particles in a confined micelle environment. From SAXS, they determined the structure of the close-packed particles in the core has an fcc arrangement. Rupich et al. reported that twinning is more abundant in supercrystals consisting of larger PbS nanocrystals and is not found for ones consisting of particles less than 4 nm in diameter, indicating that twinning energy is nanocrystal size dependent.[195]

3.4.1.2. Core−Shell Supraparticles. Balmer et al. calculated SAXS curves for supraparticles composed of a single large polymeric core with a monolayer shell consisting of small silica particles.[200] Chen et al. studied SiO_2/TiO_2 hollow nanoparticles with approximately 30% porosity in the wall.[201] These two seemingly different samples have substantial similarities in terms of X-ray scattering: in both cases, they have core−shell configurations consisting of smaller scatterers, either particles or pores, in the shell. The former work treated the shell particles as individual scatterers because they were relatively large. However, the latter assumed the shell was a homogeneous material with a lower density because the pores were relatively small and randomly distributed in the shell. The form factor amplitude formula for the core−shell system is written as

$$F(\boldsymbol{q}) = F_{core} + F_{shell} + \sum_{m}^{N_s} F_{sph}(\boldsymbol{q}, R_m)e^{-i\boldsymbol{q}\boldsymbol{r}_m} \tag{56}$$

where the shell is made of N_s spheres with radius R_m at position $\boldsymbol{r}_m$ for particle m. The terms F_{core} and F_{shell} are the scattering amplitudes of the spherical core and concentric shell, respectively. In the former work of Balmer et al., $F_{shell} = 0$ and the scattering contrast for the shell particle F_{sph} is $(\rho_{sph} - \rho_{solv})$, where ρ_{sph} is the scattering length density of the shell particle. In the latter example by Chen et al., the pores are too

DOI: 10.1021/acs.chemrev.5b00690
Chem. Rev. XXXX, XXX, XXX−XXX

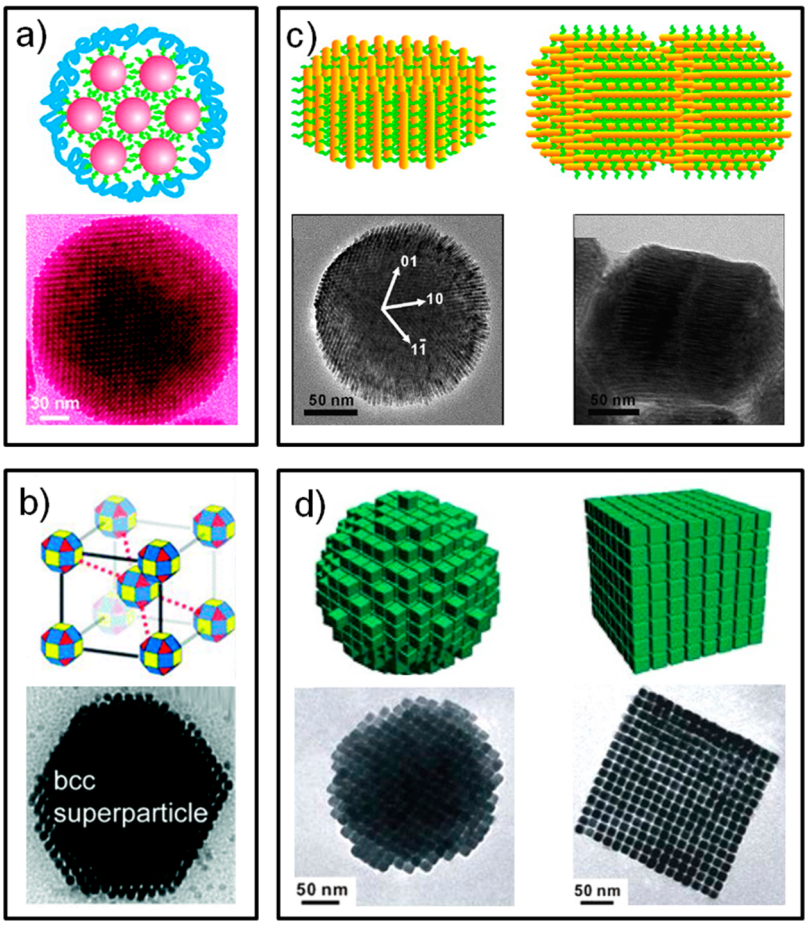

Figure 19. Superparticles made from spherical Fe_3O_4 (a) and PbSe (b), as well as rodlike CdSe/CdS (c) and cubic Fe_3O_4 (d). (a) Modified from ref 196. Copyright 2013 American Chemical Society. (b) Modified from ref 197. Copyright 2012 American Chemical Society. (c) Modified from ref 198. Copyright 2009 American Chemical Society. (d) Modified from ref 199. Copyright 2012 American Chemical Society.

small to be measured in the observed q range. Thus, they treat their system as a single core–shell particle, neglecting the last term.

When the size difference between the core particle and the shell particles is large or the surface coverage of the adsorbed particles is low, the two scatterings may add incoherently. In other words, the form factor $P(q) = P_{core} + \sum_m^{N_s} |F_{sph}(q,R_m)|^2 S_{sph}(q)$, where $S_{sph}(q)$ is the structure factor of the shell particles. For example, Goergen[202] deposited small gold nanoparticles on the surface of octahedral iron oxide nanoparticles to be used as a catalyst for oxidative dehydrogenation of cyclohexane. They determined the increase in surface area of the iron octahedral particles resulting from the small gold nanoparticles using eq 32. Christensen et al. studied atomic layer deposition of platinum nanoparticles on strontium titanate nanocubes.[203] While they found positional correlation between small platinum nanoparticles, the core–shell nature was not obvious in the SAXS data due to the high polydispersity of the large nanocubes, which presented only power law Porod scatterings in the observed q range.

Another interesting example is a polymer–bionanoparticle core–shell cluster, where the polymer is poly(4-vinylpyridine) (P4VP) and biological nanoparticles (BNPs) include cowpea mosaic virus (CPMV),[204] turnip yellow mosaic virus (TYMV),[205] rodlike tobacco mosaic virus (TMV),[206] and even proteins.[207] BNPs coat and stabilize the hydrophobic P4VP core in aqueous solutions. SAXS revealed that spherical BNPs formed a 2D hexagonal arrangement on the surface of the polymer ball and displayed tighter packing as the curvature of the ball increased. Such hexagonal packing is further confirmed from SEM images; see Figure 20b,c.

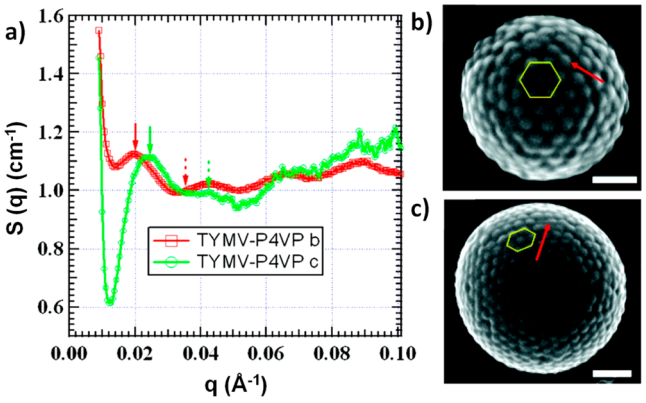

Figure 20. (a) Structure factors of two different sized TYMV–P4VP particles, where "b" and "c" refer to small and large particles, respectively. (b, c) Representative SEM images of TYMV–P4VP of samples b and c (the arrows point to packing defects). All scale bars are 100 nm. Modified from ref 205. Copyright 2009 American Chemical Society.

DOI: 10.1021/acs.chemrev.5b00690
Chem. Rev. XXXX, XXX, XXX–XXX

3.4.2. Porous Particles. Porous particles are often used for filtration, ion adsorption, and supports for catalysis.[208] The physical characteristics of the porous material, including surface area, often affect its performance. As seen from Figure 21a,

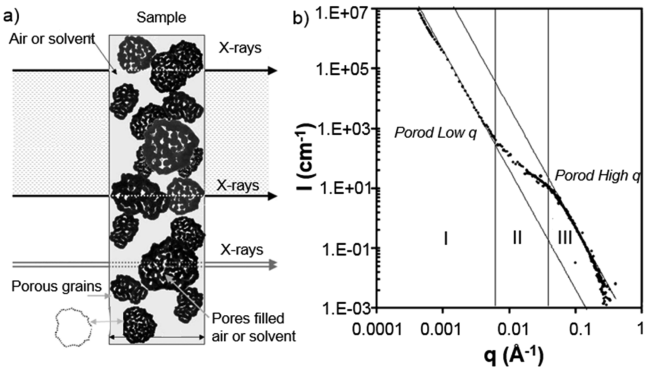

Figure 21. (a) Sample configuration in a section parallel to the beam. (b) Typical apparent intensity of a two-length-scale porous system (water-altered glass). Three regions are identified: (I) a low q Porod's law region; (II) an intermediate plateau; (III) a high q Porod's law region. (a, b) Modified with permission from ref 209. Copyright 2003 International Union of Crystallography. http://journals.iucr.org/.

porous particle can be regarded as an "inverted" cluster. Spalla et al. derived a formula similar to eq 53 but with different contrast for each term in the equation.[209] The low and high q power law slopes in regions I and III in Figure 21b correspond to the first and second terms, respectively. Their Porod constants are proportional to the external surface area S_e and surface area of the internal pores S_i, respectively. They also derived a method to calculate internal porosity form the invariant Q.[209] Chavez Panduro et al. noted that an experimental SAXS profile is measured only for a limited q range, and thus the invariant calculated from the data may not reflect the correct porosity.[210] By redefining the absolute scale of the data, they related the experimental Q to the porosity of both internal and external (that is, the spaces between the porous particles) pores.

Hollamby et al. studied mesoporous silica particles,[211] where the pores were made from CTAB micelles randomly distributed in the particle. They employed a SANS contrast variation technique to separate the contributions from the inner pore and overall particle scattering, enabling them to determine the number of micelles per mesoporous particle.[211] Further, using in situ SANS, they determined the growth mechanism; small silica oligomers adsorbed to the CTAB micelle surface, which led to a reduction of the intermicellar repulsion and resulted in micelle clustering. This aggregate forms the basis of the growing mesoporous structure.

3.4.3. Aggregates. Aggregates are typically formed when the interaction between particles is strong such that they stick upon contact and cannot rearrange to a more thermodynamically favored state. Visually, their structure may appear randomly ordered, but some may be described statistically or mathematically. In sections 3.4.3.1 and 3.4.3.2 we discuss two different types of mathematically defined aggregates.

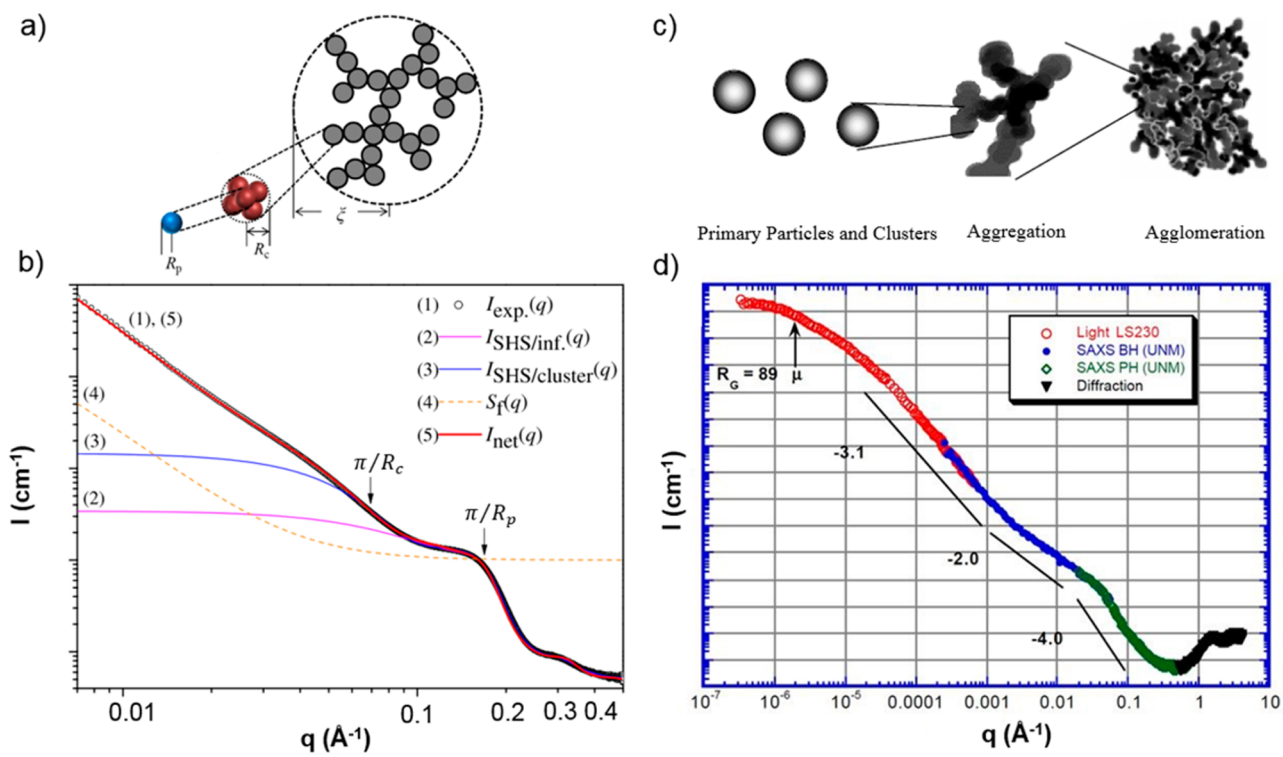

Figure 22. (a) Hierarchical assembly of palladium nanoparticles in a polymer matrix. (b) Comparison between the measured (1) and calculated (2–5) data. The structure factor (and intensity) was modeled using a sticky hard sphere (SHS) potential assuming either an infinite sized domain (inf.) or a limited sized cluster (cluster); the latter model fit the data better.[221] (a, b) Modified and adapted with permission from ref 221. Copyright 2015 AIP Publishing. (c) Schematic representation of the hierarchical structure of precipitated silica. (d) Scattering profile for precipitated silica. These data were combined from data collected on four instruments with different q ranges. (c, d) Modified and adapted with permission from ref 218. Copyright 2000 International Union of Crystallography. http://journals.iucr.org/.

DOI: 10.1021/acs.chemrev.5b00690
Chem. Rev. XXXX, XXX, XXX−XXX

3.4.3.1. Fractal Aggregates. A typical example of an aggregate structure is a fractal. In a fractal, primary particles aggregate in a way that the number or total mass of the particles is proportional to the algebraic power of a pair distance, r^{ν}, where ν is the power law exponent. This type of structure is called a mass fractal. Thus, the mean density at a pair distance r is proportional to $r^{\nu-3}$. The power law scaling varies with the type of fractal; for example, $\nu = 3$ for a 3D network of particles and 2 for a Gaussian chain. This scaling translates into a power law that can be interpreted as a Porod exponent; the scattering from a fractal is proportional to $q^{-\nu}$.[212]

Fractals have a distinctly different scattering than a homogeneous solution of concentrated particles. The number of particles in the latter system is also proportional to r^3, but q^{-3} scattering is not expected because the correlation at a long pair distance, or small q, does not exist in the homogeneous solution. This indicates that the pair distribution $g(r)$ of a fractal should have a power law at large pair distance, as will be discussed in section 4.3.2. Other fractal systems exist, including surface[212] and pore fractals.[213] From the slope of the scattering curve, it is possible to understand the mechanism of aggregation, such as reaction limited or diffusion limited growth.[214−217]

3.4.3.2. Hierarchical Aggregates. There is another type of aggregate, called the hierarchical aggregate, where the arrangement of particles varies with scale, as shown in Figure 22a,c. For example, primary particles may be arranged into clusters which in turn may be arranged into short lines. These lines may be finally assembled into dendrimer-like structures.[218] Each component of this multilevel hierarchical aggregate produces its own scattering (Figure 22b,d). In Figure 22b, we emphasize the characteristic q positions or Guinier knees of each level. The power law behaviors of each level are shown in Figure 22d. Scattering from the primary particles, the smallest building blocks, appear at the highest q region ($q > 0.1$ Å^{-1} for Figure 22b and $q = 0.04$−0.4 Å^{-1} for Figure 22d). Because the primary particles have a sharp surface, the power law scattering scales as q^{-4}, as denoted in Figure 22d. In some cases (Figure 22b), the structure factor of the primary particles can be clearly observed. In other cases (Figure 22d), it is poorly developed. At $q = 0.04$−0.07 Å^{-1} in Figure 22b and $q \approx 0.01$ Å^{-1} in Figure 22d, the scattering from the second level structures (or clusters) can be seen. The size of the clusters in Figure 22d was small and did not produce a distinct scattering. The larger aggregate (third level) scattering appears at smaller $q < 0.03$ Å^{-1} in Figure 22b and $q = 0.001$−0.01 Å^{-1} in Figure 22d. In Figure 22b, this third level scattering presents a q^{-2} power law, indicating that the clusters are aggregated into Gaussian chains. Finally, the highest level structure, the agglomerate or dendrimer-like structure shown in Figure 22c, produces the scattering at the smallest $q = 10^{-6}$−10^{-3} Å^{-1} with a $q^{-3.1}$ power law. This data suggests that the aggregates are agglomerated into a mass fractal.[96,219,220] SAXS data from these hierarchical aggregates can be fit with Beaucage's multilevel unified theory.[96]

These types of hierarchical aggregates may form by varying the environment surrounding presynthesized and stabilized colloidal nanoparticles. Robbes et al. synthesized polymer nanocomposites made of γ-Fe_3O_4 nanoparticles dispersed in a polystyrene (PS) matrix.[222] They found that γ-Fe_3O_4 nanoparticles formed hierarchical aggregates when they were transferred from an aqueous solution to a dimethylacetamide solution containing PS. Wang et al. studied in situ formation of Pd nanoparticles via thermal decomposition of organo-Pd catalyst precursors.[223] They found that Pd nanoparticles formed clusters and higher level aggregates at an early stage and further grew in size without variation of their internal arrangement at the cluster level.[223] Recently, Lin et al. studied the nature of Pd nanoparticle aggregates synthesized by reducing its precursor in poly(2-vinylpyridine) homopolymer solution.[221] By analyzing SAXS profiles of the nanocomposites using the structure factor for the sticky hard sphere potential, they found that the attractive interaction resulting in primary particle clustering and aggregation is relatively mild with a potential depth of 2.2 kT (Figure 22a,b).

4. CORRELATION FUNCTION APPROACH

So far, the scattering intensity has been treated as a product of the form factor and structure factor. In SAS, there is a method corresponding to the Patterson function in atomic diffraction, called the correlation function, $\gamma(r)$. It is the inverse Fourier transform of intensity, $I(q)$, much like $\rho(\boldsymbol{r})$ to $F(\boldsymbol{q})$. The scattering length density profile of the entire sample, $\varrho(\boldsymbol{r})$, is a convolution of a single particle density profile $\rho(\boldsymbol{r})$ and particle positional mesh or lattice $L(\boldsymbol{r})$. Thus, $\varrho(\boldsymbol{r}) = \rho(\boldsymbol{r}) \otimes L(\boldsymbol{r})$. According to the convolution theorem of Fourier transform (FT), $\mathrm{FT}(\varrho(\boldsymbol{r})) = \mathrm{FT}(\rho(\boldsymbol{r}))\,\mathrm{FT}(L(\boldsymbol{r}))$. When $\mathrm{FT}(\varrho(\boldsymbol{r}))$ is defined as $A(\boldsymbol{q})$, as is described in section 3.1, $\mathrm{FT}(\rho(\boldsymbol{r})) = F(\boldsymbol{q})$, $|\mathrm{FT}(L(\boldsymbol{r}))|^2 = S(\boldsymbol{q})$, and $|A(\boldsymbol{q})|^2 = I(\boldsymbol{q})$. The relationships between these quantities are depicted in Figure 23. Here, $I(\boldsymbol{q})$ can be replaced with $\frac{d\Sigma}{d\Omega}(\boldsymbol{q})$ when all other variables are on an absolute scale. The correlation function of $\varrho(\boldsymbol{r})$ and the scattering length density difference $\eta(\boldsymbol{r})$, which is identical to $\Delta\varrho(\boldsymbol{r}) = \varrho(\boldsymbol{r}) - \bar{\varrho}$, are $\Gamma(\boldsymbol{r})$ and $\Gamma_\eta(\boldsymbol{r})$, respectively.[17,25]

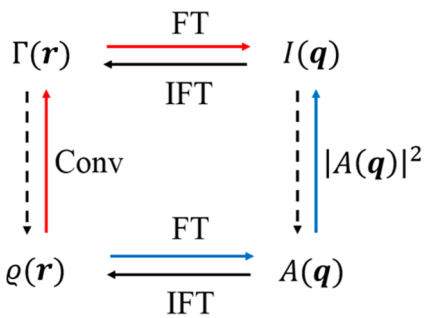

Figure 23. Relationship between $\Gamma(\boldsymbol{r})$, $\varrho(\boldsymbol{r})$, $I(\boldsymbol{q})$, and $A(\boldsymbol{q})$. FT stands for Fourier Transform, IFT is inverse FT, and Conv is convolution. The broken lines indicate nontraversable pathways unless further information is known.

$$\Gamma_\eta(r) = \langle \Gamma_\eta(\boldsymbol{r}) \rangle = \langle \int \eta(\boldsymbol{r})\, \eta(\boldsymbol{r} + \mathbf{u})\, \mathrm{d}\mathbf{u} \rangle \tag{57}$$

where $\boldsymbol{r}$ in the correlation function denotes a distance vector, although the same notation denotes a position vector for ϱ. According to eq 57, $\Gamma_\eta(0) = \overline{\eta^2}V$, where $\overline{\eta^2}$ is the mean square fluctuation of the scattering length about its mean throughout the sampling volume V. From the Fourier transform relationship between $I(\boldsymbol{q})$ and $\Gamma_\eta(\boldsymbol{r})$

$$I(\boldsymbol{q}) = V\,\frac{\mathrm{d}\Sigma}{\mathrm{d}\Omega}(\boldsymbol{q}) = \int \Gamma(\boldsymbol{r}) \mathrm{e}^{-i\boldsymbol{q}\boldsymbol{r}}\, \mathrm{d}\boldsymbol{r} = \int \Gamma_\eta(\boldsymbol{r}) \mathrm{e}^{-i\boldsymbol{q}\boldsymbol{r}}\, \mathrm{d}\boldsymbol{r} + \bar{\varrho}^2 V \delta(\boldsymbol{q}) \tag{58}$$

DOI: 10.1021/acs.chemrev.5b00690
Chem. Rev. XXXX, XXX, XXX−XXX

where δ is the delta function indicating $\bar{\varrho}^2 V\delta(\boldsymbol{q})$ is not observable in the experimental $\boldsymbol{q}$ ranges and is thus normally neglected. Often the normalized correlation function $\gamma(\boldsymbol{r}) = \Gamma_\eta(\boldsymbol{r})/\Gamma_\eta(0)$, referred to as the Debye correlation function,[65] is used when SAXS data is in an absolute scale. For an isotropically oriented system[65]

$$\frac{d\Sigma}{d\Omega}(q) = \int 4\pi r^2 \gamma(r) \frac{\sin(qr)}{qr}\, dr \tag{59}$$

Note that the distance r is a pair distance, not a position. The relationships among these quantities are summarized in Figure 23. From the definition of the invariant (eq 33) and eq 59, $Q = \overline{\eta^2}$. For a two phase system, $\overline{\eta^2} = \phi_1(1 - \phi_1)(\Delta\rho)^2$.

Various structural parameters can be extracted from the correlation function calculated from the SAXS intensity profile using eq 59. In sections 4.1−4.3, however, we limit our interest to modeling the correlation function.

4.1. Correlation Function from Experimental Data

Analysis of the correlation function $\gamma(r)$ has been frequently performed in polymer scattering to calculate, for example, mean sizes of phase separated domains and the thickness of their interface.[224] In solution scattering, instead of the correlation function, the pair distance distribution function, $p(r) \equiv r^2\gamma(r)$, has been used to determine particle shape[16,225] or internal structure.[226] As mentioned in section 3.2.1.3, this method is more common in solution SAXS of biological objects such as proteins that are identical in size and shape. Nanoparticles typically have some polydispersity, but as they become monodisperse, there is an opportunity to use this technique. For example, Moglianetti et al. calculated $p(r)$ from SANS data measured for gold nanoparticles coated with mixed ligands of C6 and C12 thiols.[82] By deuterating either the C6 or C12 ligands, they made two identical samples with different contrasts. Low resolution models were reconstructed ab initio by simultaneously fitting experimental $p(r)$ functions to reveal striped patterns of C6 and C12 on the gold surface.

Since experimental data are measured for a limited q range, $p(r)$ is typically calculated using Glatter's indirect method,[227] not by directly Fourier transforming with eq 59. Then, the experimental $p(r)$ can be compared to a computed one from a model object. Glatter showed various $p(r)$ functions for different shapes including dimers.[228] In sections 4.1.1 and 4.1.2, we will review some recent applications of $p(r)$ or $\gamma(r)$ functions.

4.1.1. Comparing Correlation Function with Simulations. Buchkremer et al. studied clusters of DNA−AuNPs.[229] They functionalized two sets of 15 nm Au nanoparticles with complementary DNA sequences. A cluster was formed by adding the particles in various ratios. By comparing $p(r)$ as determined from SAXS data with Monte Carlo simulations, they discovered that a single cluster contained eight to nine particles surrounding the centralized core particle. Thus, the degree of packing for a single cluster is as high as a bcc crystal.[57,58]

The pair distance distribution function $p(r)$ has also been used to determine the conformation of dimeric particles.[230] Yin et al. linked two polyoxometalate (POM) particles with a 2,2′-bipyridine unit that has been reported to show an allosteric *trans* to *cis* conformational transition upon the coordination of metal ions. Indeed, they observed the conformational transition of POM dimers using $p(r)$ by adding Zn^{2+} ions to the solution. The conformation was determined by comparing experimental $p(r)$ with those calculated from models derived from the crystal structure of the dimer (Figure 24).

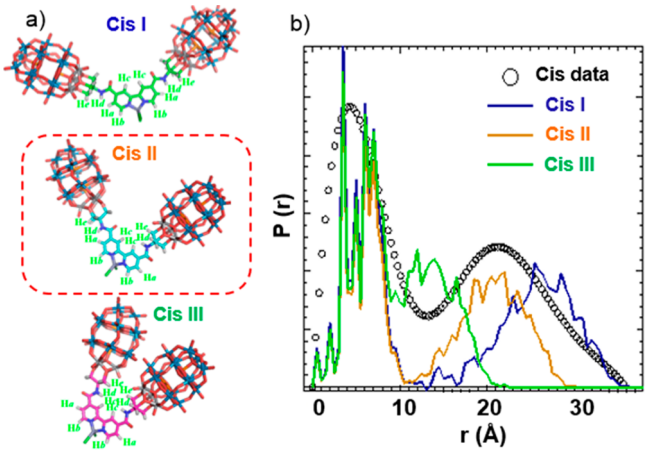

Figure 24. (a) Calculated structures of the three possible conformations that can be generated by rotation around the C3−C4 bonds for the *cis* dumbbell. (b) The calculated $p(r)$ functions were computed directly from the molecular coordinates using the program SolX.[231] The calculated $p(r)$ functions of the three possible *cis* conformations are overlaid with the experimentally derived $p(r)$ of the *cis* dumbbell. Modified from ref 230. Copyright 2013 American Chemical Society.

4.1.2. Model Analysis with Atomic PDF. Recently the SAXS correlation function has been used to aid in the analysis of atomic PDF. In an atomic PDF experiment, the WAXS is measured for a limited q range (see Figure 25a) because of experimental constraints. Thus, a PDF calculated from the WAXS data, $G(r)$, is not the same with the theoretically calculated PDF, $G^*(r)$, from a full atomic model that contains the particle shape information. Indeed, the experimental $G(r)$ is related to the theoretical $G^*(r)$ as[232,233]

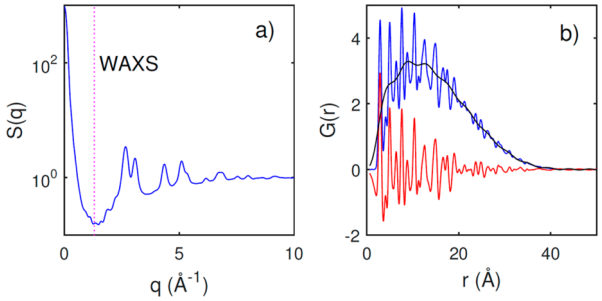

Figure 25. (a) Simulated $S(q)$ of a tetrahedral gold nanocrystal with an edge length of 5 nm and 5% Debye−Waller factor using the Debye formula (eq 9). (b) Atomic PDF (blue) calculated from $S(q)$ in (a) using eq 42. $G(r)$ in red is calculated with the WAXS part of $S(q)$ (higher q than dotted line). Black curve is $4\pi r n_p \gamma(r)$.

$$G(r) = G^*(r) - 4\pi r n_p \gamma(r) \tag{60}$$

The red curve in Figure 25b corresponds to $G(r)$ calculated from the WAXS data in Figure 25a, while the black and blue curves are $4\pi r n_p \gamma(r)$ and $G^*(r)$, respectively. Previously, in the atomic PDF literature, the particles were assumed to be simple geometric shapes, which could be modeled using analytical formulas.[233−235] Recently, some have begun to use the

DOI: 10.1021/acs.chemrev.5b00690
Chem. Rev. XXXX, XXX, XXX−XXX

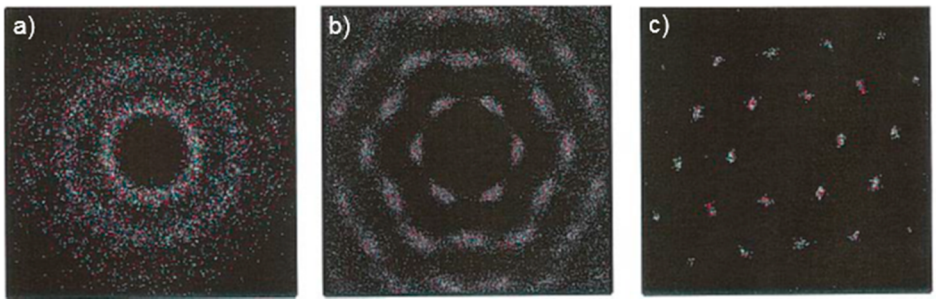

Figure 26. Computed 2D structure factor corresponding to the pure liquid (a), hexatic (b), and crystal (c) phases. Adapted with permission from ref 241. Copyright 1996 American Physical Society.

experimentally determined shape derived from SAXS for a more accurate shape correction.

Hua et al. used the correlation function obtained from SAXS data to determine the shape of TiO_2(B) nanoparticles used as a material for Li ion battery anodes.[232] The particles were highly agglomerated when dried, which prevents them from getting representative particle shape information from microscopy. Because of polydispersity, SAXS data could be fit to several spheroid models, yielding inconclusive results regarding particle shape. However, after they subtracted $\gamma(r)$ for each of the spheroid models from $G^*(r)$, the resulting $G(r)$ values were distinctively different. Comparison with experimental $G(r)$ allowed them to determine particle shape.

Gagin et al. also explored the combination of SAXS and PDF in the analysis of particles of various morphologies including core−shell and spherical particles.[236] They found that incorporating SAXS data into the fit consistently returned more robust results than those obtained by fitting the WAXS data alone. Additionally, real space fits of the atomic PDF using $\gamma(r)$ from SAXS data produced more accurate results than those obtained using approximate analytical expressions. Similarly, Farrow et al. also co-refine SAXS and PDF data for elliptical CdS nanoparticles to extract out reliable structural parameters such as the radii along the long and short axes.[126]

4.2. Particle Positional Correlation Analysis

Previously in section 3.3.1, we compared the indirectly and directly determined $g(r)$ from an SEM image and SAXS data, respectively (Figure 14). Likewise, the correlation function $\gamma(\boldsymbol{r})$ can also be computed from an SEM or TEM image. Pichler et al. analyzed the correlation function to quantitatively discuss the degree of ordering: long-range ordering vs short-range ordering.[237]

Two-dimensional nanoparticle assemblies have three representative phases—liquid, liquid crystal, and crystal—as shown in Figure 26. For these 2D structures, the Kosterlitz−Thouless−Halperin−Nelson−Young (KTNHY) theory has been developed to distinguish between these phases.[238−240] The KTNHY theory predicts that a 2D crystal will have a correlation function that decays algebraically or as $r^{-\eta_G}$, where η_G is called the KTNHY decay exponent.[239] In this case, diffraction peaks from an infinite size single crystal domain can be described as a power law (Figure 27).

$$S(\boldsymbol{q}) \propto \frac{1}{|\boldsymbol{q} - \boldsymbol{G}|^{2-\eta_G}} \tag{61}$$

where $\eta_G \propto |\boldsymbol{G}|^2$, and $\boldsymbol{G}$ is the reciprocal lattice vector. In reality, the singularity at $\boldsymbol{G}$ is not observed due to the limited size of the crystal (Figure 27). Please note that when the crystals are randomly oriented in 2D or 3D, the corresponding Lorentz factor should be applied.[39]

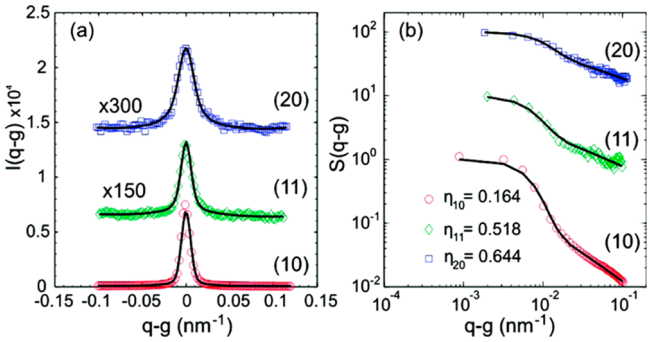

Figure 27. Shapes of diffraction peaks (10), (11), and (20) of 2D hexagonal assemblies of spherical gold nanoparticles in (a) linear scale and (b) log−log scale. Solid lines are fits to the KTNHY theory. The power law tails can be seen in (b). Adapted from ref 240. Copyright 2010 American Chemical Society.

When the crystal transforms to a hexatic phase (the liquid crystalline phase for 2D hexagonal crystals), the correlation function becomes exponential, $e^{-r/\xi}$, where ξ is the correlation length.[241,242] The shape of the single crystal structure factor peak becomes a Lorentzian for the hexatic phase.[241,243] Finally, for the liquid phase, the orientational correlation will disappear.

4.3. Analytical Correlation Function Model

In this section, we will introduce several analytical correlation function models. Scattering equations based on these models can be obtained by Fourier-transforming the correlation functions using eq 58 and are not presented to simplify the discussion.

4.3.1. Arbitrary Shaped Particles. When the shape of a particle is not a simple geometric object, it may be easier or more physically meaningful to describe the object with a correlation function. Otherwise, computing the scattering intensity from the complex object would require making a series of computations, building up a real space model, computing its scattering, and performing orientational averaging. Instead, a certain functional form that can provide a statistically meaningful understanding of the particle can be used for its correlation function. One of the simplest correlation functions is

$$\gamma(r) = e^{-r/\xi} \tag{62}$$

where ξ is the correlation length. Equation 62 dictates that the correlation decays exponentially with distance, leading to the Debye−Bueche formula[65]

DOI: 10.1021/acs.chemrev.5b00690
Chem. Rev. XXXX, XXX, XXX−XXX

$$\frac{d\Sigma}{d\Omega}(q) = \frac{8\pi(\Delta\rho)^2\phi_p\xi^3}{[1 + (q\xi)^2]^2} \tag{63}$$

which is derived using eq 59. This formula has been successfully used to fit SAXS data from morphologies such as phase separated structures. Additionally, in the literature of colloidal particles, this function has been used to represent the scattering from large clusters[13,141] (see section 3.4). When the smallest q region of this equation is approximated as a Gaussian function, one can obtain the relation $R_g = \sqrt{6}\xi$.

4.3.2. Fractal Particles. When infinitely small objects are aggregated to form a fractal object with a finite size ξ, i.e. an aerosol, the correlation function can be written with an exponential cutoff function as[244]

$$\gamma(r) = r^{D_f-3}e^{-r/\xi} \tag{64}$$

This correlation function dictates that at short distances $\gamma(r)$ will show power law behavior r^{D_f-3}, which suggests that this correlation represents a fractal structure (see section 3.4.3). Here, D_f is the fractal dimension. For simplicity, the intensity equation is not presented, though the interested reader can find it elsewhere.[212]

More recently, Besselink and ten Elshof used a step function, or Heaviside function H, as[215]

$$\gamma(r) = r^{D_f-3}H(\xi - r) \tag{65}$$

where the exponential function and H represent the particle size and internal structures, respectively. In addition, they used the Schultz−Zimm distribution function for the distribution of ξ. They found that the intensity formula derived from this correlation function successfully fit the scattering of silicate particles that possessed a mass fractal-like internal structure. Further, they were able to determine the size distribution. We remind the reader, as in section 3.2.2.2, one should not analyze the scattering of this type of porous particle (which shows fractal Porod scattering at high q) using a polydisperse sphere model for solid objects with sharp interfaces.

4.3.3. Correlation Functions with Structure Factor. The analytical correlation functions reviewed thus far all correspond to single, dilute particles. There is no increase of correlation at a distance larger than the particle size. Thus, these models are not applicable to concentrated particle solutions where particle−particle correlation is expected. Take for example, a colloidal solution, with particles that are homogeneously distributed with interparticle distances longer than twice their diameter (Figure 28a). In this case, the correlation will exponentially decay as the pair distance r increases from 0 to the diameter D of the particle. The correlation will reach a minimum for distances larger than the particle diameter. Yet, in our dense colloidal nanoparticle system, the correlation will increase at a distance equal to the gap distance between nearest neighbor particles and reach a maximum at approximately the center-to-center or interparticle distance (Figure 28b). The correlation will eventually oscillate with a periodicity corresponding to the interparticle distance. Unless the nanoparticles are located on some lattice, the interparticle distances will fluctuate and thus the oscillation in the correlation function will quickly damp out.

From this picture, Teubner and Strey[245] derived the scattering intensity theory based on Ginzbug and Landau free energy expansion and related it to a correlation function of

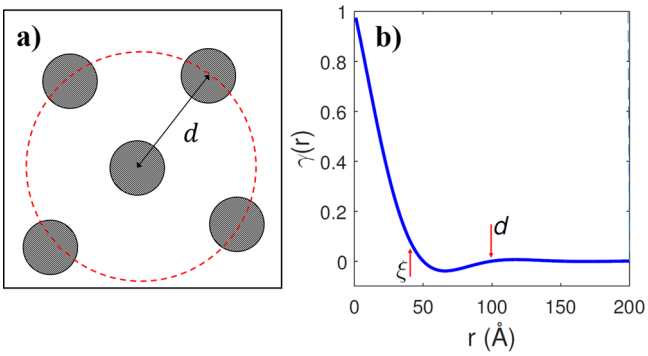

Figure 28. (a) Enlarged view of homogeneous particle solution, showing an average distance between particles. (b) Correlation function calculated using eq 66.

$$\gamma(r) = \frac{d}{2\pi r}e^{-r/\xi}\sin\left(\frac{2\pi r}{d}\right) \tag{66}$$

where ξ is a correlation length corresponding to the particle size, and d is the periodicity. The intensity of this correlation function shows a broad peak at $q = 2\pi/d$ and a power law scaling of q^{-4} at high q. This function, called the Teubner and Strey model, was originally developed to represent the structure of micelle systems,[245] and has been applied to phase separation systems.[246,247] This model also turned out to be appropriate for bicontinuous phase separated systems.[246] One may notice that the Debye−Bueche model is a special case of the Teubner and Strey model for very large d ($d \gg \xi$).

Within certain limitations, this correlation function approach can be applied for highly polydisperse irregularly shaped nanoparticle systems that contain one broad peak with Porod scaling of q^{-4}. For such a system, this approach has several advantages over particulate theory dealing with the form factor and structure factor separately. First, it is unnecessary to average the form factor using a polydispersity size distribution, and second, it circumvents the limitations of the DA or LMA (see section 3.1).

5. COMBINATION OF SCATTERING WITH MODEL SIMULATIONS

When the coordinates of each atom in a particle or a system are available, it is possible to compute the scattering profile over a large q range that covers both SAXS and WAXS regions (eq 7). In this case $F_l(\boldsymbol{q})$ and $\boldsymbol{r}_l$ become the atomic scattering factor and position of atom l, respectively. As an alternative to eq 7, Debye's formula can be used for randomly oriented particles.[248] There are numerous papers to efficiently simulate the scattering pattern from a model.[38,249−254] However, it is worth noting that Noyan et al. reported that structure refinement with the formula for nanoparticles less than 10 nm may require some caution.[255] Of course, this type of characterization is possible thanks to the advance of synthetic methods leading to highly monodisperse nanocrystals.

5.1. SAXS Simulation Using Atomistic Models

In the field of structural biology, the solution structures of identical proteins are often assumed to be identical to each other. Thus, the solution SAXS profiles can be calculated using the atomic coordinates available from the Protein Data Bank and software programs such as Crysol by Svergun.[38] He and co-workers also developed ab initio structural refinement algorithms to determine the shape of a protein molecule,

DOI: 10.1021/acs.chemrev.5b00690
Chem. Rev. XXXX, XXX, XXX−XXX

called the molecular envelope.[16] The algorithm employs dummy atoms, the coordinates of which are then optimized to determine this molecular envelope. It is important to examine the structure in solution not only because there are many biological molecules that cannot be easily crystallized but also because the solution structure may not be the same as its crystal structure. There have also been attempts to combine SAXS with molecular dynamics simulations, primarily for biological materials, although this is outside the scope of this review. For further information see the recent review by Liu et al.[80]

When the shape of a particle can be mathematically defined, i.e. for a superball[162] or polyhedron, the form factor can be calculated numerically by discretizing the inner space of the particle into volumes smaller than the SAXS resolution. Young et al. calculated the form factors of truncated polyhedral particles using Monte Carlo methods.[70] The Monte Carlo method can also be used for various systems including polymers and particles whose structures are statistically defined or their shape function cannot be easily integrated with eq 12.[69]

5.2. SAXS and WAXS: Total Scattering Simulations

As monodisperse particles become available, the use of the Debye formula for WAXS analysis in reciprocal space becomes more realistic because the requirement for statistical averaging for size and shape distribution can be relaxed.[256,257] Recently Murray's group demonstrated use of the Debye formula for various monodisperse polyhedral particles over a full q range (from SAXS to WAXS) by employing an algorithm that enhanced computational time.[67] Fleury et al. also fitted both SAXS and WAXS data using coordinates from molecular dynamics simulations. They determined the relative contributions from three different particle shapes using a linear combination to fit the data (Figure 29).[193]

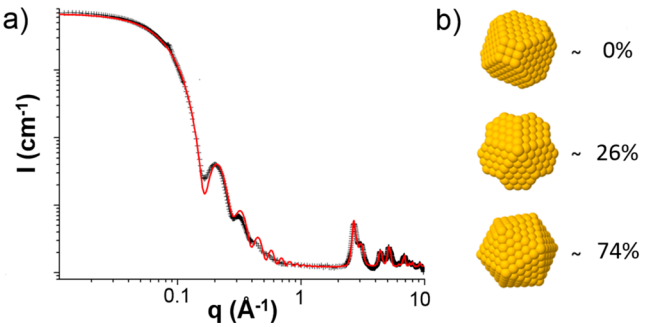

Figure 29. (a) Experimental and calculated SAXS for 5.4 nm AuNPs. The best fit is obtained from a linear combination of the calculated scattering intensities of three different external shapes, including icosahedra, decahedra, and truncated octahedral structures shown in (b). Reprinted from ref 193. Copyright 2015 American Chemical Society.

6. GISAXS

When particles are deposited as a film on a substrate, it is often useful to consider sample analysis in grazing incidence geometries (i.e., grazing incidence small-angle X-ray scattering, GISAXS) instead of transmission SAXS. In this case, transmission mode means placing the sample normal to the beam. There are several advantages to using GISAXS. First, it can provide up to a factor of 1000 times higher intensity than measuring the same sample in transmission mode due to the increase in X-ray path length of the beam through the particle film. Further, transmission mode SAXS requires a high X-ray energy to pass through the substrate. On the other hand, the X-ray does not need to penetrate the substrate in GISAXS. In addition, structural information along the z-direction (normal to the substrate) can be measured using GISAXS. This capability is necessary to determine, for example, the lattice constants of 3D nanostructures,[168] and the height and shape of nanoparticles deposited on a substrate.[258,259]

6.1. Reflection and Refraction in GISAXS

To make use of the advantages of GISAXS, a sample needs to be measured in a reflection mode, where the incident angle is close to 0°. For shallow incident angles, two optical effects appear: reflection and refraction. When an X-ray impinges on a layer of particles or a film, it may be totally reflected if the incident angle is shallower than the critical angle of the film (Figure 30a and Figure 31a). Some small fraction of the beam

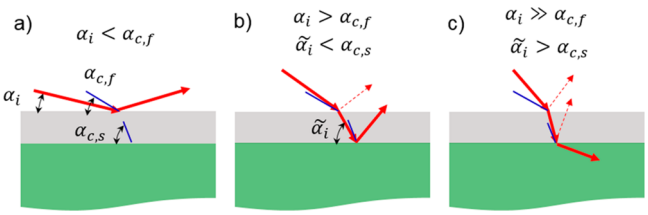

Figure 30. Propagation of an X-ray beam through a thin particle film as a function of incident angle. Purple lines denote the critical angles of film, $\alpha_{c,f}$, and substrate, $\alpha_{c,s}$. The red solid arrows depicts the majority of X-ray flux and the dotted arrows show minor flux due to reflection. The incident angle is α_i and the refracted incident incident angle in the film is $\tilde{\alpha}_i$. (a) α_i is lower than $\alpha_{c,f}$. (b) α_i is higher than $\alpha_{c,f}$, but still $\tilde{\alpha}_i$ is lower than $\alpha_{c,s}$. (c) α_i and $\tilde{\alpha}_i$ are higher than $\alpha_{c,s}$.

may penetrate the top thickness, depending on the X-ray energy, the material's mean refractive index, and the incident angle. As the incident angle increases above the critical angle of the film, the full X-ray flux will penetrate into the film with a slight refraction according to Snell's law, scatter off the particle layer, and eventually arrive at the detector.

If the nanoparticle film is optically thin (that is, it will not absorb a significant fraction of the X-ray beam), the majority of the incoming photons will not get absorbed but instead propagate through the film to the substrate surface (Figure 30b and Figure 31b,c). This is because of the high penetration power of X-rays. If the electron density of the substrate is higher than that of the film, the X-ray beam will again be totally reflected from the interface between the layer and substrate, depending on the incident angle. The reflected X-ray photons will then propagate back through the film, scattering off particles on the way out. When the scattered beam comes out of the film with a shallow incident angle, the scattered X-ray passing through the interface will also be refracted, changing the propagation direction. Any analysis of GISAXS must take account of both reflection and refraction.

When the incident angle (α_i) is greater than the critical angle (α_c) of the substrate, the X-ray beam will not reflect at the film/substrate interface (Figure 30c and Figure 31d). As the incident angle increases, both reflection and refraction become negligible according to Snell's law.

Although we have briefly described these phenomena based on the incident beam, the scattered beams can be reflected and refracted depending on their propagation angle to the interface.

DOI: 10.1021/acs.chemrev.5b00690
Chem. Rev. XXXX, XXX, XXX−XXX

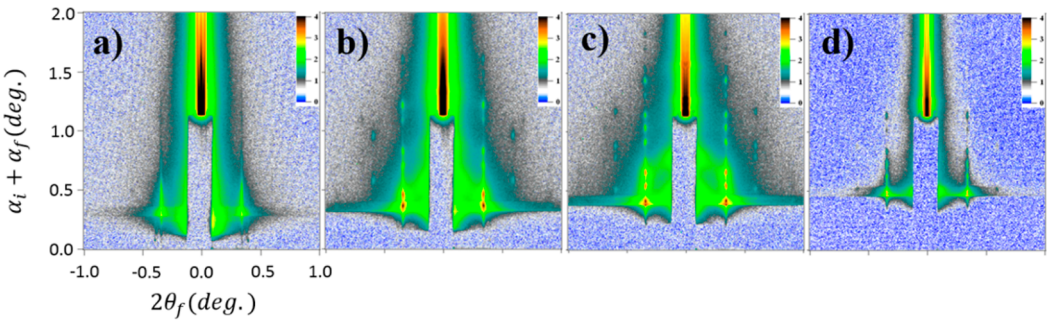

Figure 31. GISAXS data from a PS−PI block copolymer film with a hexagonally perforated lamella morphology. Data are measured at various incident angles: (a) 0.12° ($\alpha_i < \alpha_{c,f}$), (b) 0.16 and (c) 0.22° ($\alpha_{c,f} < \alpha_i < \alpha_{c,s}$), and (d) 0.3° ($\alpha_i > \alpha_{c,s}$). Axis scales in (b)−(d) are identical to the ones in (a). Detailed description about the measurement condition can be found elsewhere.[152]

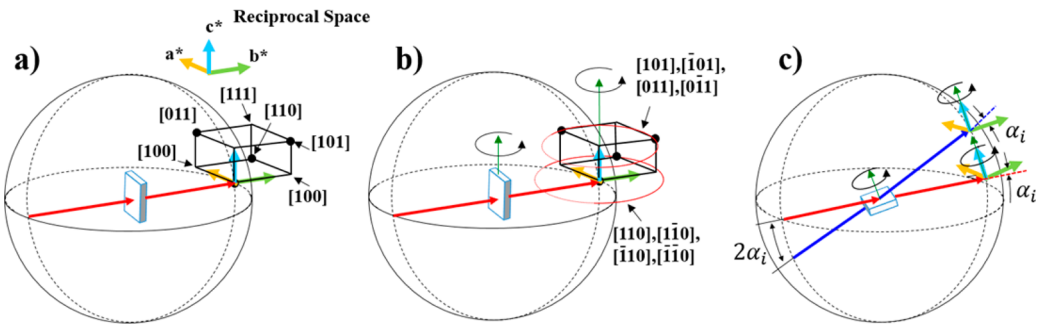

Figure 32. (a, b) Ewald spheres in transmission SAXS. (a) A bcc crystal is mounted so that its (100) and (001) planes are parallel to *x* and *z*, respectively, and the reciprocal lattice is drawn on the Ewald sphere. (b) The bcc crystal is randomly oriented in the *xy*-plane, which produces a 2D powder diffraction pattern. The green arrows depict the rotation axes *c* and *c** for real space and reciprocal space, respectively. (c) GISAXS Ewald sphere of a 2D powder bcc crystalline film. The crystals on the substrate are randomly oriented around the *z*-direction (green arrow, *c**, parallel to the substrate normal vector). The blue line represents the reflected beam while the red line represents the direct beam, indicating there are two reciprocal spaces, each rotated around *c** as a result of the of 2D random orientation.

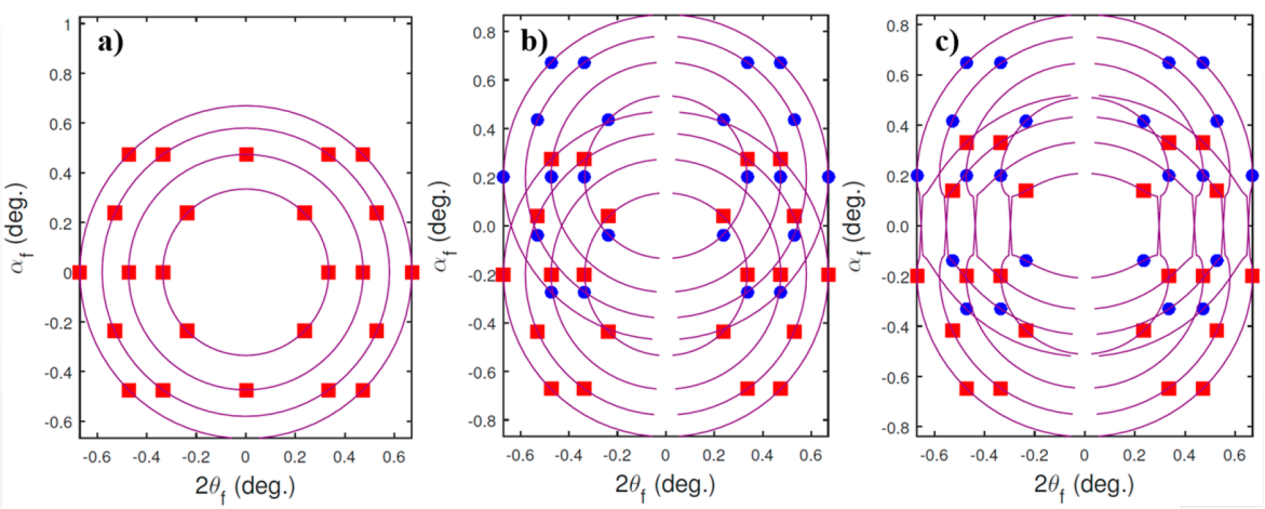

Figure 33. Simulation of 2D powder GISAXS indexing for a bcc crystal with a lattice constant of 30 nm oriented such that the (001) plane is parallel to the substrate. The X-ray energy is 10 keV. (a) When $\alpha_i = 0$, the diffraction pattern corresponds to Figure 32a (transmission SAXS). When the peaks are sharp, the two peaks at $2\theta_f = 0$ will not be detected because they are not on the Ewald sphere. (b) GISAXS indexing with $\alpha_i = 0.2°$ and no refraction. (c) GISAXS indexing with the $\alpha_i = 0.2°$ as in (b) but including refraction due to the film's electron density (0.3 Å^{-3}).

These effects will be treated theoretically in the following sections.

6.2. Indexing with Two-Beam Diffraction

In 2005,[149] Lee et al. described a two-beam approach that could be used to understand the GISAXS of 3D nanostructures that included nanostructured films[149,174] and thin layers of particles.[168,260] This innovative approach employed the concept of multiple beam diffraction theory.[261] In this respect, GISAXS could be represented as the superposition of two sets of scatterings, one for the original incident beam (the "transmitted beam" generating a reciprocal space $\boldsymbol{q}_t$), and one for the beam reflected from the substrate (the "reflected beam" generating a reciprocal space $\boldsymbol{q}_r$).[149] This concept allowed researchers to

DOI: 10.1021/acs.chemrev.5b00690
Chem. Rev. XXXX, XXX, XXX−XXX

index diffraction peaks in GISAXS using the equivalent of two incident beams.[40,168,262−265] In other words, there would be two reciprocal spaces on the Ewald sphere (Figure 32).[152]

Aside from the effects of reflection and refraction, the general procedure of indexing GISAXS diffraction peaks is quite similar to other types of diffraction. Since GISAXS is used to characterize films or layered particle systems, many of these samples have some preferred orientation with respect to the surface normal; they often show a 2D powder, or fiber texture. Figure 33 compares the SAXS and GISAXS indexing of the diffraction pattern that would be expected for a bcc lattice with 2D powder symmetry, where the [001] vector is oriented along the z-axis (see Figure 32b). As a result of the fiber symmetry, most peaks will cut the Ewald sphere twice: one on the left of the z-axis and the other on the right (Figure 33). Because of the two-beam effect in GISAXS, there should be two sets of diffraction peaks separated by $2\alpha_i$ along the z-axis. For example, the centers of the two reciprocal spaces are separated by 0.4° along the vertical direction in Figure 33b. This separation can be seen from the location of the diffraction peaks originating from the transmitted beam (red squares) compared to the reflected beam (blue circles). To a first approximation (without refraction), the pattern of peak positions originating from the direct and reflected beam is identical, but shifted vertically relative to each other (Figure 33b). The pattern is also identical to the transmission SAXS pattern, again neglecting refraction. When the refraction is considered (Figure 33c), there will be slight vertical shifts in peak position. This effect is greater at lower α_f angles, or when the diffraction angle is shallower. This in turn enables us to determine the refractive index of the film, which is linearly related to the film's electron density.[149,168]

6.3. Distorted Wave Born Approximation (DWBA) Analysis

In 1989, Levine et al. reported the first use of GISAXS to study of early growth stage of gold nanoparticle vapor deposited on glass.[266] GISAXS was quickly adapted by researchers studying UHV deposited particles on flat substrates such as silicon or glass.[41,258,267−270] At that time, major theoretical developments[41,267−269] were established that employed the distorted wave Born approximation (DWBA)[271] used for surface roughness analysis. In brief, the DWBA assumes that the incident and reflected X-ray waves will interfere to form a standing wave. The standing wave then serves as the incident wave, which scatters off of the nanostructures on the substrate. Lee et al. demonstrated successful use of the DWBA for studies of thin films containing homogeneously distributed spherical nanopores.[11,272,273] The approach assumed the nanostructured film to be a homogeneous layer when computing the wave field, and has been used in 3D nanoparticle superlattice studies (Figure 34a).[168]

When nanoparticles, or scatterers, are not randomly distributed along the z-direction, i.e. they form a monolayer, the top of the particle may feel a different wave field from the middle or bottom. Lazzari et al.[274] and Jiang et al.[275] calculated the particle form factor by slicing particles, for example slicing a spherical particle into a stack of disks and applying a different wave field to each disk (Figure 34b). When particles form a monolayer at a uniform distance above the substrate surface, the GISAXS data will display interference oscillations along the vertical direction, or z-direction, whose frequencies are inversely related to the distance between the substrate and the particle layer, called the wave guiding effect.[275−277] Films that are homogeneously filled with particles may show

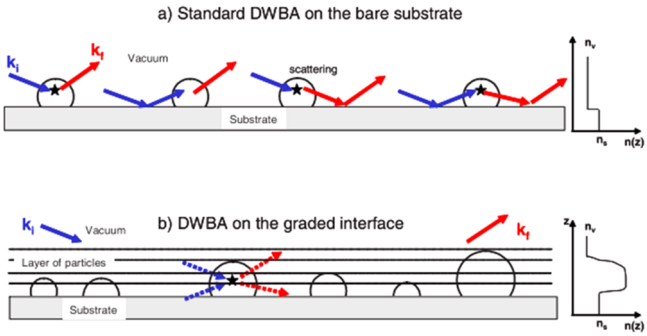

Figure 34. (a) Side view depicting the four DWBA terms of scattering, $\boldsymbol{k}_i \rightarrow \boldsymbol{k}_f$ from a single island. The blue arrow indicates the incident beam whose wave vector is $\boldsymbol{k}_i$, and the red arrow indicates the scattered beam whose wave vector is $\boldsymbol{k}_f$. (b) Slicing method. Reprinted with permission from ref 164. Copyright 2007 American Physical Society.

oscillations whose frequency is related to the film thickness,[168,260,272] known as the Kiessig fringe. Interested readers are referred to the review by Renaud et al. for further details regarding theoretical advancements.[3] See also references related to polymer films,[278] software programs,[41,43,68,165,279] and recent technical developments.[280]

The full DWBA equation is

$$I_{1\mathrm{DWBA}}(\boldsymbol{q};\, \boldsymbol{q}_t,\, \boldsymbol{q}_r) = \frac{1}{N_p}\left|\sum_{l=1}^{N_p} (T_i T_f F_l(\boldsymbol{q}_t)e^{-j\boldsymbol{q}_t \boldsymbol{r}_l} + R_i T_f F_l(\boldsymbol{q}_r)e^{-j\boldsymbol{q}_r \boldsymbol{r}_l} + T_i R_f F_l(\boldsymbol{q}_r')e^{-j\boldsymbol{q}_t' \boldsymbol{r}_l} + R_i R_f F_l(\boldsymbol{q}_t')e^{-j\boldsymbol{q}_t' \boldsymbol{r}_l})\right|^2 \quad (67)$$

where T_x and R_x are the transmitted and reflected wave amplitudes in a layer where particle l is located. The wave amplitudes are significantly enhanced in angular regions between the critical angles of both film and substrate, as in Figure 30. This phenomenon, first shown by Vineyard,[281] results in a horizontal stripe of the enhanced intensity between the critical angles as in Figure 31, and is called the Yoneda wing.[282] The subscript x = i and f stands for the incident (initial) and outgoing (final) X-ray beams. We remind the reader that, for GISAXS, there are two reciprocal spaces (vide supra). The origin of the first reciprocal space is the direct transmitted beam position, represented as $\boldsymbol{q}_t = (q_x, q_y, q_{t,z})$, while the second reciprocal space has its origin at the reflected beam position and is represented as $\boldsymbol{q}_r = (q_x, q_y, q_{r,z})$ (Figure 32). In eq 67, $\boldsymbol{q}_t' = (q_x, q_y, -q_{t,z})$ and $\boldsymbol{q}_r' = (q_x, q_y, -q_{r,z})$. The definition of $\boldsymbol{q}_t$ and $\boldsymbol{q}_r$ as well as angles α_i, α_f, and $2\theta_f$ are found in the literature.[149,152,276] Propagations of X-ray photons associated with the four terms in eq 67 are shown in Figure 34a. The first term depicts scattering events where both incoming (whose wave vector is $\boldsymbol{k}_i$) and scattered (whose wave vector is $\boldsymbol{k}_f$) beams do not interact with the substrate surface. The other three terms represent the cases where incoming or scattered beams (or both) bounce off the substrate surface.

6.3.1. Two-Dimensional (2D) Structures. For 2D monolayers, the in-plane structure factor can be separated:

DOI: 10.1021/acs.chemrev.5b00690
Chem. Rev. XXXX, XXX, XXX−XXX

$$I_{1\mathrm{DWBA}}(\boldsymbol{q};\, \boldsymbol{q}_t,\, \boldsymbol{q}_r) = \frac{1}{N_p} S(q_{\parallel}) \left| \sum_{l=1}^{N_p} \left(T_i T_f F_l(\boldsymbol{q}_t) e^{-j\boldsymbol{q}_{t,z} \boldsymbol{r}_{l,z}} + R_i T_f F_l(\boldsymbol{q}_r) e^{-j\boldsymbol{q}_{r,z} \boldsymbol{r}_{l,z}} + T_i R_f F_l(\boldsymbol{q}_r{}') e^{j\boldsymbol{q}_{r,z} \boldsymbol{r}_{l,z}} + R_i R_f F_l(\boldsymbol{q}_t{}') e^{j\boldsymbol{q}_{t,z} \boldsymbol{r}_{l,z}} \right) \right|^2 \tag{68}$$

The structure factor derived in section 3.2 can be used for $S(q_{\parallel})$. Several examples can be found in the literature, including the PY hard sphere structure factor,[283,284] 1D paracrystal factor,[274] 2D paracrystal with rectangular or hexagonal symmetry,[41,285] or a 2D lattice factor approach.[166,286] Additional theory can be found elsewhere.[3,41]

GISAXS has been very useful for studies of surface particle growth, where both size and size distribution determination are crucial.[258,267,270,272,283,287−293] This may include in situ studies of particle growth during UHV deposition,[258,267] temperature ramping,[11,272] at the liquid−air interface,[240,285,294] at the liquid−liquid interface,[295,296] at the solid−liquid interface,[288] and under catalytic reaction environments.[259,297,298]

When vapor deposited onto single crystal substrates, particle growth may occur epitaxially.[3,164,258,267,274] In this case, the particles grow with a well-defined orientation determined by the substrate, and they are often faceted. Faceted nanocrystalline particles present Bragg rod scattering normal to their facets. For example, Renaud et al.[258] studied the Volmer−Weber growth of Pd nanoparticles on a MgO substrate and modeled the particles as truncated octahedra with their (100) plane parallel to the substrate. They reported Bragg rod scattering from the (111) and (100) facets at ∼54 and 90° azimuthal angles, respectively. As such, the shape of particles can be monitored by GISAXS.

Other systems have been examined where particle growth is better modeled by a particle that is isotropic in the plane of the substrate, and does not contain facets. Models have been developed based on the difference in aspect ratio in the horizontal and vertical directions,[291] or from the power law scattering in the Porod region.[267] Note that the Porod exponent of oriented particles is not −4. In other cases, particles are assumed to be polydisperse spheres or cylinders, and size distributions along the horizontal and vertical directions are analyzed independently.[259,283,288,293]

Jun and co-workers employed GISAXS to study heterogeneous nucleation and growth of iron oxide[288] and other minerals[287] on a mineral substrate in aqueous solutions. This is one of the unique advantages of using X-rays for characterization. The X-ray can pass through environments in which particles nucleate and grow, allowing for in situ experiments. Using a polydisperse sphere model with a PY structure factor to fit the data, the authors were able to obtain nucleation and growth rates. Further operando examples are found in section 7.2.2.1.

For the examination of colloidal nanoparticles, researchers are often more interested in the structure factor. For example, several groups studied the monolayer to bilayer transition at the air−water interface using a Langmuir−Blodgett (LB) trough,[166,294,299,300] observing structure factor development along the q_z-direction. Others have examined the ordering of spherical particles[301] and nanorods[302,303] at the air−solvent interface by monitoring the evolution of the first order diffraction peak, which occurs due to surface energy minimization. When the particle concentration is high, the particles may also form a multilayer structure by diffusion to the interface, where they stick to each other by van der Waals interactions.[304]

It is also possible to make a monolayer at the solvent−solid interface by immersing a charged substrate in a solution of oppositely charged particles.[305] This type of sample often shows a broad peak in the in-plane structure factor. In situ studies suggest that dip and convective coating methods to make nanoparticle monolayers can produce assemblies of large crystalline domains, but when these layers are transferred to the substrate or dried, the degree of particle ordering often significantly worsens.[166,240,306] Nonetheless, numerous in situ studies have been done during solvent evaporation for spheres,[240,262,264,307−309] cubes,[167] and octahedra.[265,310] Vegso et al. found that spontaneous assembly via solvent evaporation leads to better ordering between layers than when particles are assembled using the layer-by-layer LB technique.[311] When the particles are oriented with respect to each other, the scattering from GISAXS and GIWAXS will be coupled.[167] Using this combination, it was found that the dipole interaction in semiconductor nanoparticles may help to improve the relative particle orientation and therefore the overall degree of order in the superlattice.[309]

6.3.2. Three-Dimensional (3D) Superlattices. In some cases it is possible to simplify DWBA theory (eq 67), for the analysis of 3D structured films. The intensity $I_1(\boldsymbol{q}_t)$ has been calculated using several different approximations. First, when nanoparticles form superlattices with island morphologies, which display rough topologies, the X-ray reflection will significantly weaken and in some cases may be completely removed from the analysis. Even when a film has a smooth surface, if the film is optically thick the X-ray will not penetrate to the film/substrate interface. Again, the reflection will disappear, simplifying the DWBA equation. For these types of samples, the last three terms that involve reflection can be neglected as

$$I_{1\mathrm{DWBA}}(\boldsymbol{q};\, \boldsymbol{q}_t,\, \boldsymbol{q}_r) \approx \frac{|T_i T_f|^2}{N_p} I_1(\boldsymbol{q}_t) \tag{69}$$

Note that, at a grazing angle, the X-ray path length along the sample is $1/\sin(\alpha_i)$ times the film thickness. For example, when a 10 keV X-ray beam propagates through a 50 nm thick Au film with $\alpha_i = 0.3°$, the X-ray would travel about 1 mm along the Au film before reaching the Au/substrate interface. Considering the attenuation length of a 10 keV X-ray beam passing through Au is approximately 5 μm, the X-ray cannot reach the interface and thus no reflection is possible. Second, when particles form highly ordered film structures with nonoverlapping diffraction peaks[152] that are optically thin, one may neglect 12 cross terms resulting from eq 67 and consider only the four self-squaring terms.[149]

Third, the same approximation that can be used for 2D monolayer systems can also be applied when the in-plane and out-of-plane structure can be decoupled. For example, when the superlattice is a stack of layers (the reciprocal space lattice vector c^* is normal to the substrate) and there is no coupled disorder between in-plane and out-of-plane directions, the full DWBA can be approximated as eq 68.

Lee et al. first employed a paracrystal theory to compute the GISAXS intensity of 2D hexagonal cylinders lying parallel to the substrate.[149] Later, Ree's group calculated the scattering of

DOI: 10.1021/acs.chemrev.5b00690
Chem. Rev. XXXX, XXX, XXX−XXX

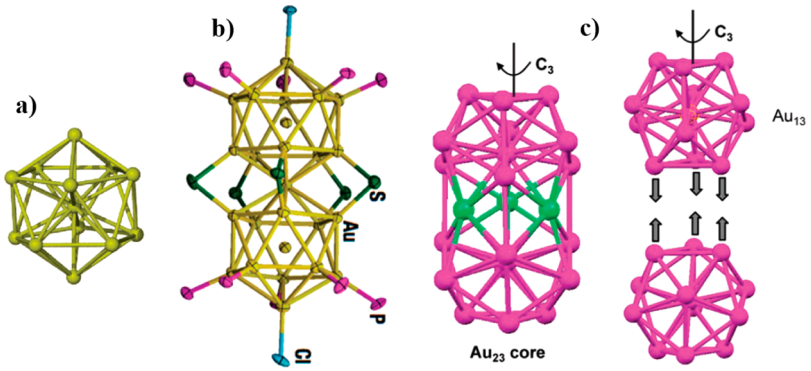

Figure 35. (a) Icosahedral Au13 atomic cluster. Reprinted from ref 321. Copyright 2008 American Chemical Society. (b) Au25 atomic cluster composed of two fused Au13 clusters sharing a vertex. Reprinted from ref 328. Copyright 2007 American Chemical Society. (c) Core of an Au38 atomic cluster consisting of two Au13 clusters sharing a face. Reprinted from ref 322. Copyright 2010 American Chemical Society.

both hexagonally perforated layer[170] and gyroid[169] film morphologies using the DWBA. They assumed a homogeneous wave field in the film, meaning that wave amplitudes T and R are the same for N_p particles. This assumption is used for all the rest of the examples. In their work, they assumed the second approximation (vide supra). Stein et al. calculated GISAXS from block copolymer films of hcp, fco (face-centered-orthorhombic), and bcc packed spheres[260] using the third approximation. The in-plane structure factor was computed with an appropriate choice of peak function, such as a Lorentzian. The peaks in the z-direction were much broader, appearing as a vertical streak due to the small number of layers, and were calculated with the full DWBA equation. Smilgies et al. further extended Stein's approach to compute the scatterings from samples that contained multiple numbers of layers, where each layer consisted of 2D hexagonally packed spherical particles.[166] To study the structural transition from a LB monolayer of spherical silver particles to a bilayer, Vegso et al. developed a model using paracrystal theory, where c^* is also parallel to the z-axis.[285] In this model, they assumed that the paracrystal disorders along the in-plane and out-of-plane directions are independent of each other, resulting in a similar GISAXS simulation as Smilgies. Buljan et al. developed a more sophisticated paracrystal model[165] using the first approximation. In their model, they employed both the first and second kinds of defects and correlated paracrystal disorders. They successfully characterized nanocrystal assemblies with orderings that were induced along a particular direction by light ion irradiation.

Using the first approximation, Förster used powder diffraction theory to study nanoparticle assemblies composed of a single type of particle.[49] More recently Breiby, Gibaud, and co-workers utilized the powder diffraction theory by considering the two-beam effect (that is, direct and reflected).[312] By carefully analyzing the shape of the diffraction peaks, they found that the nanopores in the unit cell were deformed to an ellipsoid. Thus far, these examples have only considered assemblies of a single type of particle. Lee and co-workers simulated GISAXS scattering patterns using the pseudolattice factor approach introduced in section 3.3.4 and the full DWBA eq 67.[39,313] They modeled superlattices composed of a single type and also binary mixtures of DNA-conjugated gold and silver particles that could be assembled into structures that are compositionally random bcc-like, or CsCl.

GISAXS can be simulated using brute force when the coordinates of the particles are known, for example using the Monte Carlo method.[314] This approach is particularly useful when nanoparticles are assembled as a homogeneous film that requires full consideration of the reflection of the X-ray at the interface between the film and substrate.[168]

7. APPLICATIONS

In recent years, the development of high brilliance synchrotron X-ray sources and better detectors has driven the adoption of SAXS as a tool for scientific discovery in fields that make use of materials characterization at nanometer length scales.[24] In this respect, SAXS is a complementary technique to electron microscopy. While real space imaging may be more intuitive to interpret, it is limited in terms of analysis area and the types of sample environments that can be examined, and it is not suitable for bulk measurements. In contrast, X-ray techniques provide statistically meaningful structural information averaged over macroscopic sample volumes. Perhaps most important, SAXS is capable of providing structural characterization in realistic or native sample environments. Further, the high flux and tunable energy of modern synchrotrons have decreased exposure time requirements. When combined, SAXS becomes ideally suited for in situ or operando experiments. In the following, we will focus on three fields related to metal and metal oxide nanoparticle research that make use of these advantages for structural characterization with SAXS including nanoparticle synthesis (section 7.1), self-assembly (section 7.2), and catalysis and energy storage (section 7.3).

7.1. Colloidal Nanoparticle Synthesis

During the last half-century, researchers have put forth tremendous effort, as well made great progress, in synthesizing monodisperse nanoparticles with diverse shapes.[106,315−319] Characterization is a key driver of this work, where it is critical to understand the structure of the particle products with high accuracy to further advance synthetic methodology, as well probe structure−function relationships. X-ray scattering has been at the forefront of this work, enabling nanoparticle structural characterization with atomic resolution, in native environments and operando conditions.

The most commonly used X-ray scattering technique is atomic diffraction, which has impacted nanoparticle synthesis by providing structural information at the atomic scale. For example, X-ray crystallography revealed the atomic structure of molecularly defined Au clusters[192] including Au25,[320,321] Au38,[322] and Au102.[194] Numerous other atomic Au cluster crystal structures have been solved.[323−325] These atomic

DOI: 10.1021/acs.chemrev.5b00690
Chem. Rev. XXXX, XXX, XXX−XXX

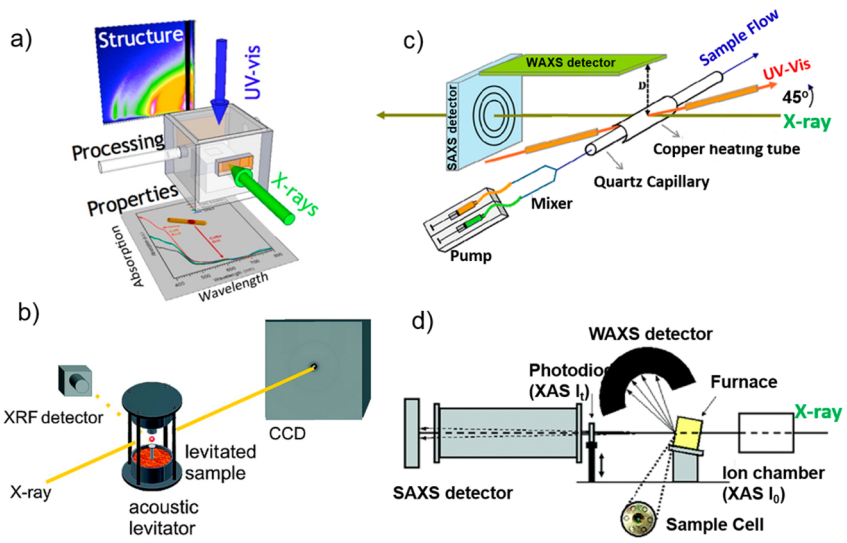

Figure 36. Schematic representations of several experimental setups for in situ nanoparticle growth studies. (a) Structural characterization of colloidal nanorod assemblies using GISAXS and UV−vis. Adapted from ref 303. Copyright 2015 American Chemical Society. (b) Experimental setup for SAXS and X-ray absorption near-edge spectroscopy (XANES) analysis of gold nanorods synthesized in droplets. Modified from ref 360. Copyright 2010 American Chemical Society. (c) Real-time SAXS/WAXS/UV−vis measurements during the formation of Au nanoparticles. Modified from ref 363. Copyright 2015 American Chemical Society. (d) SAXS/WAXS/XAS multitechnique setup for the study of inorganic solid crystallization. Adapted from ref 361. Copyright 2006 American Chemical Society.

clusters may provide a baseline to understand in situ nanoparticle synthesis. Au13[326] has been observed to be a core or basic motif for many of these atomic clusters (Figure 35a). It has an icosahedral symmetry and is a stable form of a small nanoparticle.[327] There are larger clusters consisting of multiple of Au13 motifs fused vertex-to-vertex[328] (Figure 35b) or face-to-face[322] (Figure 35c). Further, the structure of the cluster may transform depending on the surrounding environment.[329]

WAXS, also called XRD, has also played a significant role in characterizing less-defined nanoparticles. For example, WAXS has been used to determine lattice constants of nanoparticles. Researchers found that the lattice constants of some particles decrease with particle size as a result of surface stress.[67,106,330] On the other hand, nanoparticles have also shown increases in lattice constants for decreasing particle size, which are believed to originate from the incorporation of other elements,[127,331] through structural change,[332] alloying,[125] lattice stain due to particle shape,[330] or the formation of heterostructured nanoparticles.[106]

There are other types of analysis, varying from simple indexing to full atomistic calculations using the Debye formulas.[67,106,330] Further, the degree of atomic order has been studied with PDF techniques.[127,331] Neder et al. found unusually high stacking fault density in II−VI semiconductor nanoparticles using PDF analysis.[333] Further use cases of diffraction for structural analysis can be found in a recent review.[24]

In addition to WAXS, SAXS has been used to understand nanoparticle synthesis, and is frequently employed for in situ nucleation and growth studies. SAXS measures an appropriate q range to determine the size and shape of nanoparticles, and also provides several orders of magnitude higher intensity as compared to the WAXS region (see Figure 29). We note that it is not our intent to review nanoparticle synthesis as a whole. For this reason, in sections 7.1.1−7.1.4 we review in situ nanoparticle synthetic work that makes use of X-ray scattering, in particular SAXS, and its combination with other techniques such as WAXS or X-ray absorption spectroscopy (XAS). We refer readers who may be interested in the nanoparticle growth mechanisms to recent reviews by Thanh et al.[334] and Wang et al.[335]

7.1.1. SAXS Analysis Tools. Here we briefly summarize the type of information that can be obtained from an SAXS experiment. In section 3.2.3.3, we discussed how the dimensionality of a particle (i.e., shape) can be determined from the power law slope in the high q region of SAXS.[94,336] In some cases, dimensionality can also be determined from the WAXS diffraction peak.[337,338] In section 3.2.1.2, we showed that, for isometric polyhedral particles such as Platonic or Archimedean solids, the form factor oscillation is sensitive to the face/face distance.[64] In addition, SAXS is sensitive to the particle surface area.[93] The relative surface area per unit volume may increase as the surface roughness of the particle increases[202] or as spherical particles become polyhedral.[64]

The size distribution function is another key piece of information obtained from SAXS (see section 3.2.2). When the shape of a particle is known or can be assumed, it is possible to fit the data to determine the size distribution[64] and several software packages make this type of analysis.[33,34,339] For uniform sized particles, SAXS can allow the researcher to perform more advanced structural characterization, capable of determining core−shell morphologies[120] or the edge length of polyhedral particles[159] by employing model fitting (section 3.2.4.3). This kind of structure analysis with SAXS has been popular in colloidal particle research.[35]

In addition, by using absolute intensity analysis, it is possible to obtain the particle volume fraction, or nanoparticle concentration. In section 3.2.3.1 we discussed the use of $I(0)$ to determine the particle concentration. The invariant may also be used to determine the concentration; see section 3.2.3.5.

7.1.2. Experimental Techniques for In Situ Measurements. With the advent of modern high flux synchrotron X-ray sources, in situ or operando studies using X-rays have

DOI: 10.1021/acs.chemrev.5b00690
Chem. Rev. XXXX, XXX, XXX−XXX

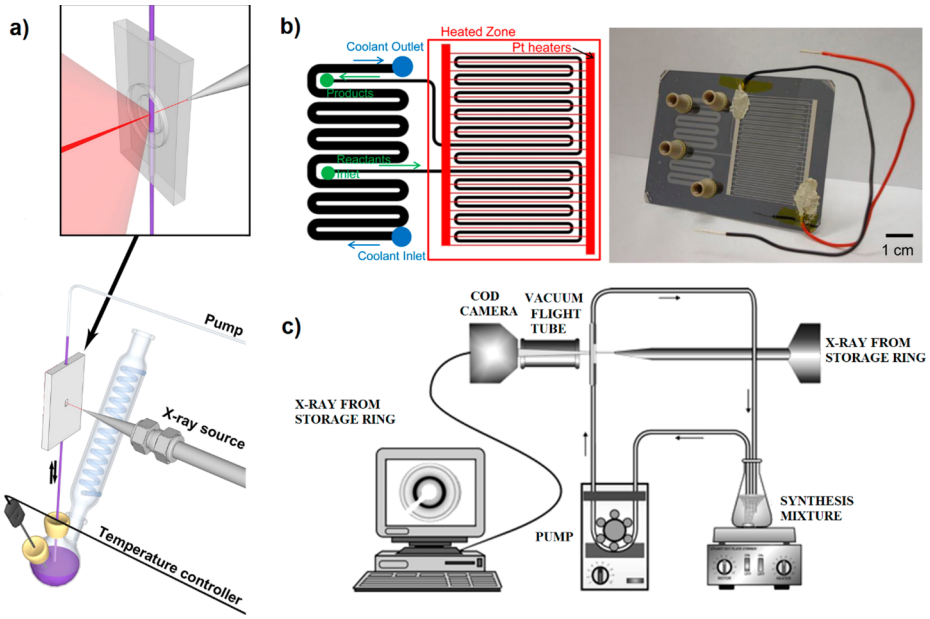

Figure 37. (a) Experimental setup of a sampling method for in situ SAXS/WAXS. Modified with permission from ref 106. Copyright 2015 Nature Publishing Group. (b) Microfluidic reactor for millisecond time-resolved SAXS and XAS studies of nanoparticles synthesis. Reprinted from ref 318. Copyright 2015 American Chemical Society. (c) Experimental setup for in situ SAXS/WAXS measurements. Reprinted from ref 365. Copyright 2005 American Chemical Society.

flourished. These sources can provide time resolutions on the order of picoseconds,[340−344] microseconds,[345,346] milliseconds,[347,348] or more than minutes.[105,106,318,349−353] Sample environments may include high pressure,[344] high temperature,[354,355] hydrothermal,[356−358] or operando conditions.[5,6] Various multimodal measurements provide complementary information about a system, and may include techniques such as SAXS/UV−vis,[359] SAXS/XAS,[360] SAXS/WAXS/XAS,[361] SAXS/WAXS/Raman,[362] or GISAXS/GIXAS/mass spectrometry,[259] as shown in Figure 36, where GI and XAS stand for grazing incidence and X-ray absorption spectroscopy, respectively.

There are several things one must take into account when planning an X-ray experiment. First, it is crucial to understand that X-rays may cause unexpected reactions, including photochemical reduction,[364] hydrolysis,[182] or thermal/photoelectrical destruction.[72] These beam effects are typically lumped together and described as "beam damage". For studies involving in situ nanoparticle synthesis, the photochemical reduction of precursors can lead to fouling of the X-ray windows of a capillary or reaction cell, necessitating the use of appropriate control experiments. XAS requires longer X-ray exposure compared to SAXS, and accordingly is more susceptible to beam damage. It is also important to consider the effects of a particular sample environment or reaction vessel on the reaction itself.[106] For example, when examining the in situ synthesis of nanoparticles in a capillary designed specifically for X-ray experiments, there may be variations in monomer diffusion as compared to the same reaction performed in a standard three-neck flask with constant stirring. Further, the sample in the beam must be representative of the contents within a reaction vessel, including both particle size and concentration. In addition, the measured sample volume should be kept constant; otherwise the number of particles in the beam will fluctuate preventing quantitative analysis.

To mitigate these issues, various in situ reaction setups have been developed, as shown in Figure 37. To monitor the reduction of gold ions on seed nanocrystals, Kwon et al. used a sampling method, as shown in Figure 37a.[106] For simultaneous SAXS and WAXS measurements, the authors periodically took an aliquot of solution from a reaction flask that was located near the X-ray beam using a syringe pump. Microfluidic devices have also shown promise. Karim et al. studied Pd nanoparticle growth using the setup shown in Figure 37b.[318] Stehle et al.[487] also developed a SAXS microfluidic device for multiphase, oil-in-water experiments. Amstad et al. performed SAXS experiments during the synthesis of amorphous nanoparticles by supersonic spray-drying using a microfluidic nebulator.[366] Microfluidic devices have often been combined with a microfocused X-ray beam.[367]

Continuous sampling as in Figure 37c[365] using a peristaltic pump can provide more flexibility for various multimodal measurements including SAXS/WAXS/Raman/IR/UV−vis.[362] Polte et al. continuously extracted sample from a reaction flask which was ejected through a nozzle to create a free liquid jet, which could be probed with SAXS and XAS.[351] This type of windowless measurement is ideal because it can prevent window contamination. Polte et al. also used an acoustic levitator to position a droplet of a reaction solution in the X-ray beam for SAXS and XAS measurements (Figure 36b).[360] Micromixer freejet setups can also be used to study the very early stage of particle growth (sub 1 ms), as demonstrated by Marmiroli et al.[368] and Schiener et al.[317] The X-ray beam was used to measure the scatterings of the particles synthesized within droplets that were jet ejected from the mixer. By varying the distance between the mixer and X-ray beam position, various time scales can be studied. In other examples, researchers connected the output of a mixer to capillaries that could be pressurized to maintain water in its supercritical state (similar to the setup in Figure 36c).[345] For experiments on

DOI: 10.1021/acs.chemrev.5b00690
Chem. Rev. XXXX, XXX, XXX−XXX

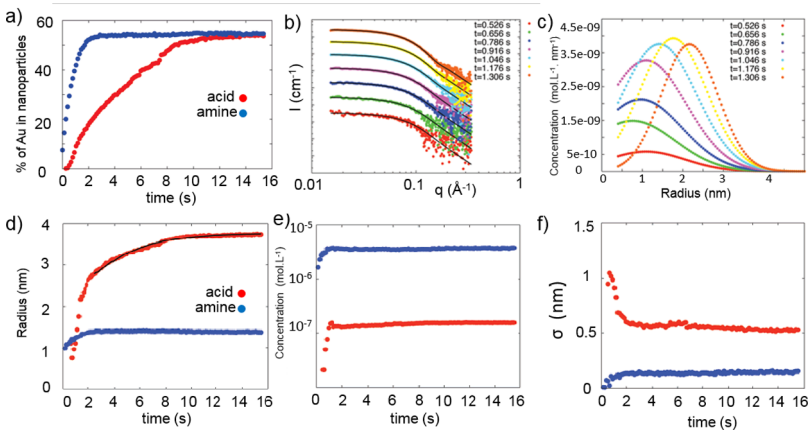

Figure 38. (a) Yield of nanoparticle reduction reactions as a function of time for acid and amine ligands. (b) Early stage SAXS patterns of the reaction with acid ligand and the corresponding fits. The data are scaled for clarity. (c) Size distribution corresponding to the SAXS patterns in (b). (d)−(f) Radius, concentration, and polydipsersity as a function of time from SAXS fitting for the two different ligands. Modified from ref 352. Copyright 2007 American Chemical Society.

slower time scales (0.1 s to tens of seconds), a stopped-flow device has been used.[348,352,369,370]

There have also been significant experimental advances by making use of high energy X-rays. Peng et al. studied the growth mechanism of silver nanocubes by employing a high energy X-ray beam (70 keV) that was able to penetrate through a specially designed reaction vessel with a long (5 mm) path length.[371] Bremholm et al.[90] also utilized the high penetration power of high energy X-rays. They reported a simultaneous in situ SAXS/WAXS study of the formation and growth of pure phase magnetite nanoparticles in supercritical H_2O (P_c = 221 bar and T_c = 374 °C). Precursors were injected into a stainless steel capillary reactor,[354] through which high energy X-rays (80 keV) can penetrate.

7.1.3. Early Stage: Nucleation and Growth of Nanoparticles. During nanoparticle synthesis studies, there are various reaction specific parameters that are important. Depending on the processes of interest, i.e. nucleation, growth, or Ostwald ripening, various time scales (microseconds to hours) may be required. Further, there are certain parameters that must be extracted from the experimental data. For example, the number, mean size and distribution width, and volume fraction of particles can be obtained by fitting SAXS curves or calculating the invariant. In this section, we review a number of examples showing how the information from SAXS experiments can be used to understand reaction mechanisms.

Abécassis et al.[352] used a stopped-flow device[348] to monitor the very early stage growth of gold nanoparticles with a time resolution of 3 ms for UV−vis, 130 ms for SAXS, and 800 ms for WAXS. SAXS data were scaled into an absolute scale, and the calculated invariant allowed the researchers to determine the degree of precursor reduction (Figure 38a). By fitting SAXS data shown in Figure 38b with a polydisperse sphere model, they obtained the size distribution function (Figure 38c), mean radii (Figure 38d), number concentrations (Figure 38e), and widths of the size distribution (Figure 38f) of the gold nanoparticles throughout the in situ experiment.

The same team later studied the difference between using acid ligand and using amine ligand on gold nanoparticle synthesis in toluene using $NaBH_4$ as a reducing agent.[370] They observed, at the final stage, approximately 55% of gold precursors are reduced to nanoparticles. Burst nucleation within 2 s was found for both ligand cases (Figure 38e), but the growth behaviors were different. When using the amine ligand, no further growth occurred after nucleation, as was evident from the constant invariant and particle concentration. On the other hand, when the acid ligand was used, the particles continued to grow after nucleation ceased.

Abécassis et al. further studied gold nanoparticle formation with simultaneous SAXS and XAS (Figure 39).[370] Using these

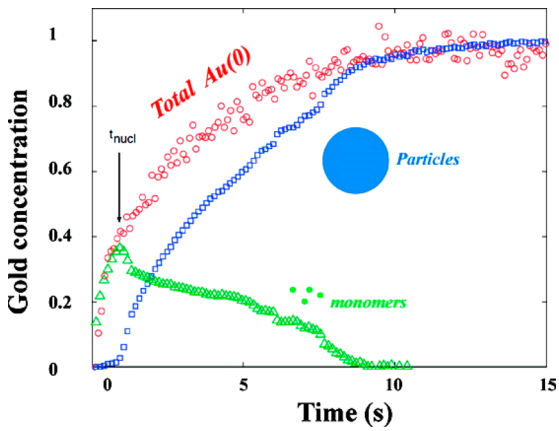

Figure 39. Formation rate of monomers for the acid ligand case at T = 298 K (circles) from XANES. Yield of reaction (squares) from SAXS; free gold atoms Au(0) (triangles) obtained by the difference between the formation rate of monomers and the yield of reaction. Adapted from ref 370. Copyright 2010 American Chemical Society.

combined techniques, the authors claimed to observe Au(0) existing as free atoms or very small atomic clusters without attaching to prenucleated particles. Monomeric atoms were also found in a Pt system by others.[372] The concentration of monomeric atoms increased to show a peak at the burst of particle nucleation, which was consistent with the mechanism that LaMer proposed, that is, classical burst nucleation and growth by monomer addition.[373,374] However, the data did not preclude other growth mechanisms such as autocatalytic growth[375] or an aggregative growth mode including coalescence.[347,350,372,376−378]

According to LaMer's theory, once the nuclei form, they will grow by adsorbing additional monomer, or individual reduced atoms.[373] Thus, the total number of nuclei will not decrease

DOI: 10.1021/acs.chemrev.5b00690
Chem. Rev. XXXX, XXX, XXX−XXX

during the reaction. However, there are many reports that show the opposite phenomenon. For example Polte et al.[360] examined in situ gold nanoparticle synthesis using the Turkevich procedure, which uses trisodium citrate as a stabilizer and a mild reducing agent. Initially, they observed burst nucleation, in which nuclei of approximately 2 nm were formed. The particles grew by coalescence as evidenced by a significant decrease in the particle number with an increase in particle size. Soon after, the particle growth slowed without a decrease of particle number. This behavior may suggest the so-called "size focusing effect" or "growth by diffusion," first described by Reiss et al.[379]

Takesue et al. focused their attention on the nucleation.[346] They employed a continuous flow reactor setup to monitor Ag nanoparticle growth with trisodium citrate with a time resolution of 0.18 ms. They also observed a burst nucleation, which resulted in 0.58 nm diameter nuclei at 0.59 ms, which they assigned to icosahedral Ag13 atomic clusters. The nuclei size remained the same until 0.98 ms, when they quickly aggregated to form particles 3.36 nm in size. Afterward, growth by coalescence was observed, similar to Polte.[360] The aggregation of icosahedral atomic clusters has also been observed in other work, including early studies by Uyeda et al.[380] and Turkevich et al.[381] The existence of Au25 and A38 structures composed of Au13 moieties introduced in the previous section may also support this growth mode.

These results indicate that stable icosahedral atomic clusters are formed via burst nucleation, which subsequently grow by the aggregative growth mechanism proposed by Zukosi et al.[382] and recently reviewed by Wang et al.[335]

7.1.4. Later Stage: Ostwald Ripening vs Smoluchowski Aggregation. There are two later stage growth mechanisms that have been proposed for nanoparticle growth. The first is Ostwald ripening[334] in which larger particles grow at the expense of smaller particles, while the second is Smoluchowski aggregation,[334,381,383] where two particles collide and aggregate into a larger particle. Initially, researchers tried to distinguish between these two mechanisms by examining the relationship between the mean radius $\bar{R}$ at time t. According to Ostwald ripening,[334] $\bar{R} \propto t^{1/3}$, while for Smoluchowski aggregation,[384] $\bar{R} \propto t^{\beta}$, where β is dependent on the aggregation mechanism.[383] Pontoni et al. found that silica particles aggregated with the power law exponent β between 1/2 and 1/3.[384] This power law scaling was attributed to a diffusion limited growth mechanism, indicating there was an attraction between the particles.

However, in some cases the exponent $\beta = 1/3$ for Smoluchowski aggregation, and thus the time dependent size scaling would be insufficient to distinguish between the two growth mechanisms. Instead it would be necessary to examine the size distribution function. Kellermann et al.[385] used a distribution function derived from the classical Liftshitz–Slyozov–Wagner (LSW) theory to fit SAXS curves from the in situ growth of Ag nanoparticles in sodium borate glass. The LSW theory is based the Ostwald ripening growth mechanism.[385] They found that $\bar{R} \propto t^{1/3}$, as predicted by LSW theory. As shown in Figure 40a, however, the particle size distribution expected from LSW theory did not fit the data better than an empirical log-normal function, leading the authors to question whether Ostwald ripening was occurring. Meli and Green presented similar results for a system of gold nanoparticles in a polymer composite.[386]

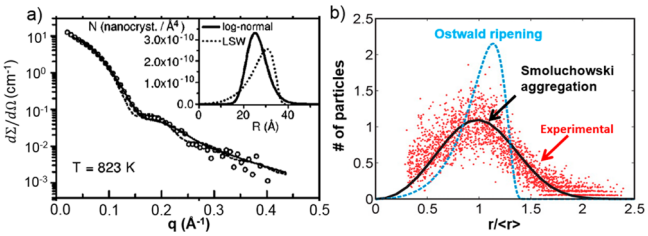

Figure 40. (a) SAXS data of Ag nanoparticles in sodium borate glass and fits using LSW and log-normal size distribution functions. Adapted with permission from ref 385. Copyright 2004 American Physical Society. (b) The particle size distribution obtained from in situ liquid TEM experiments of Ag nanoparticles reduced by the electron beam is consistent with Smoluchowski aggregation. Adapted from ref 387. Copyright 2014 American Chemical Society.

Woehl et al. studied Ag nanoparticles grown in solution using TEM.[387] As above, the mean growth rate was consistent with the LSW model, but the size distribution was broader and more symmetric than predicted. The authors found that all particles grew simultaneously, indicating that Ostwald ripening is not the dominant growth mechanism. They showed the particle size distribution matches well with the Smoluchowski aggregation kinetics at an ensemble level as shown in Figure 40b.

7.2. Nanoparticle Assembly

There has been considerable interest in recent years in the assembly of nanomaterials. Indeed, a grand challenge in nanotechnology is the rational design and assembly of nanoparticle building blocks into hierarchical crystalline superstructures, or superlattices, with exquisite control over superlattice symmetry and lattice parameters, in addition to superlattice size and shape. Analogously, these particle building blocks can be thought of as "atom mimics", with interactions governed by supramolecular forces, as opposed to the electronic overlap that determines the chemical bonding of their atomic counterparts.

These superlattices are of fundamental interest as analogues of atomic crystallization. While spherical particles typically have isotropic interaction potentials, anisotropic and patchy particle building blocks[159,388−391] may be used to develop concepts of directional bonding. Further, these assemblies have been shown to exhibit novel and useful properties.[392−394]

In this section, we limit our interest only to crystalline assemblies, and the use of X-ray scattering to study these superlattices. The detailed structural models obtained from SAXS provide researchers a means to analyze the physics of assembly. Take for example, studies on the role of alkyl ligands in the nanoparticle assemblies that are discussed below. In these studies, it is critical to obtain statistically accurate interparticle distances using the exact conditions in which the assembly forms. This information allows one to draw conclusions about the conformation of the ligands and thus the pair potential that is affected by the ligands.

Analysis of SAXS data from nanoparticle assemblies varies from simple indexing (section 3.3.5), and/or peak shape analysis (section 3.3.6), to full SAXS profile simulation (section 3.3.4), depending on the type of information one would like to obtain. When the symmetry of the crystalline lattice is not obvious, it may be useful to calculate the PDF from the experimental structure factor (section 3.3.1). In section 7.2.1, we review several examples of SAXS analysis related to nanoparticle superlattices, explaining how the information was

DOI: 10.1021/acs.chemrev.5b00690
Chem. Rev. XXXX, XXX, XXX−XXX

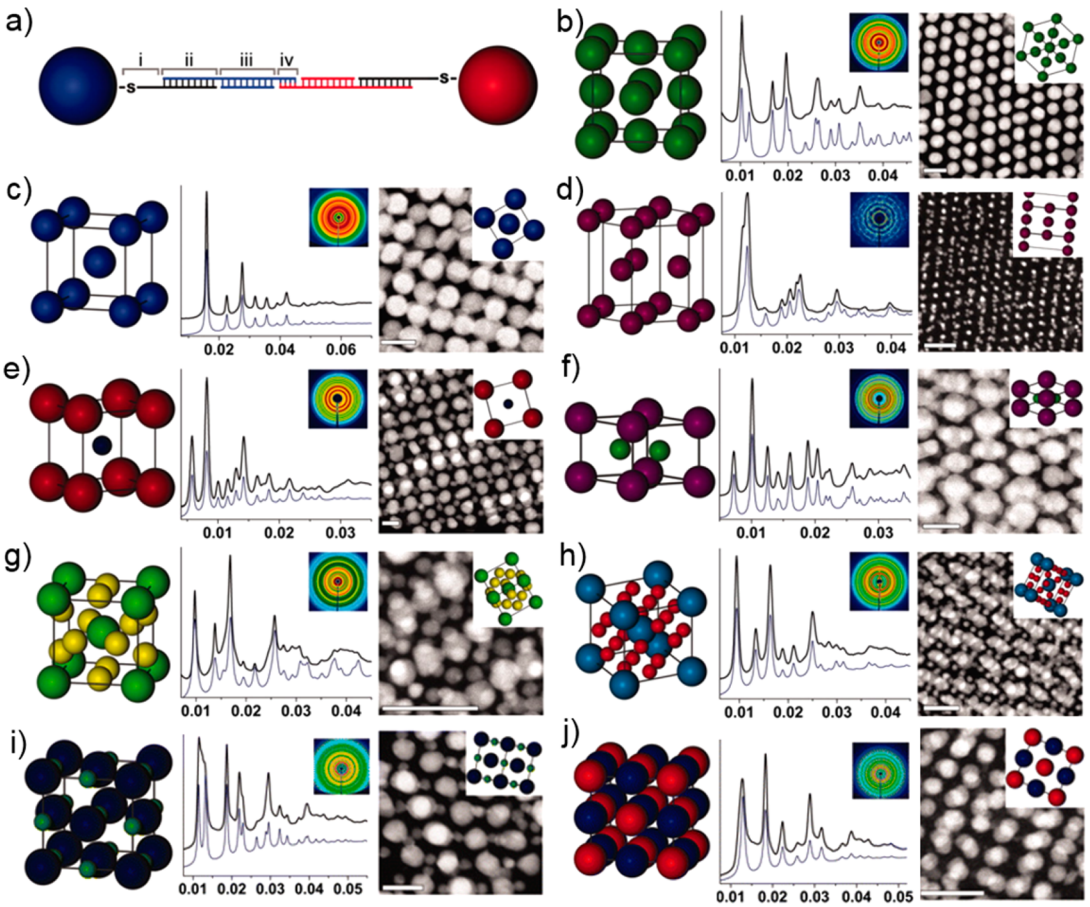

Figure 41. (a) Nanoparticle superlattice engineering with DNA. The strands used to assemble these nanoparticle superlattices consist of (i) an alkylthiol moiety and 10-base nonbinding region, (ii) a recognition sequence that binds to a DNA linker, (iii) a spacer sequence of programmable length to control interparticle distances, and (iv) a "sticky end" sequence that drives nanoparticle assembly via DNA hybridization interactions. (b−j) The superlattices are isostructural with (b) fcc, (c) bcc, (d) hcp, (e) CsCl, (f) AlB_2, (g) Cr_3Si, and (h) Cs_6C_{60} lattices, (i) NaCl, and (j) simple cubic. From left to right, each panel contains a model unit cell (not to scale), 1D and 2D (inset) SAXS patterns, and a TEM image of resin-embedded superlattices, along with the unit cell viewed along the appropriate projection axis (inset). Lines in the model denote edges of the unit cell; individual DNA connections are omitted for clarity. SAXS data are plots of nanoparticle superlattice structure factor $S(q)$ (y-axis, arbitrary units) versus scattering vector q (x-axis, $Å^{-1}$). Black traces are experimental data; gray traces are modeled SAXS patterns. All scale bars in the TEM images are 50 nm. Modified with permission from ref 12. Copyright 2011 American Association for the Advancement of Science.

extracted from SAXS data and its use in understanding superlattice assembly. Again, our purpose is not to review all of the nanoparticle assembly behavior, but instead to highlight the use of SAXS in the assembly literature.

7.2.1. Assemblies Controlled by Soft Materials. There are several types of assemblies that utilize the chemical or physical properties of organic molecules. Those molecules can provide attractive interactions, repulsive interactions, or both, which can be used by the nanoscientist to engineer nanoparticle assemblies. This section reviews several types of assemblies, where X-ray scattering has played a significant role in understanding their physics.

7.2.1.1. DNA Assembly. DNA is unique as a ligand to tailor the interaction between nanoparticles.[395] It can be synthesized with any permutation of bases, up to several hundred in length. When conjugated to a nanoparticle, this results in a dense shell of DNA with pendent "sticky ends" that impart highly specific and programmable interactions between the particles (denoted DNA−NPs).[396,397] While DNA superlattices maintain some degree of structural integrity when dried or frozen, the ordering is significantly reduced,[129] and thus it is necessary to study the assembly process in aqueous buffered solution using SAXS to eliminate variations in DNA conformation.[129] In fact, all reported structures thus far have been solved by SAXS.

These types of samples are typically randomly oriented, and thus the analysis is often equivalent to powder diffraction. Superlattice structural determination for single component spherical particle systems can be determined by simple indexing. Binary and ternary systems require full intensity simulation to confirm the particle positions in the unit cell (see section 3.3.4). Superlattices composed of polyhedral particles require even more careful modeling due to difficulties decoupling form and structure factor.[64,161,162,389] The full profile analysis is therefore crucial to solve the structure, enabling one to determine the relative orientation of each nanoparticle in the unit cell.[39,159,161,162,389] These types of analyses have resulted in a growing body of literature to understand the assembly of nanoparticles using DNA linkers, which is briefly reviewed below.

Initial work by Park et al. to characterize DNA-linked nanoparticles with SAXS showed that they formed amorphous aggregates with ill-defined symmetry.[398] However, the average interparticle distance could be controlled by varying the DNA length. In 2008, Park et al.[57] and Nykypanchuk et al.[58]

DOI: 10.1021/acs.chemrev.5b00690
Chem. Rev. XXXX, XXX, XXX−XXX

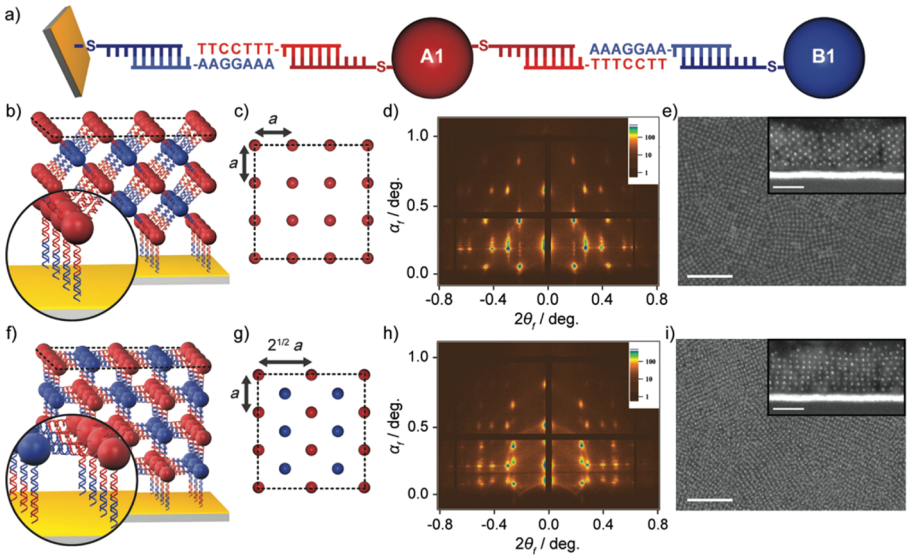

Figure 42. Superlattice orientation can be controlled by the type of DNA bonding interactions between the superlattice and substrate. (a) A binary DNA sequence design enables the stepwise growth of DNA−AuNP superlattices with either (100) (b−e) or (110) orientation (f−i). Schematic illustrations of (100)- and (110)-oriented bcc superlattices grown on mono- or bifunctionalized substrates, respectively, are shown in (b) and (f). The (100) orientation formed on substrates that displayed a single type of linker (blue) while the (110) orientation formed on substrates that displayed both types of linkers (blue and red), matching the complementary DNA-functionalized nanoparticles in the (100) (c) and (110) planes (g). (d, e) Two-dimensional GISAXS scattering pattern and SEM of (100)-oriented bcc superlattices. (h, i) Two-dimensional GISAXS scattering pattern and SEM of (110)-oriented bcc superlattices. Scale bars for the SEM top-down and cross-section views are 200 and 100 nm, respectively (e, i). Reprinted with permission from ref 168. Copyright 2013 Wiley-VCH Verlag GmbH & Co. KGaA.

independently showed that nanoparticles could be assembled into crystalline lattices using DNA linkers, as characterized by SAXS. The key innovation was the use of a short "sticky end" linker, which would bind the particles together but had a relatively low dissociation temperature. This concept is called the "weak polyvalent effect." When annealed, the DNA−NPs undergo multiple dehybridization and rehybridization events eventually forming a crystalline nanoparticle assembly. Through multiple studies, it has been observed that the system adopts a crystallographic symmetry that maximizes the number of duplexed DNA interconnects linking the particles.[12,61,399] This principle can be illustrated through a simple example. A system of particles with a single type of DNA linker (homocomplementary), in which each DNA−NP construct can bind to itself and all other particles, will form close-packed fcc and hcp structures.[57] Alternatively, a binary set of particles that have heterocomplementary linkers (in other words, particle A can only bind to particle B, and vice versa) will form a bcc structure.[57,58] Because the DNA sequence affects the crystal structure, it will also have an effect on the surface energy of various facets. This concept has been used to generate single crystals, whose habit could be described by Wulff construction.[400]

Variation in particle size, shape, and DNA sequence have resulted in diverse crystallographic structures.[399] For binary systems of spherical particles, simultaneous variation of the particle size and DNA length allows one to access symmetries that are isostructural with fcc, hcp, bcc, CsCl, AlB_2, Cr_3Si, and Cs_6C_{60} (Figure 41).[12] Ternary systems may also be prepared.[160] Further, polyhedral nanoparticles may be used as the building blocks, where the shape of nanoparticle dictates the final structure. In this case, DNA hybridization will be maximized when the facets of two adjacent particles lie face-to-face.[159,161,389]

For all of these structures, the composition of the core may be decoupled from the assembly process. Thus, superlattices can be made from Au, Ag, Pt, Pd, quantum dots, Fe_2O_3, FeO, or in principle any kind of particle that can be functionalized with DNA, including viruses and hollow particles.[401−404]

SAXS has proven to be useful for monitoring structural transformation. For example, May et al.[405] and Kim et al.[406] used an appropriate hairpin DNA to dynamically control the lattice parameter. Macfarlane et al. synthesized ternary superlattices where the third particle could be incorporated within and removed from parent binary superlattices leading to topotatic interconversions.[160] Later, Gang and co-workers showed that, by adding an appropriate DNA sequence to an existing superlattice, they could modify interparticle interactions resulting in a bcc to fcc structural transition.[407]

Thin film superlattices may also be grown on DNA modified substrates. We recently reported the growth of a bcc DNA−NP superlattice using a binary system, where each layer was grown in a stepwise or layer-by-layer fashion (Figure 42).[168] The films were characterized by GISAXS, which showed 2D powder diffraction spots. This indicated that superlattice domains were randomly oriented in the plane of the substrate but were textured normal to the substrate. This type of analysis would be challenging with transmission mode measurements; because of the alignment of the superlattice with the direction of the beam, several peaks would not be in a Bragg condition and thus forbidden. Significantly, the superlattice orientation was affected by the type of DNA on the substrate, allowing for a (100) or (110) texture. This result could be explained by maximizing the number of DNA interconnects at the interface between the substrate and superlattice. The superlattices could be reversibly dried and reconstituted.[129] The orientation could also be controlled by lithographically patterning the substrate using e-beam lithography, and using that substrate as a template for subsequent superlattice growth.[408]

DOI: 10.1021/acs.chemrev.5b00690
Chem. Rev. XXXX, XXX, XXX−XXX

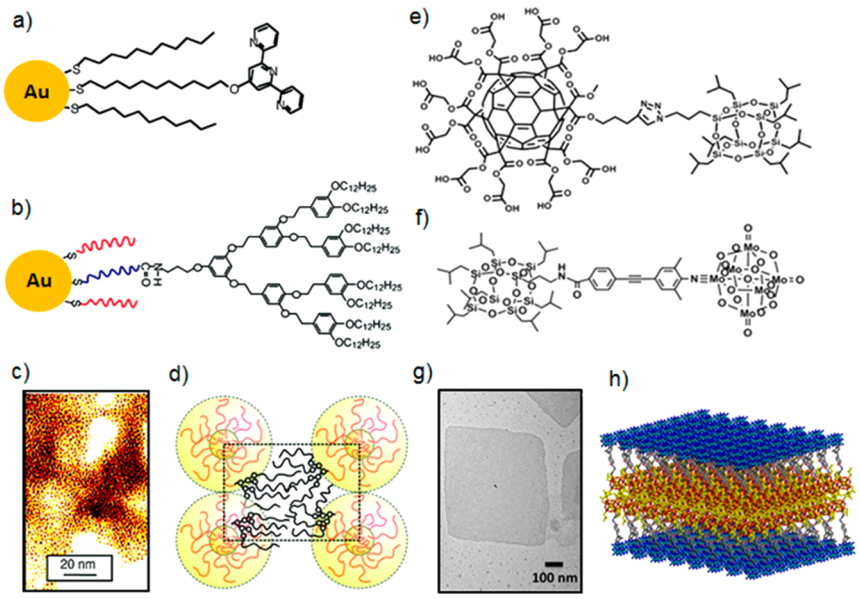

Figure 43. (a, b) Chemical structures of AuNPs attached with different ligands including (a) pyridine and (b) dendrimers. (c) TEM image of the aggregates from the assembly of AuNPs shown in (a). (d) Schematic of the simple cubic phase of superlattice assembled from AuNPs shown in (b). (e, f) Chemical structures of molecular Janus particles (e) POSS-C_{60} and (f) POSS-POM. (g) Bright field TEM image of 2D nanocrystals from slow evaporation of POSS-C_{60} solution in (e). (h) Simulated molecular arrangements in the 2D plane lattice of the POSS-POM nanocrystals in (f). (a, c) Modified from ref 409. Copyright 2002 American Chemical Society. (b, d) Modified from ref 417. Copyright 2012 American Chemical Society. (e–h) Modified from ref 390. Copyright 2014 American Chemical Society.

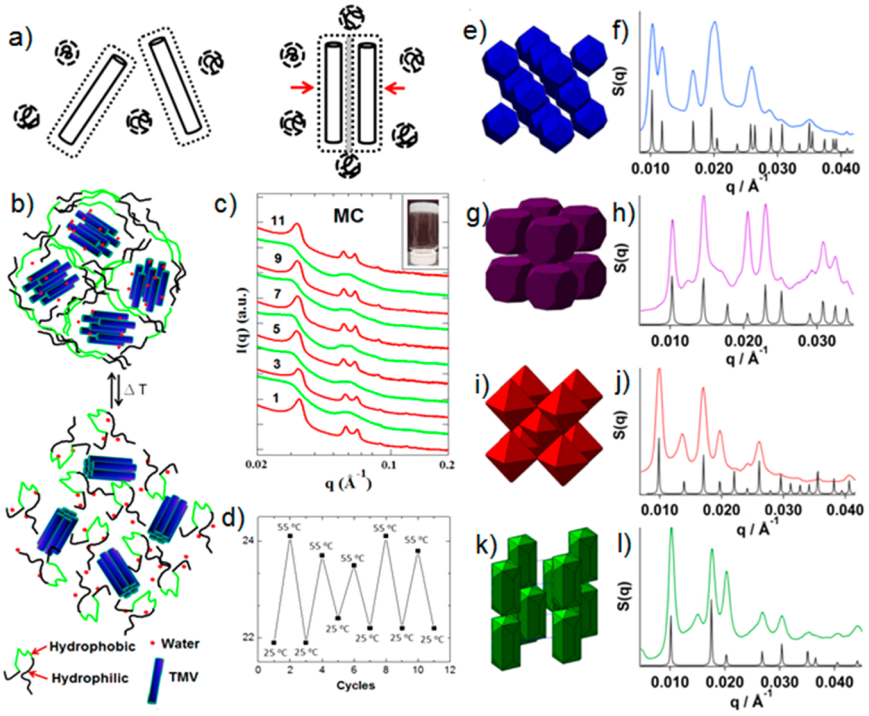

Figure 44. (a) Origin of the depletion interaction. Rodlike particles mixed with depletants (dashed spheres). The shell, whose thickness is identical to the radius of the depletants, is called the depletion layer (dashed lines around the rods). By pushing the rods closer together through osmotic pressure (arrows), the depletants gain free volume by reducing the inaccessible volume (shaded region). (b) Schematic representation of the methylcellulose (MC)/tobacco mosaic virus (TMV) sol–gel transition. MC forms a gel through a hydrophobic interaction. (c) SAXS curves for the samples containing MC with TMV at various temperatures shown in (d) during heating/cooling cycles. The SAXS data in (c) are offset for clarity. (a–d) Modified with permission from ref 428. Copyright 2013 Wiley-VCH Verlag GmbH & Co. KGaA. (e–l) Characterization of superlattices assembled from polyhedra nanoparticles via depletion. Nanoparticle shapes are rhombic dodecahedra (e–f), truncated cubes (g–h), octahedra (i–j), and tetrahexahedra (k–l). (e, g, i, k) Representation of the unit cells formed when the particles assemble. (f, h, j, l) Experimental (colored) and modeled (black) SAXS patterns for the assemblies. (e–l) Modified with permission from ref 70. Copyright 2013 Wiley-VCH Verlag GmbH & Co. KGaA.

DOI: 10.1021/acs.chemrev.5b00690
Chem. Rev. XXXX, XXX, XXX–XXX

7.2.1.2. Functional Organic Ligands. In addition to DNA, there are efforts to employ other functional molecules as ligands, which allow one to utilize various chemical interactions to control nanoparticle assembly. All of the following examples use SAXS for structural characterization. For example, SAXS has been used to determine the interparticle distance of nanoparticle assemblies, where particles are assembled through well-defined metal coordination chemistry (Figure 43a,c).[409,410] There is a substantial body of literature utilizing the assembly behavior of organic molecules that form liquid crystals, or mesogens. Numerous systems of nanoparticles functionalized with mesogenic ligands have been explored, where the assembly behavior of the particle results from the ligand interactions.[411−417] For example, by controlling the radial density profile of a nanoparticle's ligand coronal shell using dendrons, Kanie et al. were able to synthesize non close packed, simple cubic superlattices (see Figure 43b,d).[417] In situ SAXS studies have also been used to examine the phase transitions of structures assembled with mesogenic ligands at different temperatures.[418]

More sophisticated ligand design can lead to diverse crystallographic phase behavior. Cheng and co-workers studied the role of bulky ligands such as fullerenes (C_{60}) or POMs to create Janus and chiral particles as a means to examine directional interactions (see Figure 43e−h).[390,391] They mapped out the phase behavior of these types of particles, determining that the Janus type particles assembled into lamella, while chiral or nonchiral tetrahedra assembled into a diverse range of lamella, double gyroid, triclinic, bcc, or A15 phases, depending on the hydrophilic or hydrophobic properties of the ligand.

Other types of systems have been explored. For example, additional functionality has been build in using ligand shells composed of organic conducting molecules.[419] In the field of nanocomposites, materials with nanoscale structural variations including block copolymers have been utilized to sequester nanoparticles within a particular region of the matrix, thereby controlling the positions of the nanoparticles using the ordered lattice of the polymer.[420−423] SAXS is also useful to monitor the in situ response of these types of materials to various stimuli.[424]

7.2.1.3. Depletion Assembly. When charged particles are mixed with smaller particles or polymers, they can phase separate. These smaller particles, called depleted particles or depletants, then impose an osmotic compressive force on the domains of the charged particles, leading to the formation of superlattices. This process is known as depletion.[117,425] It is necessary to study the physics of depletion assembly in solution, as any variation in solvent will affect the delicate balance of attractive and repulsive forces. The osmotic pressure is typically generated by adding either surfactant micelles, often the same surfactant used for charge stabilization, or polymers to the nanoparticle solution.[70,117,426−429] The phase separation allows the depletants to explore a wider range of space, increasing the entropy of the system, as depicted in Figure 44a.[428] Consequently, the particles experience an effective attractive interaction, called the depletion interaction. The strength of the interaction is determined by the depletion layer, which is a thin layer with a uniform thickness around the particle's periphery identical to the radius of the depletant (Figure 44a). This interaction is stronger when the particle shape allows for greater overlap between the depletion layers of adjacent particles. Thus, rod-shaped particles including synthetic nanorods[426] and rod-like virus[428] have an inherently greater interaction strength as compared to spherical particles. Coulombic repulsion, which may result from the surfactants on the nanoparticle's surface or the amino acid residues in the virus, balance this entropic attractive interaction caused by the osmotic pressure. Using SAXS, we have also shown that the interaction can be dynamically and reversibly controlled, for example by using a temperature responsive depletant such as methylcellulose (Figure 44b−d). Nanoplates and polyhedral particles have also been assembled by depletion forces (Figure 44e−l).[70,117,429]

SAXS has revealed interesting physics of depletion assembly. In a mean field view, particles assemble into a structure that maximizes the face-to-face configuration because it simultaneously maximizes the depletion layer overlap.[70,117] The face-to-face distance is a strong function of the osmotic pressure and also the shape of the particles. Using SAXS, Young et al. found that truncated particles led to shorter face-to-face distances because of the extra excluded volume generated between the truncated vertices (compare nontruncated rhombic dodecahedra to truncated cubes, Figure 44e−h). Alternatively, the distance between particles can increase when nonconformal shapes are assembled (see Figure 44i−l).[70]

7.2.2. Assemblies Formed through Solvent Evaporation. There are numerous reports describing the structure of superlattices in the dried state after they were assembled in solution. For example, particle superlattices can be precipitated by adding a poor solvent.[52] They can also be assembled by spreading a solution containing particles on the surface of a poor solvent and slowly evaporating the top layer,[430] or by simply increasing the concentration of particles through slow solvent evaporation.[173,310,431−433] Because these superlattices are in the dried state, the structures of these materials have typically been determined by TEM. However, SAXS and WAXS measurements have recently become more popular because they can provide higher resolution data with better statistics over large length scales (angstroms to micrometers).[167,303,434] X-ray scattering provides information that cannot be obtained otherwise. For example, single crystalline assemblies (supercrystals) consisting of cubic nanocrystal building blocks were recently studied. The authors were able to determine the relative orientation of the nanocrystals within the supercrystal using a combination of SAXS and WAXS.[173,309] Significant numbers of in situ SAXS/WAXS studies have been reported for high pressure and high temperature environments. These experiments allow one to understand the mechanical[435−437] and thermal stabilities[432,438] of the assembled materials, and also provide a route to new materials synthesis by directionally fusing nanocrystals by pressure[439] or temperature.[440] In sections 7.2.2.1−7.2.2.3, we discuss several examples of how X-ray scattering has been used in the literature to study nanoparticle superlattices in the dried state.

7.2.2.1. Disorder Due to Drying. When particles are assembled using solvent evaporation methods, there is a high probability of disorder being introduced during the final stages of drying. This loss of order has been observed during in situ SAXS experiments for monolayers[240,306] and 3D superlattices.[195,432] While long-range order is often lost, the assembly may maintain short-range order that includes local symmetry. This structural change results in similar SAXS spectra, but ones that have peak broadening.[441] Stacking faults are also commonly observed, generating diffuse scattering perpendicular to the sliding planes,[442] which smear away form factor minima from monodisperse particles. Drying may also be accompanied

DOI: 10.1021/acs.chemrev.5b00690
Chem. Rev. XXXX, XXX, XXX−XXX

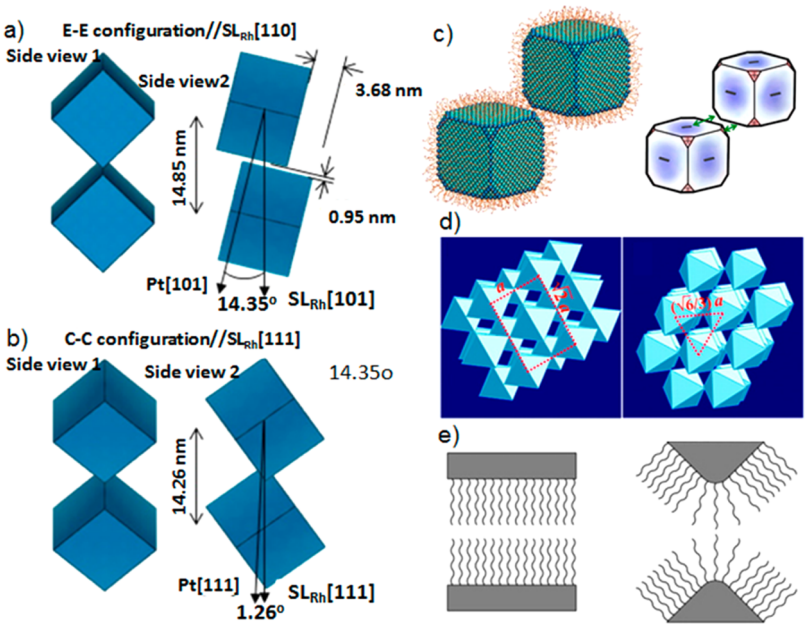

Figure 45. (a, b) Packing configurations in cubic nanoparticle superlattices: (a) edge-to-edge, and (b) corner-to-corner configurations. Modified from ref 173. Copyright 2015 American Chemical Society. (c) Shifted corner-to-corner configuration of truncated nanocubes (TCs). Modified from ref 433. Copyright 2012 American Chemical Society. (d) Model of a bcc superlattice of nanoctahedra showing [110] (left) and [111] (right) projections. Modified from ref 310. Copyright 2011 American Chemical Society. (e) Sketch of ligand interactions between planar surfaces (left) and curved surfaces (right). Modified from ref 451. Copyright 2014 American Chemical Society.

by peak position shift when there is a plastic deformation,[443] and/or peak asymmetry when there is a twin fault.[24] For samples that have been dried, solvent treatment[444] or vapor annealing may change the structure. There are conflicting results[262,445] in the literature as to if this is an effective process to increase order, and requires further study.

7.2.2.2. Non Close Packed Structures. Building off of the literature for micrometer sized colloidal crystals, nanoparticles were initially thought to form close packed structures by hard sphere packing, or van der Waals attractions.[446] However, it was quickly discovered that these models did not adequately describe the packing behavior of some nanoparticle systems coated with stabilizing ligands. Ligand stabilized nanoparticles are often better described as "soft spheres".[118] It was observed that varying the core size[143] or ligand length[143,434] causes a structural transition from a close packed fcc to non close packed bcc. Similar behavior has been observed in systems of block copolymer micelles.[447]

Understanding non close packed structures requires precise measurements of gap distances, the relative orientation of nanocrystals within the superlattice, as well as their size and shape. Nanoparticle systems modeled as spheres often display some degree of faceting, and are thus not strictly spherical. For example, researchers observed an oriented diffraction pattern in both SAXS and WAXS for a nanocrystal superlattice, which may imply that the nanocrystals were nonspherical.[172,434,446] When particle sphericity decreases further (i.e., for polyhedral particles), the particles often orient with respect to each other within the superlattice, indicating that SAXS and WAXS data will be correlated.[173,446] This combined analysis has been performed for octahedral particles (with minor truncation), which were observed to form bcc superlattices with a (110) texture normal to the substrate. The GIWAXS also had a (110) preferred orientation.[310]

One would expect to observe the highest packing possible for each shape, which corresponds to face-to-face packing.[448] However, some superlattices have also been reported to have non close packed structures,[173] which have been attributed to truncation,[449] excess physisorbed ligands,[450] or anisotropic stress.[173] Low density packing structures in assemblies of nonspherical particles can possess vertex-to-vertex[310,451] or edge-to-edge[433] configurations (see Figure 45a–d) instead of the face-to-face orientations that are known to be preferred when considering van der Waals interactions.[452] Boles and Talapin explained this phenomenon by showing that the vertex-to-vertex contact may cause less steric repulsion and higher van der Waals attraction between ligands (see Figure 45e).[451] Rupich et al. found that smaller PbS particles are less likely to form superlattice twinning boundaries than larger particles.[195] This behavior was explained using a model where the strain energy for the smaller particles was lower than some threshold that the ligand layer could absorb.

In the future, a full statistical analysis of the relative nanocrystal orientations with respect to the superlattice using simultaneous SAXS/WAXS and/or orientation mapping[453] with a microbeam SAXS/WAXS[454] will help elucidate the mechanisms of non close packing or the potential existence of plastic crystal phases.[455]

7.2.2.3. Conformation of Ligands. The distance between particles in a superlattice, or gap distance, is known to affect the optical,[456] mechanical,[457] and electrical[458,459] properties of the resulting material.[460] Importantly, the gap distance can reflect the state of the ligand. For example, when the gap between gold nanoparticles functionalized with alkylthiol ligands decreases such that the ligands are fully interdigitated, the ligand melting temperature increases,[461] resulting in a higher Young's modulus for the superlattice.[457] Further, it is known that electrons can hop between the nearest neighbor gold nanoparticles when their ligands are interdigitated.[462] The effect of the gap distance

DOI: 10.1021/acs.chemrev.5b00690
Chem. Rev. XXXX, XXX, XXX−XXX

is also known to dramatically influence the electronic and optical properties of PbSe nanocrystal films.[463−465]

To understand how the structure of the ligand affects the superlattice properties, it is crucial to determine the gap distance between the particles. SAXS is ideally suited for this type of analysis, because it is possible to measure both particle size and interparticle distance with angstrom resolution, providing statistically meaningful results.

Korgel et al. studied dodecanethiol capped Ag nanoparticles.[118] They found that the ligand surface coverage was approximately 75% regardless of particle diameter. The gap distance was found to be shorter than twice the length of the ligands, which indicates that the ligands are interdigitated and may possess a liquid-like nature due to the particle curvature. Terrill et al. studied[462] the assembly of gold nanoparticles functionalized with octanethiol (C8), dodecanethiol (C12)m and hexadecanethiol (C16). For these dried assemblies, they found that the length of the interdigitated section increases with the number of carbons in the alkyl chain.

Others noted that these results were dependent on solvent vapor pressure during the drying process. Wan et al. studied the gap distance of 5 and 7 nm particles functionalized with C12, C14, and C16 alkanethiols.[445] When the assemblies are formed under 0 solvent vapor pressure, the gap distances increased with chain length. Similar to Terrill's work, the length of the interdigitated section increased for longer ligands. However, when the vapor pressure was increased to above 37%, the gap distances were constant regardless of particle size and chain length, which was attributed to physisorbed alkylthiols and residual solvent trapped between the nanoparticles. Further, they showed that the gap distance reversibly increased and decreased as solvent vapor was introduced and removed. Upon solvent vapor injection, the degree of ordering degraded, though the structure returned after removal of the vapor.

The ligand shell of semiconductor PbS nanocrystals assembled into superlattice structures is also interdigitated.[434] Interestingly, the degree of interdigitation was found to depend on particle size. Baranov et al. varied the particle diameter using a fixed ligand length (oleic acid). They found the gap distance of 1.1 nm, which is shorter than the length of the ligand itself, did not change for particles smaller than 5 nm.[444] However, as the particle size increased from 5 to 8.9 nm, the gap distance increased linearly from 1.1 to 3.4 nm, or approximately twice the length of oleic acid. Thus, the length of the interdigitated region decreased with particle size.

The solvent can substantially affect the ligand structure, thereby affecting the gap distance. The results by Goodfellow et al.[432] were consistent with those of Baranov et al. as discussed above. They drop-cast 6.6 nm oleic acid coated PbSe nanoparticles in a good solvent (50:50 toluene:hexane). After evaporation, they obtained a bcc superlattice with a gap distance of 2.6 nm. Interestingly, Lee et al. found that the same kind of particles (7 nm PbS particles coated with oleic acid) formed an fcc superlattice with a gap distance of 1.4 nm.[438] In their work, the superlattice was prepared using a destabilization driven assembly by mixing a poor solvent (isopropanol) into a solution of particles in toluene.[466] The short gap distance may be attributed to a coiled conformation in the ligand due to the poor solvent. The thermal responses of these two structures were opposite. While the gap distance in the bcc lattice shrunk by 0.5 nm upon heating at 150 °C, that of the fcc expanded by approximately 0.7 nm. This result indicates that the ligands on both samples may approach an equilibrium state upon annealing.

Hanrath et al. studied the effect of evaporation speed on the gap distance of oleic acid coated PbS (6.4 nm) and PbSe (6.1 nm) nanoparticles.[262] They observed that fast evaporation (faster than particle diffusion speed in solution) led to shorter gaps (3.2 and 2.2 nm gaps for PbS and PbSe, respectively) than slow evaporation (3.3 and 3.0 nm, respectively). This result indicates that the kinetics of assembly have a substantial effect on the gap distance.

However, these results discussed above indicate that the gap distance depends on sample preparation. There are also experimental limitations that introduce further questions. First, the majority of these studies assume that the particles are spherical. If nonspherical particles are randomly oriented into a superlattice, the unit cell size of the superlattice should increase due to rotational entropy.[70,455] Sphericity of the particles needs to be confirmed or taken into account during the analysis. Second, many of assemblies present a peak or a set of broad peaks, which makes it hard to determine the symmetry of the structure and therefore the center-to-center and gap distances. While the mathematical relationship between the interparticle distance and the first order peak position is identical for structures with fcc and bcc symmetry, it is different for symmetries such as 1D arrays, 2D hexagonal packing, or 3D cubic packing.

7.3. Operando Characterization Using in Situ SAXS and Combined Techniques

One grand challenge of basic science is to gain a better understanding of the mechanisms and dynamics of reactive material transformations in real conditions. Considering the complexity of many reactive systems, which may include complicated reactive materials, high temperature and pressure environments, as well as the existence of both reactants and products, it is important to apply operando techniques to characterize these reactive materials.[5,223,297,467] Multiple synchrotron X-ray techniques including, for example X-ray absorption spectroscopy (XAS), can be integrated with SAXS to provide a unique approach to analyze complex samples and develop a more complete understanding of a given reaction mechanism.[5,361,362,468−471] To achieve a high time resolution for operando studies, both X-ray scattering and spectroscopy require a high flux and brilliance, which, again, requires a synchrotron X-ray source. In this section, we will mainly focus on the utilization of SAXS, or the combination of SAXS with other techniques for the operando characterization of a variety of catalytic materials for energy applications in the fields of fuel cells, heterogeneous catalysis, and electrochemical energy storage.

7.3.1. Fuel Cells. Polymer exchange membrane fuel cells are a promising high-efficiency energy conversion technology that can be used for transport applications. However, the technology is hindered by the deactivation of the Pt nanoparticle electrocatalyst during the reaction, which reduces the efficiency and limits operational cycling.[472] To reduce loading of the high cost Pt catalyst, it is a necessary to understand the mechanisms governing the underlying processes of Pt deactivation under operating conditions. To elucidate electrocatalyst degradation pathways, Gilbert et al. studied Pt nanoparticle growth during potential cycling of the electrocatalyst in an aqueous acidic environment using operando ASAXS.[471] Over the first 80 potential cycles, they found the

DOI: 10.1021/acs.chemrev.5b00690
Chem. Rev. XXXX, XXX, XXX−XXX

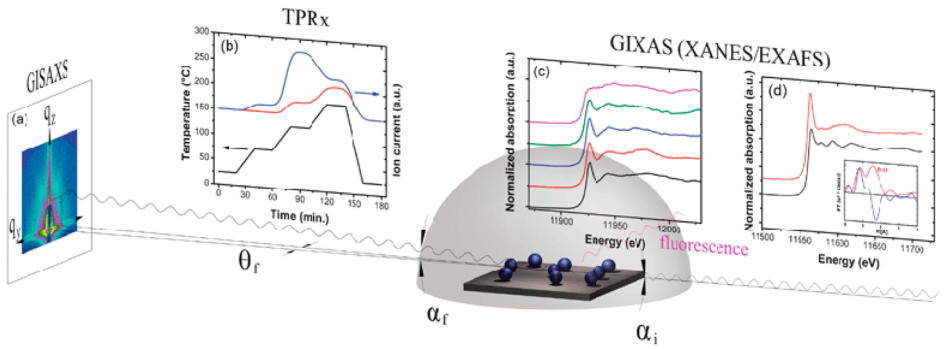

Figure 46. Schematic of combined temperature-programmed reaction, grazing-incidence X-ray scattering, and X-ray absorption (X-ray absorption near-edge spectroscopy, XANES; extended X-ray absorption fine structure, EXAFS) experimental setup. The insets illustrate the capabilities offered by this combination of techniques: (a) 2D in situ GISAXS pattern that allows for the determination of particle size and shape and to study particle stability, (b) monitoring of product evolution with temperature/time, (c) series of XANES spectra collected during in situ reduction of small gold nanoparticles, and (d) example of a quick EXAFS scan on Pt10 atomic clusters revealing fully oxidized Pt. Adapted with permission from ref 474. Copyright 2010 PCCP Owner Societies.

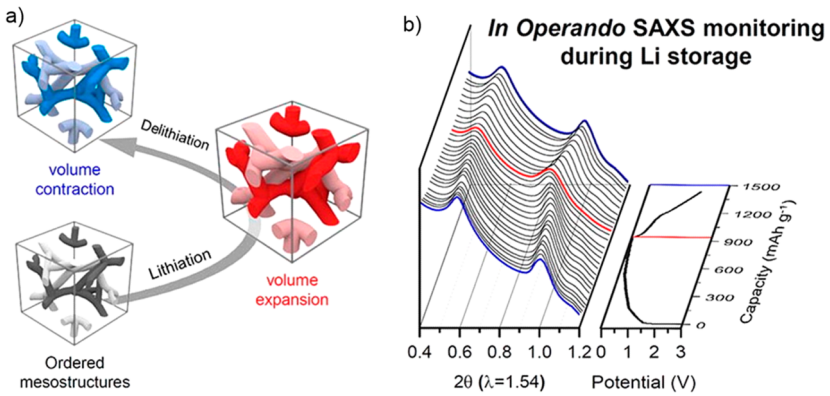

Figure 47. (a) Schematic illustration depicting the volume change of mesoporous metal oxide electrodes during cycling. (b) Operando SAXS profiles of TiO_2 mesoporous electrodes during lithiation and delithiation. Modified from ref 468. Copyright 2015 American Chemical Society.

dominant deactivation mechanism of Pt includes two parts: (1) the preferential dissolution of the smallest particles and (2) the reprecipitation of the dissolved species onto existing particles, resulting in Pt particle growth. They further demonstrated that oxide coverage plays a key role in the Pt dissolution process and in the corresponding growth of the Pt nanoparticle. Recently, the mechanisms of Pt deactivation were further examined during accelerated stress tests to compare the results to those observed in an aqueous environment. During these stress tests, the deactivation was also dominated by the loss of particles smaller than a critical diameter, which was found to be ∼3.5 to ∼4 nm.[467] In addition, they compared Pt_3Co alloy nanocatalyst with pure Pt nanocatalyst in an operando fuel cell as well as in an aqueous environment. In this study, particles below a critical diameter also dissolved. They found the critical particle diameter size of Pt_3Co is in the range 5.2−6.1 nm and it has a higher degradation rate than Pt.[473]

7.3.2. Heterogeneous Catalysts. Detailed insight into the working principles of heterogeneous catalysts under operando conditions are of great importance for improving their catalytic performance and subsequent redesign. Catalysts are very complex structures and possess many different potentially active sites that are highly dependent on composition, size, and morphology. Determining the nature of these sites, and their interaction with the support, as well as information concerning their role in the specific catalytic reaction, is of chief importance for rational catalyst design. A combination of temperature-programmed reaction (TPR) with in situ GISAXS and GIXAS can be used to monitor catalytic activity of the supported nanoparticles to obtain the particle size and oxidation state under reaction conditions,[474] as shown in Figure 46.

Winans et al. performed an in situ GISAXS study of the thermal stability of supported Pt nanoparticles on a silicon wafer.[476] The analysis revealed that Pt nanoparticles maintained their original size up to approximately 320 °C. Above that temperature, agglomeration occurred. They further studied the size evolution of Pt nanoparticles as a function of the Pt surface coverage using anomalous GISAXS. Anisotropic subnanometer-sized nanoparticles coalesced on amorphous substrates. Interestingly, the shape became spherical as the sizes increased.[283]

Laoufi et al. performed operando work to investigate the relationship between the catalytic activity and size/shape of gold nanoparticles supported on TiO_2 during CO oxidation using GISAXS.[477] The occurrence of CO oxidation led to a sintering of Au particles, which is directly correlated to the reaction rate. The catalytic activity was the highest for particles that had a horizontal diameter of 2.1 ± 0.3 nm and a height of about six atomic layers. They further monitored the changes in size and shape of Pt particles in the presence and absence of a MgO(001) support as a function of CO pressure using GISAXS. While the Pt particles were stable on the MgO support, they found that Pt nanoparticles with sizes below 2 nm

DOI: 10.1021/acs.chemrev.5b00690
Chem. Rev. XXXX, XXX, XXX−XXX

were unstable without the support after exposure to CO at partial pressures higher than 10^{-1} Pa.[478]

The Stefan group further studied nanocatalyst size effects on the catalytic reactivity using well-defined atomic clusters. For example, they investigated the oxidative dehydrogenation of propane using Pt8−Pt10 clusters on Al_2O_3 and found that the reactivity and selectivity are much higher than the previously studied Pt nanocatalyst due to a high activation energy.[479] They further investigated different Au6−Au10 clusters[480] and Ag3 clusters for propylene epoxidation.[481] Both systems were effective in the formation of propylene oxide at low temperatures. However, while Au clusters maintained their size, the Ag3 clusters aggregated to 3.5 nm. Recently, Lee et al. prepared Co27 clusters to study the effect of the support on the oxidative dehydrogenation of cyclohexene.[475] The activity of the clusters supported on MgO was much higher than that for other ZnO, TiO_2, and Al_2O_3 supports due to the formation of a mixed Co−Mg−O phase under reaction conditions.

7.3.3. Battery Electrodes. Operando SAXS is useful for characterizing lithium ion batteries for energy storage. Conventional lithium ion batteries suffer from capacity loss due to a variety of failure mechanisms related to the strain imposed on anode and cathode materials upon lithiation and delithiation. Recently, ordered mesoporous materials have been recognized as promising candidates for the next generation of electrode materials because their ordered framework of mesopores can act as a physical buffer for these volume changes.[23,482] Recently, Park et al. reported operando SAXS to study mesoscopic structural changes from ordered mesoporous electrode materials during cycling, as illustrated in Figure 47.[468] In their work, three different ordered mesoporous materials were examined, including TiO_2 (intercalation reaction), Co_3O_4 (conversion reaction), and SnO_2 (conversion and alloying reaction). The variation of the mesoscopic unit cell volumes upon lithiation and delithiation was measured using SAXS. The authors found a reversible and relatively small volume change for TiO_2, which provided evidence that the mesopores can in fact effectively accommodate the volume expansion of the crystalline framework during lithium intercalation.

As a second example, conversion battery electrodes have been examined with SAXS and PDF. These electrodes are attractive due to higher energy storage capacity than conventional intercalation electrodes. Further, Fe-based materials are abundant and cheap, and allow one to access multiple oxidation states. However, these Fe-based conversion electrodes suffer from poor stability due to growth and aggregation of metallic Fe nanoparticles. Wiaderek et al. combined operando SAXS and atomic PDF analysis to study Fe-based electrode materials with various anions, including fluorides, oxyfluorides, and oxides.[469] They found that the anion chemistry of the electrode affected the final Fe particle size and morphology. For example, in the case of the fluorine-rich environment, Fe atoms had enhanced mobility, which led to faster particle growth. More defects were found within the Fe nanoparticles in the oxygen-rich environment; the particles grew through defect annealing. For the mixed oxyfluoride system, unusual nanostructures were formed that did not result in an interconnected network of Fe nanoparticles, which was attributed to competitive growth mechanisms of the two anionic systems.

8. CONCLUSION AND OUTLOOK

SAXS is a nanoscale characterization technique that has been used for a century and applied to diverse fields of study. We have provided a review of the literature that employs SAXS as a tool for the characterization of nanoparticle systems and, in particular, have highlighted areas where SAXS can provide unique characterization capabilities to examine samples in real time and in real environments. We have discussed theoretical developments that are beneficial for the analysis of SAXS data, and have provided examples of their use in the literature for the characterization of systems ranging from individual nanoparticles to their assemblies. Both real space and reciprocal space methods have been thoroughly described for the analysis of complex structures, which have benefited greatly from computational advancements.

A variety of technical developments have expanded the SAXS portfolio. GISAXS, which is a reflection mode version of SAXS, has allowed researchers to examine particle monolayers and nanostructured films. In situ and operando studies have gained significant attention for energy-related materials studies. SAXS has been combined with other techniques that include the use of X-ray (i.e., XAS and WAXS) and non-X-ray characterization (i.e., UV−vis, Raman, mass spectrometry, etc.). These multimodal measurements have allowed researchers a better understanding of chemical transformation in a variety of fields where nanoscale structure is of interest, including catalysis and energy storage.

As nanoparticles become increasingly incorporated into a variety of functional materials, it will become ever more important to gain a deep understanding of their structure−property relationships. Modern SAXS techniques are being developed for this purpose. One grand challenge is the routine reconstruction of nanoparticle size and shape in real space, an application that is beginning to be realized using coherent SAXS,[483,484] and will greatly benefit from further development in X-ray sources. SAXS tomography[485,486] is another example that has recently begun to show potential. As always, with the development of new experimental methodology in particular for in situ and operando SAXS, it will be critical to make further advances in the design of sample environments. These have benefited greatly in recent years from the rapid prototyping capabilities of 3D printing. In addition, advanced computing facilities and new software packages will allow for automation and the routine analysis of large and complex data sets. These and other developments will be facilitated by the emergence of new and brighter X-ray sources throughout the world.

AUTHOR INFORMATION

Corresponding Author

*E-mail: blee@anl.gov.

Notes

The authors declare no competing financial interest.

Biographies

Tao Li (taoli@aps.anl.gov) is assistant scientist of the Advanced Photon Source at Argonne National Lab. His research interests focus on using advanced X-ray techniques, especially small angle X-ray scattering, to study the self-assembly of nanoparticles into functional materials in the field of energy and nanomedicine. Dr. Li earned his bachelor's degree in polymer material science and engineering from the East China University of Science and Technology (ECUST) in 2003. He completed his Ph.D. in the Department of Chemistry and Biochemistry at the University of South Carolina—Columbia in 2009. Dr. Li has authored/coauthored more than 40 peer-reviewed research papers.

DOI: 10.1021/acs.chemrev.5b00690
Chem. Rev. XXXX, XXX, XXX−XXX

Andrew J. Senesi (ajsenesi@anl.gov) received his B.A. in chemistry from Kalamazoo College in 2004. After a brief stint abroad, he completed his Ph.D. in chemistry with Prof. Chad Mirkin at Northwestern University focusing on nanoscale lithography and the DNA-directed assembly of nanoparticles. He is currently a postdoctoral scholar at Argonne National Lab, with research interests in the use of SAXS for the organization of nanoscale systems and energy applications.

Byeongdu Lee is a physicist at the Advanced Photon Source (APS) in the Argonne National Laboratory (ANL). He has been using SAXS and SANS since he was a graduate student of the department of chemistry at POSTECH in Korea. He obtained a Ph.D. in polymer physics by studying polymer crystallization and nanoporous materials using SAXS and GISAXS. After he joined the APS, his research focus has been on nanoparticles and their assemblies. He was awarded the Young Scientist Award from the IUCr small angle scattering committee in 2006. He served as a chair of the small angle scattering interest group of the American Crystallography Association.

ACKNOWLEDGMENTS

The authors were supported by the U.S. DOE under Contract No. DE-AC02-06CH11357.

REFERENCES

(1) Chu, B.; Hsiao, B. S. Small-Angle X-ray Scattering of Polymers. *Chem. Rev.* **2001**, *101*, 1727−1762.

(2) Daniel, M.-C.; Astruc, D. Gold Nanoparticles: Assembly, Supramolecular Chemistry, Quantum-Size-Related Properties, and Applications toward Biology, Catalysis, and Nanotechnology. *Chem. Rev.* **2004**, *104*, 293−346.

(3) Renaud, G.; Lazzari, R.; Leroy, F. Probing Surface and Interface Morphology with Grazing Incidence Small Angle X-Ray Scattering. *Surf. Sci. Rep.* **2009**, *64*, 255−380.

(4) Talapin, D. V.; Lee, J.-S.; Kovalenko, M. V.; Shevchenko, E. V. Prospects of Colloidal Nanocrystals for Electronic and Optoelectronic Applications. *Chem. Rev.* **2010**, *110*, 389−458.

(5) Newton, M. A.; van Beek, W. Combining Synchrotron-Based X-ray Techniques with Vibrational Spectroscopies for the In Situ Study of Heterogeneous Catalysts: A View from A Bridge. *Chem. Soc. Rev.* **2010**, *39*, 4845−4863.

(6) Bentrup, U. Combining In Situ Characterization Methods in One Set-Up: Looking with More Eyes into the Intricate Chemistry of the Synthesis and Working of Heterogeneous Catalysts. *Chem. Soc. Rev.* **2010**, *39*, 4718−4730.

(7) Rivnay, J.; Mannsfeld, S. C. B.; Miller, C. E.; Salleo, A.; Toney, M. F. Quantitative Determination of Organic Semiconductor Microstructure from the Molecular to Device Scale. *Chem. Rev.* **2012**, *112*, 5488−5519.

(8) Wang, Y.; Wang, Y.; Breed, D. R.; Manoharan, V. N.; Feng, L.; Hollingsworth, A. D.; Weck, M.; Pine, D. J. Colloids with Valence and Specific Directional Bonding. *Nature* **2012**, *491*, 51−55.

(9) Morita, T.; Nishikawa, K. Fluctuations in Density and Concentration of Methanol−Water Mixtures at 7 MPa and 373, 423 K Studied by Small-Angle X-ray Scattering. *Chem. Phys. Lett.* **2004**, *389*, 29−33.

(10) Bates, F. S.; Fredrickson, G. H. Block Copolymer Thermodynamics: Theory and Experiment. *Annu. Rev. Phys. Chem.* **1990**, *41*, 525−557.

(11) Lee, B.; Park, Y.-H.; Hwang, Y.-T.; Oh, W.; Yoon, J.; Ree, M. Ultralow-k Nanoporous Organosilicate Dielectric Films Imprinted with Dendritic Spheres. *Nat. Mater.* **2005**, *4*, 147−150.

(12) Macfarlane, R. J.; Lee, B.; Jones, M. R.; Harris, N.; Schatz, G. C.; Mirkin, C. A. Nanoparticle Superlattice Engineering with DNA. *Science* **2011**, *334*, 204−208.

(13) Sztucki, M.; Narayanan, T.; Belina, G.; Moussaïd, A.; Pignon, F.; Hoekstra, H. Kinetic Arrest and Glass-Glass Transition in Short-Ranged Attractive Colloids. *Phys. Rev. E* **2006**, *74*, 051504.

(14) *Applications of Synchrotron Light to Scattering and Diffraction in Materials and Life Sciences*; Ezquerra, T. A., Garcia-Gutierrez, M. C., Nogales, A., Gomez, M., Eds.; Lecture Notes in Physics 776; Springer: Berlin, 2009.

(15) Peterson, V. K.; Papadakis, C. M. Functional Materials Analysis using In Situ and In Operando X-ray and Neutron Scattering. *IUCrJ* **2015**, *2*, 292−304.

(16) Mertens, H. D. T.; Svergun, D. I. Structural Characterization of Proteins and Complexes using Small-Angle X-ray Solution Scattering. *J. Struct. Biol.* **2010**, *172*, 128−141.

(17) Guinier, A.; Fournet, G. *Small-Angle Scattering of X-rays*; John Wiley & Sons, Inc.: New York, 1955.

(18) Turkevich, J.; Hubbell, H. H. Low Angle X-Ray Diffraction of Colloidal Gold and Carbon Black[1a]. *J. Am. Chem. Soc.* **1951**, *73*, 1−7.

(19) *Modern Aspects of Small-Angle Scattering*; Springer: Dordrecht, Netherlands, 1995.

(20) Thiele, E. Equation of State for Hard Spheres. *J. Chem. Phys.* **1963**, *39*, 474−479.

(21) Brown, W. *Light Scattering: Principles and Development*, 1st ed.; Clarendon Press: New York, 1996.

(22) Pedersen, J. S. Analysis of Small-Angle Scattering Data from Colloids and Polymer Solutions: Modeling and Least-Squares Fitting. *Adv. Colloid Interface Sci.* **1997**, *70*, 171−210.

(23) Ren, Y.; Ma, Z.; Bruce, P. G. Ordered Mesoporous Metal Oxides: Synthesis and Applications. *Chem. Soc. Rev.* **2012**, *41*, 4909−4927.

(24) Ingham, B. X-ray Scattering Characterisation of Nanoparticles. *Crystallogr. Rev.* **2015**, *21*, 229−303.

(25) Roe, R.-J. *Methods of X-ray and Neutron Scattering in Polymer Science*; Oxford University Press: New York, 2000.

(26) Blanton, T. N.; Barnes, C. L.; Lelental, M. Preparation of Silver Behenate Coatings to Provide Low- to Mid-Angle Diffraction Calibration. *J. Appl. Crystallogr.* **2000**, *33*, 172−173.

(27) Zhang, F.; Ilavsky, J.; Long, G.; Quintana, J. G.; Allen, A.; Jemian, P. Glassy Carbon as An Absolute Intensity Calibration Standard for Small-Angle Scattering. *Metall. Mater. Trans. A* **2010**, *41*, 1151−1158.

(28) Orthaber, D.; Bergmann, A.; Glatter, O. SAXS Experiments on Absolute Scale with Kratky Systems using Water as a Secondary Standard. *J. Appl. Crystallogr.* **2000**, *33*, 218−225.

(29) Wang, W.; Murthy, N. S.; Grubb, D. T. 'Butterfly' Small-Angle X-ray Scattering Patterns in Semicrystalline Polymers Are Double-Elliptical. *Polymer* **2007**, *48*, 3393−3399.

(30) Pauw, B. R. Everything SAXS: Small-Angle Scattering Pattern Collection and Correction. *J. Phys.: Condens. Matter* **2013**, *25*, 383201.

(31) Hammersley, A. P. *FIT2D: An Introduction and Overview*; ESRF Internal Report; 1997.

(32) Ilavsky, J. Nika: Software for Two-Dimensional Data Reduction. *J. Appl. Crystallogr.* **2012**, *45*, 324−328.

(33) Bressler, I.; Kohlbrecher, J.; Thunemann, A. F. SASfit: A Tool for Small-Angle Scattering Data Analysis using A Library of Analytical Expressions. *J. Appl. Crystallogr.* **2015**, *48*, 1587−1598.

(34) Ilavsky, J.; Jemian, P. R. Irena: Tool Suite for Modeling and Analysis of Small-Angle Scattering. *J. Appl. Crystallogr.* **2009**, *42*, 347−353.

(35) Pedersen, M. C.; Arleth, L.; Mortensen, K. WillItFit: a Framework for Fitting of Constrained Models to Small-Angle Scattering Data. *J. Appl. Crystallogr.* **2013**, *46*, 1894−1898.

(36) Forster, S.; Apostol, L.; Bras, W. Scatter: Software for the Analysis of Nano- and Mesoscale Small-Angle Scattering. *J. Appl. Crystallogr.* **2010**, *43*, 639−646.

(37) SasView for Small Angle Scattering Analysis. http://www.sasview.org/.

(38) Svergun, D.; Barberato, C.; Koch, M. H. J. CRYSOL - A Program to Evaluate X-ray Solution Scattering of Biological Macro-

DOI: 10.1021/acs.chemrev.5b00690
Chem. Rev. XXXX, XXX, XXX−XXX

molecules from Atomic Coordinates. *J. Appl. Crystallogr.* **1995**, *28*, 768−773.
(39) Senesi, A. J.; Lee, B. Small-Angle Scattering of Particle Assemblies. *J. Appl. Crystallogr.* **2015**, *48*, 1172−1182.
(40) Jiang, Z. GIXSGUI: A MATLAB toolbox for Grazing-Incidence X-ray Scattering Data Visualization and Reduction, and Indexing of Buried Three-Dimensional Periodic Nanostructured Films. *J. Appl. Crystallogr.* **2015**, *48*, 917−926.
(41) Lazzari, R. IsGISAXS: A Program for Grazing-Incidence Small-Angle X-ray Scattering Analysis of Supported Islands. *J. Appl. Crystallogr.* **2002**, *35*, 406−421.
(42) Lee, B. Software. https://sites.google.com/site/byeongdu/software.
(43) Babonneau, D. FitGISAXS: Software Package for Modelling and Analysis of GISAXS data using IGOR Pro. *J. Appl. Crystallogr.* **2010**, *43*, 929−936.
(44) SAS Portal. http://smallangle.org/.
(45) Advanced Photon Source: Catalog of Data Analysis Software. https://www1.aps.anl.gov/science/scientific-software.
(46) Hosemann, R.; Bagchi, S. N. *Direct Analysis of Diffraction by Matter*; North-Holland: Amsterdam, 1962.
(47) Pedersen, J. Determination of Size Distribution from Small-Angle Scattering Data for Systems with Effective Hard-Sphere Interactions. *J. Appl. Crystallogr.* **1994**, *27*, 595−608.
(48) Kaler, E. W. In *Modern Aspects of Small-Angle Scattering*; Brumberger, H., Ed.; Springer: Milan, Italy, 1995.
(49) Förster, S.; Timmann, A.; Konrad, M.; Schellbach, C.; Meyer, A.; Funari, S. S.; Mulvaney, P.; Knott, R. Scattering Curves of Ordered Mesoscopic Materials. *J. Phys. Chem. B* **2005**, *109*, 1347−1360.
(50) Ye, X.; Millan, J. A.; Engel, M.; Chen, J.; Diroll, B. T.; Glotzer, S. C.; Murray, C. B. Shape Alloys of Nanorods and Nanospheres from Self-Assembly. *Nano Lett.* **2013**, *13*, 4980−4988.
(51) Ye, X.; Chen, J.; Engel, M.; Millan, J. A.; Li, W.; Qi, L.; Xing, G.; Collins, J. E.; Kagan, C. R.; Li, J.; et al. Competition of Shape and Interaction Patchiness for Self-Assembling Nanoplates. *Nat. Chem.* **2013**, *5*, 466−473.
(52) Shevchenko, E. V.; Talapin, D. V.; Kotov, N. A.; O'Brien, S.; Murray, C. B. Structural Diversity in Binary Nanoparticle Superlattices. *Nature* **2006**, *439*, 55−59.
(53) Bartlett, P.; Ottewill, R. H.; Pusey, P. N. Superlattice Formation in Binary Mixtures of Hard-Sphere Colloids. *Phys. Rev. Lett.* **1992**, *68*, 3801−3804.
(54) Bartlett, P.; Campbell, A. I. Three-Dimensional Binary Superlattices of Oppositely Charged Colloids. *Phys. Rev. Lett.* **2005**, *95*, 128302.
(55) Leunissen, M. E.; Christova, C. G.; Hynninen, A. P.; Royall, C. P.; Campbell, A. I.; Imhof, A.; Dijkstra, M.; van Roij, R.; van Blaaderen, A. Ionic Colloidal Crystals of Oppositely Charged Particles. *Nature* **2005**, *437*, 235−240.
(56) Kalsin, A. M.; Fialkowski, M.; Paszewski, M.; Smoukov, S. K.; Bishop, K. J. M.; Grzybowski, B. A. Electrostatic Self-Assembly of Binary Nanoparticle Crystals with A Diamond-Like Lattice. *Science* **2006**, *312*, 420−424.
(57) Park, S. Y.; Lytton-Jean, A. K. R.; Lee, B.; Weigand, S.; Schatz, G. C.; Mirkin, C. A. DNA-Programmable Nanoparticle Crystallization. *Nature* **2008**, *451*, 553−556.
(58) Nykypanchuk, D.; Maye, M. M.; van der Lelie, D.; Gang, O. DNA-Guided Crystallization of Colloidal Nanoparticles. *Nature* **2008**, *451*, 549−552.
(59) Wagner, J.; Härtl, W.; Hempelmann, R. Characterization of Monodisperse Colloidal Particles: Comparison between SAXS and DLS. *Langmuir* **2000**, *16*, 4080−4085.
(60) Sanders, J. V. Close-Packed Structures of Spheres of Two Different Sizes I. Observations on Natural Opal. *Philos. Mag. A* **1980**, *42*, 705−720.
(61) Senesi, A. J.; Eichelsdoerfer, D. J.; Brown, K. A.; Lee, B.; Auyeung, E.; Choi, C. H. J.; Macfarlane, R. J.; Young, K. L.; Mirkin, C. A. Oligonucleotide Flexibility Dictates Crystal Quality in DNA-Programmable Nanoparticle Superlattices. *Adv. Mater.* **2014**, *26*, 7235−7240.
(62) Feigin, L. A.; Svergun, D. I. *Structure Analysis by Small-Angle X-ray and Nuetron Scattering*; Plenum Press: New York, 1987.
(63) Li, X.; Shew, C.-Y.; He, L.; Meilleur, F.; Myles, D. A. A.; Liu, E.; Zhang, Y.; Smith, G. S.; Herwig, K. W.; Pynn, R.; et al. Scattering Functions of Platonic Solids. *J. Appl. Crystallogr.* **2011**, *44*, 545−557.
(64) Senesi, A.; Lee, B. Small Angle Scattering Function of Polyhedral Particles. *J. Appl. Crystallogr.* **2015**, *48*, 565−577.
(65) Debye, P.; Bueche, A. M. Scattering by An Inhomogeneous Solid. *J. Appl. Phys.* **1949**, *20*, 518−525.
(66) Alves, C.; Pedersen, J. S.; Oliveira, C. L. P. Modelling of High-Symmetry Nanoscale Particles bySmall-Angle Scattering. *J. Appl. Crystallogr.* **2014**, *47*, 84−94.
(67) Gordon, T. R.; Diroll, B. T.; Paik, T.; Doan-Nguyen, V. V. T.; Gaulding, E. A.; Murray, C. B. Characterization of Shape and Monodispersity of Anisotropic Nanocrystals through Atomistic X-ray Scattering Simulation. *Chem. Mater.* **2015**, *27*, 2502−2506.
(68) Chourou, S. T.; Sarje, A.; Li, X. S.; Chan, E. R.; Hexemer, A. HipGISAXS: A High-Performance Computing Code for Simulating Grazing-Incidence X-ray Scattering Data. *J. Appl. Crystallogr.* **2013**, *46*, 1781−1795.
(69) Pedersen, J. S. In *Neutrons, X-rays and Light: Scattering Methods Applied to Soft Condensed Matter*; Zemb, T., Lindner, P., Eds.; Elsevier Science: North Holland, 2002.
(70) Young, K. L.; Personick, M. L.; Engel, M.; Damasceno, P. F.; Barnaby, S. N.; Bleher, R.; Li, T.; Glotzer, S. C.; Lee, B.; Mirkin, C. A. A Directional Entropic Force Approach to Assemble Anisotropic Nanoparticles into Superlattices. *Angew. Chem., Int. Ed.* **2013**, *52*, 13980−13984.
(71) Kriechbaum, M. Rg-Calculator of Polyhedra. http://www.staff.tugraz.at/manfred.kriechbaum/xitami/java/rgpolyhedra.html, 2014.
(72) Xu, R.; Jiang, H.; Song, C.; Rodriguez, J. A.; Huang, Z.; Chen, C.-C.; Nam, D.; Park, J.; Gallagher-Jones, M.; Kim, S.; et al. Single-Shot Three-Dimensional Structure Determination of Nanocrystals with Femtosecond X-ray Free-Electron Laser Pulses. *Nat. Commun.* **2014**, *5*, 4061.
(73) Takahashi, Y.; Suzuki, A.; Zettsu, N.; Oroguchi, T.; Takayama, Y.; Sekiguchi, Y.; Kobayashi, A.; Yamamoto, M.; Nakasako, M. Coherent Diffraction Imaging Analysis of Shape-Controlled Nanoparticles with Focused Hard X-ray Free-Electron Laser Pulses. *Nano Lett.* **2013**, *13*, 6028−6032.
(74) Barke, I.; Hartmann, H.; Rupp, D.; Flückiger, L.; Sauppe, M.; Adolph, M.; Schorb, S.; Bostedt, C.; Treusch, R.; Peltz, C.; et al. The 3D-Architecture of Individual Free Silver Nanoparticles Captured by X-ray Scattering. *Nat. Commun.* **2015**, *6*, 6187.
(75) Takahashi, Y.; Zettsu, N.; Nishino, Y.; Tsutsumi, R.; Matsubara, E.; Ishikawa, T.; Yamauchi, K. Three-Dimensional Electron Density Mapping of Shape-Controlled Nanoparticle by Focused Hard X-ray Diffraction Microscopy. *Nano Lett.* **2010**, *10*, 1922−1926.
(76) Robinson, I.; Harder, R. Coherent X-ray Diffraction Imaging of Strain at the Nanoscale. *Nat. Mater.* **2009**, *8*, 291−298.
(77) Watari, M.; McKendry, R. A.; Vögtli, M.; Aeppli, G.; Soh, Y.-A.; Shi, X.; Xiong, G.; Huang, X.; Harder, R.; Robinson, I. K. Differential Stress Induced by Thiol Adsorption on Facetted Nanocrystals. *Nat. Mater.* **2011**, *10*, 862−866.
(78) Petoukhov, M. V.; Franke, D.; Shkumatov, A. V.; Tria, G.; Kikhney, A. G.; Gajda, M.; Gorba, C.; Mertens, H. D. T.; Konarev, P. V.; Svergun, D. I. New Developments in the ATSAS Program Package for Small-Angle Scattering Data Analysis. *J. Appl. Crystallogr.* **2012**, *45*, 342−350.
(79) Walther, D.; Cohen, F. E.; Doniach, S. Reconstruction of Low-Resolution Three-Dimensional Density Maps from One-Dimensional Small-Angle X-ray Solution Scattering Data for Biomolecules. *J. Appl. Crystallogr.* **2000**, *33*, 350−363.
(80) Boldon, L.; Laliberte, F.; Liu, L. Review of the Fundamental Theories Behind Small Angle X-ray Scattering, Molecular Dynamics Simulations, and Relevant Integrated Application. *Nano Rev.* **2015**, *6*, 25661.

DOI: 10.1021/acs.chemrev.5b00690
Chem. Rev. XXXX, XXX, XXX−XXX

(81) Burian, M.; Fritz-Popovski, G.; He, M.; Kovalenko, M. V.; Paris, O.; Lechner, R. T. Considerations on the Model-Free Shape Retrieval of Inorganic Nanocrystals from Small-Angle Scattering Data. *J. Appl. Crystallogr.* **2015**, *48*, 857−868.
(82) Moglianetti, M.; Ong, Q. K.; Reguera, J.; Harkness, K. M.; Mameli, M.; Radulescu, A.; Kohlbrecher, J.; Jud, C.; Svergun, D. I.; Stellacci, F. Scanning Tunneling Microscopy and Small Angle Neutron Scattering Study of Mixed Monolayer Protected Gold Nanoparticles in Organic Solvents. *Chem. Sci.* **2014**, *5*, 1232−1240.
(83) Aragon, S. R.; Pecora, R. Theory of Dynamic Light Scattering from Polydisperse Systems. *J. Chem. Phys.* **1976**, *64*, 2395−2404.
(84) Borchert, H.; Shevchenko, E. V.; Robert, A.; Mekis, I.; Kornowski, A.; Grübel, G.; Weller, H. Determination of Nanocrystal Sizes: A Comparison of TEM, SAXS, and XRD Studies of Highly Monodisperse CoPt3 Particles. *Langmuir* **2005**, *21*, 1931−1936.
(85) Hansen, S.; Pedersen, J. S. A Comparison of Three Dfferent Mthods for Aalysing Small Angle Scattering Data. *J. Appl. Crystallogr.* **1991**, *24*, 541−548.
(86) Glatter, O. IUCr A New Method for the Evaluation of Small-Angle Scattering Data. *J. Appl. Crystallogr.* **1977**, *10*, 415−421.
(87) Pauw, B. R.; Pedersen, J. S.; Tardif, S.; Takata, M.; Iversen, B. B. Improvements and Considerations for Size Distribution Retrieval from Small-Angle Scattering Data by Monte Carlo Methods. *J. Appl. Crystallogr.* **2013**, *46*, 365−371.
(88) Wang, W.; Chen, X.; Cai, Q.; Mo, G.; Jiang, L. S.; Zhang, K.; Chen, Z. J.; Wu, Z. H.; Pan, W. In Situ SAXS Study on Size Changes of Platinum Nanoparticles with Temperature. *Eur. Phys. J. B* **2008**, *65*, 57−64.
(89) Jellinek, M. H.; Fankuchen, I. X-Ray Examination of Pure Alumina Gel. *Ind. Eng. Chem.* **1949**, *41*, 2259−2265.
(90) Bremholm, M.; Felicissimo, M.; Iversen, B. B. Time-Resolved In Situ Synchrotron X-ray Study and Large-Scale Production of Magnetite Nanoparticles in Supercritical Water. *Angew. Chem.* **2009**, *121*, 4882−4885.
(91) Nakamura, K.; Kawabata, T.; Mori, Y. Size Distribution Analysis of Colloidal Gold by Small Angle X-ray Scattering and Light Absorbance. *Powder Technol.* **2003**, *131*, 120−128.
(92) Pedersen, J. S.; Posselt, D.; Mortensen, K. Analytical Treatment of the Resolution Function for Small-Angle Scattering. *J. Appl. Crystallogr.* **1990**, *23*, 321−333.
(93) Debye, P.; Anderson, H. R.; Brumberger, H. Scattering by An Inhomogeneous Solid. II. The Correlation Function and Its Application. *J. Appl. Phys.* **1957**, *28*, 679−683.
(94) Loubat, A.; Lacroix, L.-M.; Robert, A.; Impéror-Clerc, M.; Poteau, R.; Maron, L.; Arenal, R.; Pansu, B.; Viau, G. Ultrathin Gold Nanowires: Soft-Templating versus Liquid Phase Synthesis, A Quantitative Study. *J. Phys. Chem. C* **2015**, *119*, 4422−4430.
(95) Hammouda, B. A New Guinier-Porod Model. *J. Appl. Crystallogr.* **2010**, *43*, 716−719.
(96) Beaucage, G. Small-Angle Scattering from Polymeric Mass Fractals of Arbitrary Mass-Fractal Dimension. *J. Appl. Crystallogr.* **1996**, *29*, 134−146.
(97) Beaucage, G.; Kammler, H. K.; Pratsinis, S. E. Particle Size Distributions from Small-Angle Scattering using Global Scattering Functions. *J. Appl. Crystallogr.* **2004**, *37*, 523−535.
(98) Leung, C.-Y.; Palmer, L. C.; Kewalramani, S.; Qiao, B.; Stupp, S. I.; Olvera de la Cruz, M.; Bedzyk, M. J. Crystalline Polymorphism Induced by Charge Regulation in Ionic Membranes. *Proc. Natl. Acad. Sci. U. S. A.* **2013**, *110*, 16309−16314.
(99) Skar-Gislinge, N.; Simonsen, J. B.; Mortensen, K.; Feidenhans'l, R.; Sligar, S. G.; Lindberg Møller, B.; Bjørnholm, T.; Arleth, L. Elliptical Structure of Phospholipid Bilayer Nanodiscs Encapsulated by Scaffold Proteins: Casting the Roles of the Lipids and the Protein. *J. Am. Chem. Soc.* **2010**, *132*, 13713−13722.
(100) Hendrickson, W. A. Anomalous Diffraction in Crystallographic Phase Evaluation. *Q. Rev. Biophys.* **2014**, *47*, 49−93.
(101) Sztucki, M.; Di Cola, E.; Narayanan, T. Anomalous Small-Angle X-ray Scattering from Charged Soft Matter. *Eur. Phys. J.: Spec. Top.* **2012**, *208*, 319−331.
(102) Taylor, G. L. Introduction to Phasing. *Acta Crystallogr., Sect. D: Biol. Crystallogr.* **2010**, *66*, 325−338.
(103) Carbone, L.; Cozzoli, P. D. Colloidal Heterostructured Nanocrystals: Synthesis and Growth Mechanisms. *Nano Today* **2010**, *5*, 449−493.
(104) Mokari, T.; Rothenberg, E.; Popov, I.; Costi, R.; Banin, U. Selective Growth of Metal Tips onto Semiconductor Quantum Rods and Tetrapods. *Science* **2004**, *304*, 1787−1790.
(105) Demortière, A.; Schaller, R. D.; Li, T.; Chattopadhyay, S.; Krylova, G.; Shibata, T.; dos Santos Claro, P. C.; Rowland, C. E.; Miller, J. T.; Cook, R.; et al. In Situ Optical and Structural Studies on Photoluminesence Quenching in CdSe/CdS/Au Heterostructures. *J. Am. Chem. Soc.* **2014**, *136*, 2342−2350.
(106) Kwon, S. G.; Krylova, G.; Phillips, P. J.; Klie, R. F.; Chattopadhyay, S.; Shibata, T.; Bunel, E. E.; Liu, Y.; Prakapenka, V. B.; Lee, B.; et al. Heterogeneous Nucleation and Shape Transformation of Multicomponent Metallic Nanostructures. *Nat. Mater.* **2015**, *14*, 215−223.
(107) Pimpinelli, A.; Villain, J. *Physics of Crystal Growth*; Cambridge University Press: 1998.
(108) Pathak, H.; Wyslouzil, B.; Obeidat, A.; Wilemski, G. The Structure of Aqueous-Alkane Nanodroplets. *AIP Conf. Proc.* **2013**, *1527*, 472−475.
(109) Obeidat, A.; Hrahsheh, F.; Wilemski, G. Scattering Form Factors for Russian Doll Aerosol Droplet Models. *J. Phys. Chem. B* **2015**, *119*, 9304−9311.
(110) Pathak, H.; Obeidat, A.; Wilemski, G.; Wyslouzil, B. The Structure of D_2O-Nonane Nanodroplets. *J. Chem. Phys.* **2014**, *140*, 224318.
(111) Kaya, H. Scattering Behaviour of Janus Particles. *Appl. Phys. A: Mater. Sci. Process.* **2002**, *74*, s507−s509.
(112) Fütterer, T.; Vliegenthart, G. A.; Lang, P. R. Particle Scattering Factor of Janus Micelles. *Macromolecules* **2004**, *37*, 8407−8413.
(113) Haas, S.; Zehl, G.; Dorbandt, I.; Manke, I.; Bogdanoff, P.; Fiechter, S.; Hoell, A. Direct Accessing the Nanostructure of Carbon Supported Ru−Se Based Catalysts by ASAXS. *J. Phys. Chem. C* **2010**, *114*, 22375−22384.
(114) Zehl, G.; Schmithals, G.; Hoell, A.; Haas, S.; Hartnig, C.; Dorbandt, I.; Bogdanoff, P.; Fiechter, S. On the Structure of Carbon-Supported Selenium-Modified Ruthenium Nanoparticles as Electrocatalysts for Oxygen Reduction in Fuel Cells. *Angew. Chem., Int. Ed.* **2007**, *46*, 7311−7314.
(115) Kewalramani, S.; Zwanikken, J. W.; Macfarlane, R. J.; Leung, C.-Y.; Olvera de la Cruz, M.; Mirkin, C. A.; Bedzyk, M. J. Counterion Distribution Surrounding Spherical Nucleic Acid−Au Nanoparticle Conjugates Probed by Small-Angle X-ray Scattering. *ACS Nano* **2013**, *7*, 11301−11309.
(116) Gómez-Graña, S.; Hubert, F.; Testard, F.; Guerrero-Martínez, A.; Grillo, I.; Liz-Marzán, L. M.; Spalla, O. Surfactant (Bi)Layers on Gold Nanorods. *Langmuir* **2012**, *28*, 1453−1459.
(117) Young, K. L.; Jones, M. R.; Zhang, J.; Macfarlane, R. J.; Esquivel-Sirvent, R.; Nap, R. J.; Wu, J.; Schatz, G. C.; Lee, B.; Mirkin, C. A. Assembly of Reconfigurable One-Dimensional Colloidal Superlattices due to A Synergy of Fundamental Nanoscale Forces. *Proc. Natl. Acad. Sci. U. S. A.* **2012**, *109*, 2240−2245.
(118) Korgel, B. A.; Fullam, S.; Connolly, S.; Fitzmaurice, D. Assembly and Self-Organization of Silver Nanocrystal Superlattices: Ordered "Soft Spheres. *J. Phys. Chem. B* **1998**, *102*, 8379−8388.
(119) Diroll, B. T.; Weigandt, K. M.; Jishkariani, D.; Cargnello, M.; Murphy, R. J.; Hough, L. A.; Murray, C. B.; Donnio, B. Quantifying "Softness" of Organic Coatings on Gold Nanoparticles Using Correlated Small-Angle X-ray and Neutron Scattering. *Nano Lett.* **2015**, *15*, 8008−8012.
(120) Podsiadlo, P.; Kwon, S. G.; Koo, B.; Lee, B.; Prakapenka, V. B.; Dera, P.; Zhuravlev, K. K.; Krylova, G.; Shevchenko, E. V. How "Hollow" Are Hollow Nanoparticles? *J. Am. Chem. Soc.* **2013**, *135*, 2435−2438.
(121) Krycka, K. L.; Borchers, J. A.; Salazar-Alvarez, G.; López-Ortega, A.; Estrader, M.; Estradé, S.; Winkler, E.; Zysler, R. D.; Sort, J.;

DOI: 10.1021/acs.chemrev.5b00690
Chem. Rev. XXXX, XXX, XXX−XXX

Peiró, F.; et al. Resolving Material-Specific Structures within $Fe_3O_4|\gamma$-Mn_2O_3 Core|Shell Nanoparticles Using Anomalous Small-Angle X-ray Scattering. *ACS Nano* **2013**, *7*, 921−931.
(122) Haug, J.; Kruth, H.; Dubiel, M.; Hofmeister, H.; Haas, S.; Tatchev, D.; Hoell, A. ASAXS Study on the Formation of Core−Shell Ag/Au Nanoparticles in Glass. *Nanotechnology* **2009**, *20*, 505705.
(123) Kluthe, C.; Al-Kassab, T.; Barker, J.; Pyckhout-Hintzen, W.; Kirchheim, R. Segregation of Hydrogen at Internal Ag/MgO (Metal/Oxide)-Interfaces as Observed by Small Angle Neutron Scattering. *Acta Mater.* **2004**, *52*, 2701−2710.
(124) Yu, C.; Koh, S.; Leisch, J. E.; Toney, M. F.; Strasser, P. Size and Composition Distribution Dynamics of Alloy Nanoparticle Eectrocatalysts Probed by Anomalous Small Angle X-ray Scattering (ASAXS). *Faraday Discuss.* **2009**, *140*, 283−296.
(125) Strasser, P.; Koh, S.; Anniyev, T.; Greeley, J.; More, K.; Yu, C.; Liu, Z.; Kaya, S.; Nordlund, D.; Ogasawara, H.; et al. Lattice-Strain Control of the Activity in Dealloyed Core−Shell Fuel Cell Catalysts. *Nat. Chem.* **2010**, *2*, 454−460.
(126) Farrow, C. L.; Shi, C.; Juhas, P.; Peng, X.; Billinge, S. J. L. Robust Structure and Morphology Parameters for CdS Nanoparticles by Combining Small-Angle X-ray Scattering and Atomic Pair Distribution Function Data in A Complex Modeling Framework. *J. Appl. Crystallogr.* **2014**, *47*, 561−565.
(127) Petkov, V. In *Characterization of Materials*; John Wiley & Sons, Inc.: 2012.
(128) Farrow, C. L.; Billinge, S. J. L. Relationship between the Atomic Pair Distribution Function and Small-Angle Scattering: Implications for Modeling of Nanoparticles. *Acta Crystallogr., Sect. A: Found. Crystallogr.* **2009**, *65*, 232−239.
(129) Radha, B.; Senesi, A. J.; O'Brien, M. N.; Wang, M. X.; Auyeung, E.; Lee, B.; Mirkin, C. A. Reconstitutable Nanoparticle Superlattices. *Nano Lett.* **2014**, *14*, 2162−2167.
(130) Ornstein, L. S.; Zernike, F. Accidental Derivations of Density and Opalescence at the Critical Point of A Single Substance. *Proc. Acad. Sci. Amsterdam* **1914**, *17*, 793.
(131) Lebowitz, J. L.; Percus, J. K. Mean Spherical Model for Lattice Gases with Extended Hard Cores and Continuum Fluids. *Phys. Rev.* **1966**, *144*, 251−258.
(132) Høye, J. S.; Blum, L. Solution of the Yukawa Closure of the Ornstein-Zernike Equation. *J. Stat. Phys.* **1977**, *16*, 399−413.
(133) Liu, Y.; Chen, W.-R.; Chen, S.-H. Cluster Formation in Two-Yukawa Fluids. *J. Chem. Phys.* **2005**, *122*, 044507.
(134) Liu, Y.; Fratini, E.; Baglioni, P.; Chen, W.-R.; Chen, S.-H. Effective Long-Range Attraction between Protein Molecules in Solutions Studied by Small Angle Neutron Scattering. *Phys. Rev. Lett.* **2005**, *95*, 118102.
(135) Kinning, D. J.; Thomas, E. L. Hard-Sphere Interactions between Spherical Domains in Diblock Copolymers. *Macromolecules* **1984**, *17*, 1712−1718.
(136) Wertheim, M. S. Exact Solution of the Percus-Yevick Integral Equation for Hard Spheres. *Phys. Rev. Lett.* **1963**, *10*, 321−323.
(137) Baxter, R. J. Percus−Yevick Equation for Hard Spheres with Surface Adhesion. *J. Chem. Phys.* **1968**, *49*, 2770−2774.
(138) Robertus, C.; Philipse, W. H.; Joosten, J. G. H.; Levine, Y. K. Solution of the Percus−Yevick Approximation of the Multicomponent Adhesive Spheres System Applied to the Small Angle X-ray Scattering from Microemulsions. *J. Chem. Phys.* **1989**, *90*, 4482−4490.
(139) De Kruif, C. G.; Rouw, P. W.; Briels, W. J.; Duits, M. H. G.; Vrij, A.; May, R. P. Adhesive Hard-Sphere Colloidal Dispersions. A Small-Angle Neutron-Scattering Study of Stickiness and the Structure Factor. *Langmuir* **1989**, *5*, 422−428.
(140) Mendez-Alcaraz, J. M.; D'Aguanno, B.; Klein, R. Structure of Binary Colloidal Mixtures of Charged and Uncharged Spherical Particles. *Langmuir* **1992**, *8*, 2913−2920.
(141) Narayanan, T. In *Applications of Synchrotron Light to Scattering and Diffraction in Materials and Life Sciences*; Gomez, M., Nogales, A., Garcia-Gutierrez, M. C., Ezquerra, T. A., Eds.; Lecture Notes in Physics 776; Springer: Berlin, 2009.
(142) Crocker, J. C.; Grier, D. G. Microscopic Measurement of the Pair Interaction Potential of Charge-Stabilized Colloid. *Phys. Rev. Lett.* **1994**, *73*, 352−355.
(143) Korgel, B. A.; Fitzmaurice, D. Small-Angle X-ray-Scattering Study of Silver-Nanocrystal Disorder-Order Phase Transitions. *Phys. Rev. B: Condens. Matter Mater. Phys.* **1999**, *59*, 14191−14201.
(144) Baeza, G. P.; Genix, A.-C.; Degrandcourt, C.; Petitjean, L.; Gummel, J.; Couty, M.; Oberdisse, J. Multiscale Filler Structure in Simplified Industrial Nanocomposite Silica/SBR Systems Studied by SAXS and TEM. *Macromolecules* **2013**, *46*, 317−329.
(145) Matsuoka, H.; Tanaka, H.; Hashimoto, T.; Ise, N. Elastic Scattering from Cubic Lattice Systems with Paracrystalline Distortion. *Phys. Rev. B: Condens. Matter Mater. Phys.* **1987**, *36*, 1754−1765.
(146) Matsuoka, H.; Tanaka, H.; Iizuka, N.; Hashimoto, T.; Ise, N. Elastic Scattering from Cubic Lattice Systems with Paracrystalline Distortion. II. *Phys. Rev. B: Condens. Matter Mater. Phys.* **1990**, *41*, 3854−3856.
(147) Abbas, S.; Lodge, T. P. Superlattice Formation in a Binary Mixture of Block Copolymer Micelles. *Phys. Rev. Lett.* **2006**, *97*, 097803.
(148) Turner, D. C.; Gruner, S. M. X-ray Diffraction Reconstruction of the Inverted Hexagonal (HII) Phase in Lipid-Water Systems. *Biochemistry* **1992**, *31*, 1340−1355.
(149) Lee, B.; Park, I.; Yoon, J.; Park, S.; Kim, J.; Kim, K.-W.; Chang, T.; Ree, M. Structural Analysis of Block Copolymer Thin Films with Grazing Incidence Small-Angle X-ray Scattering. *Macromolecules* **2005**, *38*, 4311−4323.
(150) Toombes, G. E. S.; Finnefrock, A. C.; Tate, M. W.; Ulrich, R.; Wiesner, U.; Gruner, S. M. A Re-Evaluation of the Morphology of a Bicontinuous Block Copolymer−Ceramic Material. *Macromolecules* **2007**, *40*, 8974−8982.
(151) Wang, W.; Pan, D.; Song, Y.; Liu, W.; Yang, L.; Huang, H. W. Method of X-Ray Anomalous Diffraction for Lipid Structures. *Biophys. J.* **2006**, *91*, 736−743.
(152) Lee, B.; Park, I.; Park, H.; Lo, C.-T.; Chang, T.; Winans, R. E. Electron Eensity Map using Multiple Scattering in Grazing-Incidence Small-Angle X-ray Scattering. *J. Appl. Crystallogr.* **2007**, *40*, 496−504.
(153) Zeng, X.; Kieffer, R.; Glettner, B.; Nürnberger, C.; Liu, F.; Pelz, K.; Prehm, M.; Baumeister, U.; Hahn, H.; Lang, H.; et al. Complex Multicolor Tilings and Critical Phenomena in Tetraphilic Liquid Crystals. *Science* **2011**, *331*, 1302−1306.
(154) Pan, D.; Wang, W.; Liu, W.; Yang, L.; Huang, H. W. Chain Packing in the Inverted Hexagonal Phase of Phospholipids: A Study by X-ray Anomalous Diffraction on Bromine-labeled Chains. *J. Am. Chem. Soc.* **2006**, *128*, 3800−3807.
(155) Yuan, P.; Sun, J.; Xu, H.; Zhou, L.; Liu, J.; Zhang, D.; Wang, Y.; Jack, K. S.; Drennan, J.; Zhao, D.; et al. Extensive Inspection of an Unconventional Mesoporous Silica Material at All Length-Scales. *Chem. Mater.* **2011**, *23*, 229−238.
(156) Perroni, D. V.; Mahanthappa, M. K. Inverse Pm3n Cubic Micellar Lyotropic Phases from Zwitterionic Triazolium Gemini Surfactants. *Soft Matter* **2013**, *9*, 7919−7922.
(157) Vonk, C. Investigation of Non-Ideal Two-Phase Polymer Structures by Small-Angle X-ray Scattering. *J. Appl. Crystallogr.* **1973**, *6*, 81−86.
(158) Shibayama, M.; Hashimoto, T. Small-Angle X-ray Scattering Analyses of Lamellar Microdomains Based on A Model of One-Dimensional Paracrystal with Uniaxial Orientation. *Macromolecules* **1986**, *19*, 740−749.
(159) Jones, M. R.; Macfarlane, R. J.; Lee, B.; Zhang, J.; Young, K. L.; Senesi, A. J.; Mirkin, C. A. DNA-Nanoparticle Superlattices Formed from Anisotropic Building Blocks. *Nat. Mater.* **2010**, *9*, 913−917.
(160) Macfarlane, R. J.; Jones, M. R.; Lee, B.; Auyeung, E.; Mirkin, C. A. Topotactic Interconversion of Nanoparticle Superlattices. *Science* **2013**, *341*, 1222−1225.
(161) O'Brien, M. N.; Jones, M. R.; Lee, B.; Mirkin, C. A. Anisotropic Nanoparticle Complementarity in DNA-mediated Co-crystallization. *Nat. Mater.* **2015**, *14*, 833−839.

DOI: 10.1021/acs.chemrev.5b00690
Chem. Rev. XXXX, XXX, XXX−XXX

(162) Yager, K. G.; Zhang, Y.; Lu, F.; Gang, O. Periodic Lattices of Arbitrary Nano-Objects: Modeling and Applications for Self-Assembled Systems. *J. Appl. Crystallogr.* **2014**, *47*, 118−129.
(163) Kaler, E. In *Modern Aspects of Small-Angle Scattering*; Brumberger, H., Ed.; Springer: Dordrecht, Netherlands, 1995; Vol. *451*.
(164) Lazzari, R.; Renaud, G.; Jupille, J.; Leroy, F. Self-Similarity during Growth of the Au/TiO2(110) Model Catalyst as Seen by the Scattering of X-rays at Grazing-Angle Incidence. *Phys. Rev. B: Condens. Matter Mater. Phys.* **2007**, *76*, 125412.
(165) Buljan, M.; Radic, N.; Bernstorff, S.; Drazic, G.; Bogdanovic-Radovic, I.; Holy, V. Grazing-Incidence Small-Angle X-ray Scattering: Application to the Study of Quantum Dot Lattices. *Acta Crystallogr., Sect. A: Found. Crystallogr.* **2012**, *68*, 124−138.
(166) Smilgies, D.-M.; Heitsch, A. T.; Korgel, B. A. Stacking of Hexagonal Nanocrystal Layers during Langmuir−Blodgett Deposition. *J. Phys. Chem. B* **2012**, *116*, 6017−6026.
(167) Choi, J. J.; Bian, K.; Baumgardner, W. J.; Smilgies, D.-M.; Hanrath, T. Interface-Induced Nucleation, Orientational Alignment and Symmetry Transformations in Nanocube Superlattices. *Nano Lett.* **2012**, *12*, 4791−4798.
(168) Senesi, A. J.; Eichelsdoerfer, D. J.; Macfarlane, R. J.; Jones, M. R.; Auyeung, E.; Lee, B.; Mirkin, C. A. Stepwise Evolution of DNA-Programmable Nanoparticle Superlattices. *Angew. Chem., Int. Ed.* **2013**, *52*, 6624−6628.
(169) Jin, S.; Yoon, J.; Heo, K.; Park, H.-W.; Kim, J.; Kim, K.-W.; Shin, T. J.; Chang, T.; Ree, M. Detailed Analysis of Gyroid Structures in Diblock Copolymer Thin Films with Synchrotron Grazing-Incidence X-ray Scattering. *J. Appl. Crystallogr.* **2007**, *40*, 950−958.
(170) Heo, K.; Yoon, J.; Jin, S.; Kim, J.; Kim, K.-W.; Shin, T. J.; Chung, B.; Chang, T.; Ree, M. Polystyrene-b-Polyisoprene Thin Films with Hexagonally Perforated Layer Structure: Quantitative Grazing-Incidence X-ray Scattering Analysis. *J. Appl. Crystallogr.* **2008**, *41*, 281−291.
(171) David, W. I. F.; Shankland, K.; McCusker, L. B.; Barlocher, C. *Structure Determination from Powder Diffraction Data*; Oxford University Press: Oxford, U.K., 2006.
(172) Simon, P.; Rosseeva, E.; Baburin, I. A.; Liebscher, L.; Hickey, S. G.; Cardoso-Gil, R.; Eychmüller, A.; Kniep, R.; Carrillo-Cabrera, W. PbS−Organic Mesocrystals: The Relationship between Nanocrystal Orientation and Superlattice Array. *Angew. Chem., Int. Ed.* **2012**, *51*, 10776−10781.
(173) Li, R.; Bian, K.; Wang, Y.; Xu, H.; Hollingsworth, J. A.; Hanrath, T.; Fang, J.; Wang, Z. An Obtuse Rhombohedral Superlattice Assembled by Pt Nanocubes. *Nano Lett.* **2015**, *15*, 6254.
(174) Tate, M. P.; Urade, V. N.; Kowalski, J. D.; Wei, T.-c.; Hamilton, B. D.; Eggiman, B. W.; Hillhouse, H. W. Simulation and Interpretation of 2D Diffraction Patterns from Self-Assembled Nanostructured Films at Arbitrary Angles of Incidence: From Grazing Incidence (Above the Critical Angle) to Transmission Perpendicular to the Substrate. *J. Phys. Chem. B* **2006**, *110*, 9882−9892.
(175) Breiby, D. W.; Bunk, O.; Andreasen, J. W.; Lemke, H. T.; Nielsen, M. M. Simulating X-ray Diffraction of Textured Films. *J. Appl. Crystallogr.* **2008**, *41*, 262−271.
(176) Snyder, R. L.; Fiala, J.; Bunge, B. J. *Defect and Microstructure Analysis by Diffraction*; Oxford University Press: Oxford, U.K., 1999.
(177) Stokes, A. R.; Wilson, A. J. C. The Diffraction of X rays by Distorted Crystal Aggregates - I. *Proc. Phys. Soc.* **1944**, *56*, 174.
(178) Williamson, G. K.; Hall, W. H. X-ray Line Broadening from Filed Aluminium and Wolfram. *Acta Metall.* **1953**, *1*, 22−31.
(179) Warren, B. E.; Averbach, B. L. The Effect of Cold-Work Distortion on X-Ray Patterns. *J. Appl. Phys.* **1950**, *21*, 595−599.
(180) Mittemeijer, E. J.; Welzel, U. The "State of the Art" of the Diffraction Analysis of Crystallite Size and Lattice Strain. *Z. Kristallogr.* **2008**, *223*, 552.
(181) Weidenthaler, C. Pitfalls in the Characterization of Nanoporous and Nanosized Materials. *Nanoscale* **2011**, *3*, 792.
(182) Cui, H.; Pashuck, E. T.; Velichko, Y. S.; Weigand, S. J.; Cheetham, A. G.; Newcomb, C. J.; Stupp, S. I. Spontaneous and X-ray−Triggered Crystallization at Long Range in Self-Assembling Filament Networks. *Science* **2010**, *327*, 555−559.
(183) Dalmaschio, C. J.; da Silveira Firmiano, E. G.; Pinheiro, A. N.; Sobrinho, D. G.; Farias de Moura, A.; Leite, E. R. Nanocrystals Self-Assembled in Superlattices Directed by the Solvent-Organic Capping Interaction. *Nanoscale* **2013**, *5*, 5602−5610.
(184) Sulyanova, E. A.; Shabalin, A.; Zozulya, A. V.; Meijer, J.-M.; Dzhigaev, D.; Gorobtsov, O.; Kurta, R. P.; Lazarev, S.; Lorenz, U.; Singer, A.; et al. Structural Evolution of Colloidal Crystal Films in the Process of Melting Revealed by Bragg Peak Analysis. *Langmuir* **2015**, *31*, 5274−5283.
(185) Lu, Z.; Yin, Y. Colloidal Nanoparticle Clusters: Functional Materials by Design. *Chem. Soc. Rev.* **2012**, *41*, 6874−6887.
(186) Wang, T.; LaMontagne, D.; Lynch, J.; Zhuang, J.; Cao, Y. C. Colloidal Superparticles from Nanoparticle Assembly. *Chem. Soc. Rev.* **2013**, *42*, 2804−2823.
(187) de Nijs, B.; Dussi, S.; Smallenburg, F.; Meeldijk, J. D.; Groenendijk, D. J.; Filion, L.; Imhof, A.; van Blaaderen, A.; Dijkstra, M. Entropy-Driven Formation of Large Icosahedral Colloidal Clusters by Spherical Confinement. *Nat. Mater.* **2015**, *14*, 56−60.
(188) Chen, O.; Riedemann, L.; Etoc, F.; Herrmann, H.; Coppey, M.; Barch, M.; Farrar, C. T.; Zhao, J.; Bruns, O. T.; Wei, H. Magneto-Fluorescent Core-Shell Supernanoparticles. *Nat. Commun.* **2014**, *5*, 5093.
(189) Wang, T.; Zhuang, J.; Lynch, J.; Chen, O.; Wang, Z.; Wang, X.; LaMontagne, D.; Wu, H.; Wang, Z.; Cao, Y. C. Self-Assembled Colloidal Superparticles from Nanorods. *Science* **2012**, *338*, 358−363.
(190) Xia, Y.; Nguyen, T. D.; Yang, M.; Lee, B.; Santos, A.; Podsiadlo, P.; Tang, Z.; Glotzer, S. C.; Kotov, N. A. Self-Assembly of Self-Limiting Monodisperse Supraparticles from Polydisperse Nanoparticles. *Nat. Nanotechnol.* **2011**, *6*, 580−587.
(191) Tanaka, H.; Koizumi, S.; Hashimoto, T.; Itoh, H.; Satoh, M.; Naka, K.; Chujo, Y. Combined in Situ and Time-Resolved SANS and SAXS Studies of Chemical Reactions at Specific Sites and Self-Assembling Processes of Reaction Products: Reduction of Palladium Ions in Self-Assembled Polyamidoamine Dendrimers as A Template. *Macromolecules* **2007**, *40*, 4327−4337.
(192) Jin, R. Quantum Sized, Thiolate-Protected Gold Nanoclusters. *Nanoscale* **2010**, *2*, 343−362.
(193) Fleury, B.; Cortes-Huerto, R.; Taché, O.; Testard, F.; Menguy, N.; Spalla, O. Gold Nanoparticle Internal Structure and Symmetry Probed by Unified Small-Angle X-ray Scattering and X-ray Diffraction Coupled with Molecular Dynamics Analysis. *Nano Lett.* **2015**, *15*, 6088−6094.
(194) Jadzinsky, P. D.; Calero, G.; Ackerson, C. J.; Bushnell, D. A.; Kornberg, R. D. Structure of a Thiol Monolayer-Protected Gold Nanoparticle at 1.1 Å Resolution. *Science* **2007**, *318*, 430−433.
(195) Rupich, S. M.; Shevchenko, E. V.; Bodnarchuk, M. I.; Lee, B.; Talapin, D. V. Size-Dependent Multiple Twinning in Nanocrystal Superlattices. *J. Am. Chem. Soc.* **2010**, *132*, 289−296.
(196) Zhuang, J.; Wu, H.; Yang, Y.; Cao, Y. C. Supercrystalline Colloidal Particles from Artificial Atoms. *J. Am. Chem. Soc.* **2007**, *129*, 14166−14167.
(197) Nagaoka, Y.; Chen, O.; Wang, Z.; Cao, Y. C. Structural Control of Nanocrystal Superlattices Using Organic Guest Molecules. *J. Am. Chem. Soc.* **2012**, *134*, 2868−2871.
(198) Zhuang, J.; Shaller, A. D.; Lynch, J.; Wu, H.; Chen, O.; Li, A. D. Q.; Cao, Y. C. Cylindrical Superparticles from Semiconductor Nanorods. *J. Am. Chem. Soc.* **2009**, *131*, 6084−6085.
(199) Wang, T.; Wang, X.; LaMontagne, D.; Wang, Z.; Wang, Z.; Cao, Y. C. Shape-Controlled Synthesis of Colloidal Superparticles from Nanocubes. *J. Am. Chem. Soc.* **2012**, *134*, 18225−18228.
(200) Balmer, J. A.; Mykhaylyk, O. O.; Schmid, A.; Armes, S. P.; Fairclough, J. P. A.; Ryan, A. J. Characterization of Polymer-Silica Nanocomposite Particles with Core−Shell Morphologies using Monte Carlo Simulations and Small Angle X-ray Scattering. *Langmuir* **2011**, *27*, 8075−8089.
(201) Chen, Z. H.; Kim, C.; Zeng, X.-b.; Hwang, S. H.; Jang, J.; Ungar, G. Characterizing Size and Porosity of Hollow Nanoparticles:

DOI: 10.1021/acs.chemrev.5b00690
Chem. Rev. XXXX, XXX, XXX−XXX

SAXS, SANS, TEM, DLS, and Adsorption Isotherms Compared. *Langmuir* **2012**, *28*, 15350−15361.
(202) Goergen, S.; Yin, C.; Yang, M.; Lee, B.; Lee, S.; Wang, C.; Wu, P.; Boucher, M. B.; Kwon, G.; Seifert, S.; et al. Structure Sensitivity of Oxidative Dehydrogenation of Cyclohexane over FeO_x and Au/Fe_3O_4 Nanocrystals. *ACS Catal.* **2013**, *3*, 529−539.
(203) Christensen, S. T.; Elam, J. W.; Rabuffetti, F. A.; Ma, Q.; Weigand, S. J.; Lee, B.; Seifert, S.; Stair, P. C.; Poeppelmeier, K. R.; Hersam, M. C.; et al. Controlled Growth of Platinum Nanoparticles on Strontium Titanate Nanocubes by Atomic Layer Deposition. *Small* **2009**, *5*, 750−757.
(204) Li, T.; Niu, Z.; Emrick, T.; Russell, T. P.; Wang, Q. Core/Shell Biocomposites from the Hierarchical Assembly of Bionanoparticles and Polymer. *Small* **2008**, *4*, 1624−1629.
(205) Li, T.; Ye, B.; Niu, Z.; Thompson, P.; Seifert, S.; Lee, B.; Wang, Q. Closed-Packed Colloidal Assemblies from Icosahedral Plant Virus and Polymer. *Chem. Mater.* **2009**, *21*, 1046−1050.
(206) Li, T.; Wu, L.; Suthiwangcharoen, N.; Bruckman, M. A.; Cash, D.; Hudson, J. S.; Ghoshroy, S.; Wang, Q. Controlled Assembly of Rodlike Vruses with Polymers. *Chem. Commun.* **2009**, 2869−2871.
(207) Suthiwangcharoen, N.; Li, T.; Wu, L.; Reno, H. B.; Thompson, P.; Wang, Q. Facile Co-Assembly Process to Generate Core−Shell Nanoparticles with Functional Protein Corona. *Biomacromolecules* **2014**, *15*, 948−956.
(208) Lu, J.; Fu, B.; Kung, M. C.; Xiao, G.; Elam, J. W.; Kung, H. H.; Stair, P. C. Coking- and Sintering-Resistant Palladium Catalysts Achieved Through Atomic Layer Deposition. *Science* **2012**, *335*, 1205−1208.
(209) Spalla, O.; Lyonnard, S.; Testard, F. Analysis of the Small-Angle Intensity Scattered by a Porous and Granular Medium. *J. Appl. Crystallogr.* **2003**, *36*, 338−347.
(210) Chavez Panduro, E. A.; Beuvier, T.; Fernandez Martinez, M.; Hassani, L.; Calvignac, B.; Boury, F.; Gibaud, A. Small-Angle X-ray Scattering Analysis of Porous Powders of $CaCO_3$. *J. Appl. Crystallogr.* **2012**, *45*, 881−889.
(211) Hollamby, M. J.; Borisova, D.; Brown, P.; Eastoe, J.; Grillo, I.; Shchukin, D. Growth of Mesoporous Silica Nanoparticles Monitored by Time-Resolved Small-Angle Neutron Scattering. *Langmuir* **2012**, *28*, 4425−4433.
(212) Martin, J. E.; Hurd, A. J. Scattering from Fractals. *J. Appl. Crystallogr.* **1987**, *20*, 61−78.
(213) Pfeifer, P.; Ehrburger-Dolle, F.; Rieker, T. P.; González, M. T.; Hoffman, W. P.; Molina-Sabio, M.; Rodríguez-Reinoso, F.; Schmidt, P. W.; Voss, D. J. Nearly Space-Filling Fractal Networks of Carbon Nanopores. *Phys. Rev. Lett.* **2002**, *88*, 115502.
(214) Eggersdorfer, M. L.; Pratsinis, S. E. The Structure of Agglomerates Consisting of Polydisperse Particles. *Aerosol Sci. Technol.* **2012**, *46*, 347−353.
(215) Besselink, R.; ten Elshof, J. E. Mass-Fractal Growth in Niobia/Silsesquioxane Mixtures: A Small-Angle X-ray Scattering Study. *J. Appl. Crystallogr.* **2014**, *47*, 1606−1613.
(216) Zucchi, I. A.; Hoppe, C. E.; Galante, M. J.; Williams, R. J. J.; López-Quintela, M. A.; Matějka, L.; Slouf, M.; Pleštil, J. Self-Assembly of Gold Nanoparticles as Colloidal Crystals Induced by Polymerization of Amphiphilic Monomers. *Macromolecules* **2008**, *41*, 4895−4903.
(217) Schaefer, D. W.; Martin, J. E.; Wiltzius, P.; Cannell, D. S. Fractal Geometry of Colloidal Aggregates. *Phys. Rev. Lett.* **1984**, *52*, 2371−2374.
(218) Schaefer, D. W.; Rieker, T.; Agamalian, M.; Lin, J. S.; Fischer, D.; Sukumaran, S.; Chen, C.; Beaucage, G.; Herd, C.; Ivie, J. Multilevel Structure of Reinforcing Silica and Carbon. *J. Appl. Crystallogr.* **2000**, *33*, 587−591.
(219) Bale, H. D.; Schmidt, P. W. Small-Angle X-Ray-Scattering Investigation of Submicroscopic Porosity with Fractal Properties. *Phys. Rev. Lett.* **1984**, *53*, 596−599.
(220) Teixeira, J. Small-Angle Scattering by Fractal Systems. *J. Appl. Crystallogr.* **1988**, *21*, 781−785.
(221) Lin, Y.-C.; Chen, C.-Y.; Chen, H.-L.; Hashimoto, T.; Chen, S.-A.; Li, Y.-C. Hierarchical Self-assembly of Nanoparticles in Polymer Matrix and the Nature of the Interparticle Interaction. *J. Chem. Phys.* **2015**, *142*, 214905.
(222) Robbes, A.-S.; Jestin, J.; Meneau, F.; Dalmas, F.; Sandre, O.; Perez, J.; Boué, F.; Cousin, F. Homogeneous Dispersion of Magnetic Nanoparticles Aggregates in a PS Nanocomposite: Highly Reproducible Hierarchical Structure Tuned by the Nanoparticles' Size. *Macromolecules* **2010**, *43*, 5785−5796.
(223) Wang, J.; Winans, R. E.; Anderson, S. L.; Seifert, S.; Lee, B.; Chupas, P. J.; Ren, Y.; Lee, S.; Liu, Y. In Situ Small-Angle X-ray Scattering from Pd Nanoparticles Formed by Thermal Decomposition of Organo-Pd Catalyst Precursors Dissolved in Hydrocarbons. *J. Phys. Chem. C* **2013**, *117*, 22627−22635.
(224) Stribeck, N. *X-Ray Scattering of Soft Matter*; Springer: Berlin, 2007.
(225) Semenyuk, A. V.; Svergun, D. I. GNOM - A Program Package for Small-Angle Scattering Data Processing. *J. Appl. Crystallogr.* **1991**, *24*, 537−540.
(226) Fritz, G.; Bergmann, A. Interpretation of Small-Angle Scattering Data of Inhomogeneous Ellipsoids. *J. Appl. Crystallogr.* **2004**, *37*, 815−822.
(227) Glatter, O. A New Method for the Evaluation of Small-Angle Scattering Data. *J. Appl. Crystallogr.* **1977**, *10*, 415−421.
(228) Glatter, O. The Interpretation of Real-Space Information from Small-Angle Scattering Experiments. *J. Appl. Crystallogr.* **1979**, *12*, 166−175.
(229) Buchkremer, A.; Linn, M. J.; Timper, J. U.; Eckert, T.; Mayer, J.; Richtering, W.; von Plessen, G.; Simon, U. Synthesis and Internal Structure of Finite-Size DNA−Gold Nanoparticle Assemblies. *J. Phys. Chem. C* **2014**, *118*, 7174−7184.
(230) Yin, P.; Li, T.; Forgan, R. S.; Lydon, C.; Zuo, X.; Zheng, Z. N.; Lee, B.; Long, D.; Cronin, L.; Liu, T. Exploring the Programmable Assembly of A Polyoxometalate−Organic Hybrid via Metal Ion Coordination. *J. Am. Chem. Soc.* **2013**, *135*, 13425−13432.
(231) Tiede, D. M.; Mardis, K. L.; Zuo, X. X-ray Scattering Combined with Coordinate-Based Analyses for Applications in Natural and Artificial Photosynthesis. *Photosynth. Res.* **2009**, *102*, 267−279.
(232) Hua, X.; Liu, Z.; Bruce, P. G.; Grey, C. P. The Morphology of TiO_2 (B) Nanoparticles. *J. Am. Chem. Soc.* **2015**, *137*, 13612−13623.
(233) Kodama, K.; Iikubo, S.; Taguchi, T.; Shamoto, S.-i. Finite Size Effects of Nanoparticles on the Atomic Pair Distribution Functions. *Acta Crystallogr., Sect. A: Found. Crystallogr.* **2006**, *62*, 444−453.
(234) Howell, R. C.; Proffen, T.; Conradson, S. D. Pair Distribution Function and Structure Factor of Spherical Particles. *Phys. Rev. B: Condens. Matter Mater. Phys.* **2006**, *73*, 094107.
(235) Gilbert, B. Finite Size Effects on the Real-Space Pair Distribution Function of Nanoparticles. *J. Appl. Crystallogr.* **2008**, *41*, 554−562.
(236) Gagin, A.; Allen, A. J.; Levin, I. Combined Fitting of Small- and Wide-Angle X-ray Total Scattering Data from Nanoparticles: Benefits and Issues. *J. Appl. Crystallogr.* **2014**, *47*, 619−629.
(237) Pichler, S.; Bodnarchuk, M. I.; Kovalenko, M. V.; Yarema, M.; Springholz, G.; Talapin, D. V.; Heiss, W. Evaluation of Ordering in Single-Component and Binary Nanocrystal Superlattices by Analysis of Their Autocorrelation Functions. *ACS Nano* **2011**, *5*, 1703−1712.
(238) Stein, G. E.; Kramer, E. J.; Li, X.; Wang, J. Single-Crystal Diffraction from Two-Dimensional Block Copolymer Arrays. *Phys. Rev. Lett.* **2007**, *98*, 086101.
(239) Stein, G. E.; Lee, W. B.; Fredrickson, G. H.; Kramer, E. J.; Li, X.; Wang, J. Thickness Dependent Ordering in Laterally Confined Monolayers of Spherical-Domain Block Copolymers. *Macromolecules* **2007**, *40*, 5791−5800.
(240) Jiang, Z.; Lin, X.-M.; Sprung, M.; Narayanan, S.; Wang, J. Capturing the Crystalline Phase of Two-Dimensional Nanocrystal Superlattices in Action. *Nano Lett.* **2010**, *10*, 799−803.
(241) Marcus, A. H.; Rice, S. A. Observations of First-Order Liquid-to-Hexatic and Hexatic-to-Solid Phase Transitions in A Confined Colloid Suspension. *Phys. Rev. Lett.* **1996**, *77*, 2577−2580.

DOI: 10.1021/acs.chemrev.5b00690
Chem. Rev. XXXX, XXX, XXX−XXX

(242) Kapfer, S. C.; Krauth, W. Two-Dimensional Melting: From Liquid-Hexatic Coexistence to Continuous Transitions. *Phys. Rev. Lett.* **2015**, *114*, 035702.
(243) Aeppli, G.; Bruinsma, R. Hexatic Order and Liquid Density Fluctuations. *Phys. Rev. Lett.* **1984**, *53*, 2133−2136.
(244) Sorensen, C. M.; Wang, G. M. Size Distribution Effect on the Power Law Regime of the Structure Factor of Fractal Aggregates. *Phys. Rev. E: Stat. Phys., Plasmas, Fluids, Relat. Interdiscip. Top.* **1999**, *60*, 7143−7148.
(245) Teubner, M.; Strey, R. Origin of the Scattering Peak in Microemulsions. *J. Chem. Phys.* **1987**, *87*, 3195−3200.
(246) Li, W.; Ryan, A. J.; Meier, I. K. Morphology Development via Reaction-Induced Phase Separation in Flexible Polyurethane Foam. *Macromolecules* **2002**, *35*, 5034−5042.
(247) Hillmyer, M. A.; Maurer, W. W.; Lodge, T. P.; Bates, F. S.; Almdal, K. Model Bicontinuous Microemulsions in Ternary Homopolymer/Block Copolymer Blends. *J. Phys. Chem. B* **1999**, *103*, 4814−4824.
(248) Debye, P. Zerstreuung Von Röntgenstrahlen. *Ann. Phys.* **1915**, *351*, 809−823.
(249) Gumerov, N. A.; Berlin, K.; Fushman, D.; Duraiswami, R. A Hierarchical Algorithm for Fast Debye Summation with Applications to Small Angle Scattering. *J. Comput. Chem.* **2012**, *33*, 1981−1996.
(250) Olds, D. P.; Duxbury, P. M. Efficient Algorithms for Calculating Small-Angle Scattering from Large Model Structures. *J. Appl. Crystallogr.* **2014**, *47*, 1077−1086.
(251) Schmidt-Rohr, K. Simulation of Small-Angle Scattering Curves by Numerical Fourier Transformation. *J. Appl. Crystallogr.* **2007**, *40*, 16−25.
(252) Pantos, E.; van Garderen, H. F.; Hilbers, P. A. J.; Beelen, T. P. M.; van Santen, R. A. Simulation of Small-Angle Scattering from Large Assemblies of Multi-type Scatterer Particles. *J. Mol. Struct.* **1996**, *383*, 303−308.
(253) Bardhan, J.; Park, S.; Makowski, L. SoftWAXS: A Computational Tool for Modeling Wide-Angle X-ray Solution Scattering from Biomolecules. *J. Appl. Crystallogr.* **2009**, *42*, 932−943.
(254) Cervellino, A.; Giannini, C.; Guagliardi, A. On the Efficient Evaluation of Fourier Patterns for Nanoparticles and Clusters. *J. Comput. Chem.* **2006**, *27*, 995−1008.
(255) Ozturk, H.; Yan, H.; Hill, J. P.; Noyan, I. C. Sampling Statistics of Diffraction from Nanoparticle Powder Aggregates. *J. Appl. Crystallogr.* **2014**, *47*, 1016−1025.
(256) Vogel, W.; Rosner, B.; Tesche, B. Structural Investigations of Gold (Au_{55}) Organometallic Complexes by X-ray Powder Diffraction and Transmission Electron Microscopy. *J. Phys. Chem.* **1993**, *97*, 11611−11616.
(257) Chiche, D.; Digne, M.; Revel, R.; Chanéac, C.; Jolivet, J.-P. Accurate Determination of Oxide Nanoparticle Size and Shape Based on X-Ray Powder Pattern Simulation: Application to Boehmite AlOOH. *J. Phys. Chem. C* **2008**, *112*, 8524−8533.
(258) Renaud, G.; Lazzari, R.; Revenant, C.; Barbier, A.; Noblet, M.; Ulrich, O.; Leroy, F.; Jupille, J.; Borensztein, Y.; Henry, C. R.; et al. Real-Time Monitoring of Growing Nanoparticles. *Science* **2003**, *300*, 1416−1419.
(259) Molina, L. M.; Lee, S.; Sell, K.; Barcaro, G.; Fortunelli, A.; Lee, B.; Seifert, S.; Winans, R. E.; Elam, J. W.; Pellin, M. J.; et al. Size-dependent Selectivity and Activity of Silver Nanoclusters in the Partial Oxidation of Propylene to Propylene Oxide and Acrolein: A Joint Experimental and Theoretical Study. *Catal. Today* **2011**, *160*, 116−130.
(260) Stein, G. E.; Kramer, E. J.; Li, X.; Wang, J. Layering Transitions in Thin Films of Spherical-Domain Block Copolymers. *Macromolecules* **2007**, *40*, 2453−2460.
(261) Chang, S.-L. Solution to the X-ray Phase Problem Using Multiple Diffraction—A Review. *Crystallogr. Rev.* **1987**, *1*, 87−184.
(262) Hanrath, T.; Choi, J. J.; Smilgies, D.-M. Structure/Processing Relationships of Highly Ordered Lead Salt Nanocrystal Superlattices. *ACS Nano* **2009**, *3*, 2975−2988.
(263) Ahn, H.; Shin, C.; Lee, B.; Ryu, D. Y. Phase Transitions of Block Copolymer Film on Homopolymer-Grafted Substrate. *Macromolecules* **2010**, *43*, 1958−1963.
(264) Lu, C.; Akey, A. J.; Dahlman, C. J.; Zhang, D.; Herman, I. P. Resolving the Growth of 3D Colloidal Nanoparticle Superlattices by Real-Time Small-Angle X-ray Scattering. *J. Am. Chem. Soc.* **2012**, *134*, 18732−18738.
(265) Zhang, J.; Luo, Z.; Martens, B.; Quan, Z.; Kumbhar, A.; Porter, N.; Wang, Y.; Smilgies, D.-M.; Fang, J. Reversible Kirkwood−Alder Transition Observed in Pt_3Cu_2 Nanoctahedron Assemblies under Controlled Solvent Annealing/Drying Conditions. *J. Am. Chem. Soc.* **2012**, *134*, 14043−14049.
(266) Levine, J. R.; Cohen, J. B.; Chung, Y. W.; Georgopoulos, P. Grazing-Incidence Small-Angle X-ray Scattering: New Tool for Studying Thin Film Growth. *J. Appl. Crystallogr.* **1989**, *22*, 528−532.
(267) Revenant, C.; Leroy, F.; Lazzari, R.; Renaud, G.; Henry, C. R. Quantitative Analysis of Grazing Incidence Small-Angle X-ray Scattering: Pd/MgO(001) Growth. *Phys. Rev. B: Condens. Matter Mater. Phys.* **2004**, *69*, 035411.
(268) Rauscher, M.; Paniago, R.; Metzger, H.; Kovats, Z.; Domke, J.; Peisl, J.; Pfannes, H.-D.; Schulze, J.; Eisele, I. Grazing Incidence Small Angle X-ray Scattering from Free-Standing Nanostructures. *J. Appl. Phys.* **1999**, *86*, 6763−6769.
(269) Rauscher, M.; Salditt, T.; Spohn, H. Small-Angle X-ray Scattering under Grazing Incidence: The Cross Section in the Distorted-Wave Born Approximation. *Phys. Rev. B: Condens. Matter Mater. Phys.* **1995**, *52*, 16855−16863.
(270) Babonneau, D.; Naudon, A.; Thiaudiere, D.; Lequien, S. Morphological Characterization of Ion-Sputtered C-Ag, C/C-Ag and Ag/C Films by GISAXS. *J. Appl. Crystallogr.* **1999**, *32*, 226−233.
(271) Sinha, S. K.; Sirota, E. B.; Garoff, S.; Stanley, H. B. X-ray and Neutron Scattering from Rough Surfaces. *Phys. Rev. B: Condens. Matter Mater. Phys.* **1988**, *38*, 2297−2311.
(272) Lee, B.; Yoon, J.; Oh, W.; Hwang, Y.; Heo, K.; Jin, K. S.; Kim, J.; Kim, K.-W.; Ree, M. In-Situ Grazing Incidence Small-Angle X-ray Scattering Studies on Nanopore Evolution in Low-k Organosilicate Dielectric Thin Films. *Macromolecules* **2005**, *38*, 3395−3405.
(273) Lee, B.; Oh, W.; Yoon, J.; Hwang, Y.; Kim, J.; Landes, B. G.; Quintana, J. P.; Ree, M. Scattering Studies of Nanoporous Organosilicate Thin Films Imprinted with Reactive Star Porogens. *Macromolecules* **2005**, *38*, 8991−8995.
(274) Lazzari, R.; Leroy, F.; Renaud, G. Grazing-Incidence Small-Angle X-ray Scattering from Dense Packing of Islands on Surfaces: Development of Distorted Wave Born Approximation and Correlation between Particle Sizes and Spacing. *Phys. Rev. B: Condens. Matter Mater. Phys.* **2007**, *76*, 125411.
(275) Jiang, Z.; Lee, D. R.; Narayanan, S.; Wang, J.; Sinha, S. K. Waveguide-Enhanced Grazing-Incidence Small-Angle X-ray Scattering of Buried Nanostructures in Thin Films. *Phys. Rev. B: Condens. Matter Mater. Phys.* **2011**, *84*, 075440.
(276) Lee, B.; Lo, C.-T.; Thiyagarajan, P.; Lee, D. R.; Niu, Z.; Wang, Q. Structural Characterization using the Multiple Scattering Effects in Grazing-Incidence Small-Angle X-ray Scattering. *J. Appl. Crystallogr.* **2008**, *41*, 134−142.
(277) Babonneau, D.; Camelio, S.; Vandenhecke, E.; Rousselet, S.; Garel, M.; Pailloux, F.; Boesecke, P. Quantitative Analysis of Nanoripple and Nanoparticle Patterns by Grazing Incidence Small-Angle X-ray Scattering 3D Mapping. *Phys. Rev. B: Condens. Matter Mater. Phys.* **2012**, *85*, 235415.
(278) Müller-Buschbaum, P. In *Applications of Synchrotron Light to Scattering and Diffraction in Materials and Life Sciences*; Gomez, M., Nogales, A., Garcia-Gutierrez, M. C., Ezquerra, T. A., Eds.; Lecture Notes in Physics 776; Springer: Berlin, 2009.
(279) Durniak, C.; Ganeva, M.; Pospelov, G.; Herck, W. V.; Wuttke, J. BornAgain. http://www.bornagainproject.org/, 2015.
(280) Hexemer, A.; Muller-Buschbaum, P. Advanced Grazing-Incidence Techniques for Modern Soft-Matter Materials Analysis. *IUCrJ* **2015**, *2*, 106−125.

DOI: 10.1021/acs.chemrev.5b00690
Chem. Rev. XXXX, XXX, XXX−XXX

(281) Vineyard, G. H. Grazing-Incidence Diffraction and the Distorted-Wave Approximation for the Study of Surfaces. *Phys. Rev. B: Condens. Matter Mater. Phys.* **1982**, *26*, 4146−4159.
(282) Yoneda, Y. Anomalous Surface Reflection of X Rays. *Phys. Rev.* **1963**, *131*, 2010−2013.
(283) Lee, B.; Seifert, S.; Riley, S. J.; Tikhonov, G.; Tomczyk, N. A.; Vajda, S.; Winans, R. E. Anomalous Grazing Incidence Small-Angle X-ray Scattering Studies of Platinum Nanoparticles formed by Cluster Deposition. *J. Chem. Phys.* **2005**, *123*, 074701.
(284) Babonneau, D.; Camelio, S.; Lantiat, D.; Simonot, L.; Michel, A. Waveguiding and Correlated Roughness Effects in Layered Nanocomposite Thin Films Studied by Grazing-Incidence Small-Angle X-ray Scattering. *Phys. Rev. B: Condens. Matter Mater. Phys.* **2009**, *80*, 155446.
(285) Vegso, K.; Siffalovic, P.; Jergel, M.; Weis, M.; Benkovicova, M.; Majkova, E.; Luby, S.; Kocsis, T.; Capek, I. Silver Nanoparticle Monolayer-to-Bilayer Transition at the Air/Water Interface as Studied by the GISAXS Technique: Application of a New Paracrystal Model. *Langmuir* **2012**, *28*, 9395−9404.
(286) Jiang, Z.; He, J.; Deshmukh, S. A.; Kanjanaboos, P.; Kamath, G.; Wang, Y.; Sankaranarayanan, S. K. R. S.; Wang, J.; Jaeger, H. M.; Lin, X.-M. Subnanometre Ligand-Shell Asymmetry Leads to Janus-Like Nanoparticle Membranes. *Nat. Mater.* **2015**, *14*, 912−917.
(287) Fernandez-Martinez, A.; Hu, Y.; Lee, B.; Jun, Y.-S.; Waychunas, G. A. In Situ Determination of Interfacial Energies between Heterogeneously Nucleated $CaCO_3$ and Quartz Substrates: Thermodynamics of CO_2 Mineral Trapping. *Environ. Sci. Technol.* **2013**, *47*, 102−109.
(288) Jun, Y.-S.; Lee, B.; Waychunas, G. A. In Situ Observations of Nanoparticle Early Development Kinetics at Mineral−Water Interfaces. *Environ. Sci. Technol.* **2010**, *44*, 8182−8189.
(289) Perlich, J.; Schwartzkopf, M.; Körstgens, V.; Erb, D.; Risch, J. F. H.; Müller-Buschbaum, P.; Röhlsberger, R.; Roth, S. V.; Gehrke, R. Pattern Formation of Colloidal Suspensions by Dip-Coating: An In Situ Grazing Incidence X-ray Scattering Study. *Phys. Status Solidi RRL* **2012**, *6*, 253−255.
(290) Meshot, E. R.; Verploegen, E.; Bedewy, M.; Tawfick, S.; Woll, A. R.; Green, K. S.; Hromalik, M.; Koerner, L. J.; Philipp, H. T.; Tate, M. W.; et al. High-Speed in Situ X-ray Scattering of Carbon Nanotube Film Nucleation and Self-Organization. *ACS Nano* **2012**, *6*, 5091−5101.
(291) Kaune, G.; Ruderer, M. A.; Metwalli, E.; Wang, W.; Couet, S.; Schlage, K.; Röhlsberger, R.; Roth, S. V.; Müller-Buschbaum, P. In Situ GISAXS Study of Gold Film Growth on Conducting Polymer Films. *ACS Appl. Mater. Interfaces* **2009**, *1*, 353−360.
(292) Kutsch, B.; Lyon, O.; Schmitt, M.; Mennig, M.; Schmidt, H. Small-Angle X-ray Scattering Experiments in Grazing Incidence on Sol-Gel Coatings Containing Nano-Scaled Gold Colloids: a New Technique for Investigating Thin Coatings and Films. *J. Appl. Crystallogr.* **1997**, *30*, 948−956.
(293) Christensen, S. T.; Elam, J. W.; Lee, B.; Feng, Z.; Bedzyk, M. J.; Hersam, M. C. Nanoscale Structure and Morphology of Atomic Layer Deposition Platinum on $SrTiO_3$ (001). *Chem. Mater.* **2009**, *21*, 516−521.
(294) Fukuto, M.; Heilmann, R. K.; Pershan, P. S.; Badia, A.; Lennox, R. B. Monolayer/Bilayer Transition in Langmuir Films of Derivatized Gold Nanoparticles at the Gas/Water Interface: An X-ray Scattering Study. *J. Chem. Phys.* **2004**, *120*, 3446−3459.
(295) He, J.; Niu, Z.; Tangirala, R.; Wang, J.-Y.; Wei, X.; Kaur, G.; Wang, Q.; Jutz, G.; Böker, A.; Lee, B.; et al. Self-Assembly of Tobacco Mosaic Virus at Oil/Water Interfaces. *Langmuir* **2009**, *25*, 4979−4987.
(296) Lin, Y.; Böker, A.; Skaff, H.; Cookson, D.; Dinsmore, A. D.; Emrick, T.; Russell, T. P. Nanoparticle Assembly at Fluid Interfaces: Structure and Dynamics. *Langmuir* **2005**, *21*, 191−194.
(297) Lee, S.; Lee, B.; Seifert, S.; Vajda, S.; Winans, R. E. Simultaneous Measurement of X-ray Small Angle Scattering, Absorption and Reactivity: A Continuous Flow Catalysis Reactor. *Nucl. Instrum. Methods Phys. Res., Sect. A* **2011**, *649*, 200−203.
(298) Saint-Lager, M.-C.; Bailly, A.; Dolle, P.; Baudoing-Savois, R.; Taunier, P.; Garaudée, S.; Cuccaro, S.; Douillet, S.; Geaymond, O.; Perroux, G.; et al. New Reactor Dedicated to In Operando Studies of Model Catalysts by means of Surface X-ray Diffraction and Grazing Incidence Small Angle X-ray Scattering. *Rev. Sci. Instrum.* **2007**, *78*, 083902.
(299) Dai, Y.; Lin, B.; Meron, M.; Kim, K.; Leahy, B.; Witten, T. A.; Shpyrko, O. G. Synchrotron X-ray Studies of Rapidly Evolving Morphology of Self-Assembled Nanoparticle Films under Lateral Compression. *Langmuir* **2013**, *29*, 14050−14056.
(300) Schultz, D. G.; Lin, X.-M.; Li, D.; Gebhardt, J.; Meron, M.; Viccaro, J.; Lin, B. Structure, Wrinkling, and Reversibility of Langmuir Monolayers of Gold Nanoparticles. *J. Phys. Chem. B* **2006**, *110*, 24522−24529.
(301) Narayanan, S.; Wang, J.; Lin, X.-M. Dynamical Self-Assembly of Nanocrystal Superlattices during Colloidal Droplet Evaporation by In Situ Small Angle X-Ray Scattering. *Phys. Rev. Lett.* **2004**, *93*, 135503.
(302) Pietra, F.; Rabouw, F. T.; Evers, W. H.; Byelov, D. V.; Petukhov, A. V.; de Mello Donegá, C.; Vanmaekelbergh, D. Semiconductor Nanorod Self-Assembly at the Liquid/Air Interface Studied by in Situ GISAXS and ex Situ TEM. *Nano Lett.* **2012**, *12*, 5515−5523.
(303) Ocier, C. R.; Smilgies, D.-M.; Robinson, R. D.; Hanrath, T. Reconfigurable Nanorod Films: An in Situ Study of the Relationship between the Tunable Nanorod Orientation and the Optical Properties of Their Self-Assembled Thin Films. *Chem. Mater.* **2015**, *27*, 2659−2665.
(304) Born, P.; Schön, V.; Blum, S.; Gerstner, D.; Huber, P.; Kraus, T. Self-Assembly of Gold Nanoparticles at the Oil−Vapor Interface: From Mono- to Multilayers. *Langmuir* **2014**, *30*, 13176−13181.
(305) Kewalramani, S.; Wang, S.; Lin, Y.; Nguyen, H. G.; Wang, Q.; Fukuto, M.; Yang, L. Systematic Approach to Electrostatically Induced 2D Crystallization of Nanoparticles at Liquid Interfaces. *Soft Matter* **2011**, *7*, 939−945.
(306) Ashley, C. E.; Dunphy, D. R.; Jiang, Z.; Carnes, E. C.; Yuan, Z.; Petsev, D. N.; Atanassov, P. B.; Velev, O. D.; Sprung, M.; Wang, J.; et al. Convective Assembly of 2D Lattices of Virus-like Particles Visualized by In-Situ Grazing-Incidence Small-Angle X-Ray Scattering. *Small* **2011**, *7*, 1043−1050.
(307) Siffalovic, P.; Majkova, E.; Chitu, L.; Jergel, M.; Luby, S.; Satka, A.; Roth, S. V. Self-Assembly of Iron Oxide Nanoparticles Studied by Time-Resolved Grazing-Incidence Small-Angle X-ray Scattering. *Phys. Rev. B: Condens. Matter Mater. Phys.* **2007**, *76*, 195432.
(308) Yu, Y.; Bosoy, C. A.; Smilgies, D. M.; Korgel, B. A. Self-Assembly and Thermal Stability of Binary Superlattices of Gold and Silicon Nanocrystals. *J. Phys. Chem. Lett.* **2013**, *4*, 3677−3682.
(309) Corricelli, M.; Altamura, D.; Curri, M. L.; Sibillano, T.; Siliqi, D.; Mazzone, A.; Depalo, N.; Fanizza, E.; Zanchet, D.; Giannini, C.; et al. GISAXS and GIWAXS study on Self-Assembling Processes of Nanoparticle Based Superlattices. *CrystEngComm* **2014**, *16*, 9482−9492.
(310) Zhang, J.; Luo, Z.; Quan, Z.; Wang, Y.; Kumbhar, A.; Smilgies, D.-M.; Fang, J. Low Packing Density Self-Assembled Superstructure of Octahedral Pt_3Ni Nanocrystals. *Nano Lett.* **2011**, *11*, 2912−2918.
(311) Vegso, K.; Siffalovic, P.; Benkovicova, M.; Jergel, M.; Luby, S.; Majkova, E.; Capek, I.; Kocsis, T.; Perlich, J.; Roth, S. V. GISAXS Analysis of 3D Nanoparticle Assemblies—Effect of Vertical Nanoparticle Ordering. *Nanotechnology* **2012**, *23*, 045704.
(312) Panduro, E. A. C.; Granlund, H.; Sztucki, M.; Konovalov, O.; Breiby, D. W.; Gibaud, A. Using Three-Dimensional 3D Grazing-Incidence Small-Angle X-ray Scattering (GISAXS) Analysis To Probe Pore Deformation in Mesoporous Silica Films. *ACS Appl. Mater. Interfaces* **2014**, *6*, 2686−2691.
(313) Ross, M.; Ku, J.; Lee, B.; Mirkin, C.; Schatz, G. Plasmonic Metallurgy Enabled by DNA. *Adv. Mater.* **2016**, DOI: 10.1002/adma.201505806.
(314) Tate, M. P.; Hillhouse, H. W. General Method for Simulation of 2D GISAXS Intensities for Any Nanostructured Film Using Discrete Fourier Transforms. *J. Phys. Chem. C* **2007**, *111*, 7645−7654.

DOI: 10.1021/acs.chemrev.5b00690
Chem. Rev. XXXX, XXX, XXX−XXX

(315) Park, J.; Joo, J.; Kwon, S. G.; Jang, Y.; Hyeon, T. Synthesis of Monodisperse Spherical Nanocrystals. *Angew. Chem., Int. Ed.* **2007**, *46*, 4630−4660.
(316) Wuithschick, M.; Birnbaum, A.; Witte, S.; Sztucki, M.; Vainio, U.; Pinna, N.; Rademann, K.; Emmerling, F.; Kraehnert, R.; Polte, J. Turkevich in New Robes: Key Questions Answered for the Most Common Gold Nanoparticle Synthesis. *ACS Nano* **2015**, *9*, 7052−7071.
(317) Schiener, A.; Magerl, A.; Krach, A.; Seifert, S.; Steinruck, H. G.; Zagorac, J.; Zahn, D.; Weihrich, R. In Situ Investigation of Two-Step Nucleation and Growth of CdS Nanoparticles from Solution. *Nanoscale* **2015**, *7*, 11328−11333.
(318) Karim, A. M.; Al Hasan, N.; Ivanov, S.; Siefert, S.; Kelly, R. T.; Hallfors, N. G.; Benavidez, A. D.; Kovarik, L.; Jenkins, A.; Winans, R. E.; et al. Synthesis of 1 nm Pd Nanoparticles in a Microfluidic Reactor: Insights from In Situ XAFS and SAXS. *J. Phys. Chem. C* **2015**, *119*, 13257.
(319) Harada, M.; Saijo, K.; Sakamoto, N. Characterization of Metal Nanoparticles Prepared by Photoreduction in Aqueous Solutions of Various Surfactants using UV−Vis, EXAFS and SAXS. *Colloids Surf., A* **2009**, *349*, 176−188.
(320) Zhu, M.; Aikens, C. M.; Hollander, F. J.; Schatz, G. C.; Jin, R. Correlating the Crystal Structure of A Thiol-Protected Au_{25} Cluster and Optical Properties. *J. Am. Chem. Soc.* **2008**, *130*, 5883−5885.
(321) Heaven, M. W.; Dass, A.; White, P. S.; Holt, K. M.; Murray, R. W. Crystal Structure of the Gold Nanoparticle $[N(C_8H_{17})_4][Au_{25}(SCH_2CH_2Ph)_{18}]$. *J. Am. Chem. Soc.* **2008**, *130*, 3754−3755.
(322) Qian, H.; Eckenhoff, W. T.; Zhu, Y.; Pintauer, T.; Jin, R. Total Structure Determination of Thiolate-Protected Au_{38} Nanoparticles. *J. Am. Chem. Soc.* **2010**, *132*, 8280−8281.
(323) Vermaak, J. S.; Mays, C. W.; Kuhlmann-Wilsdorf, D. On Surface Stress and Surface Tension: I. Theoretical Considerations. *Surf. Sci.* **1968**, *12*, 128−133.
(324) Berry, C. R. Electron Diffraction from Small Crystals. *Phys. Rev.* **1952**, *88*, 596−599.
(325) Leontyev, I. N.; Kuriganova, A. B.; Leontyev, N. G.; Hennet, L.; Rakhmatullin, A.; Smirnova, N. V.; Dmitriev, V. Size Dependence of the Lattice Parameters of Carbon Supported Platinum Nanoparticles: X-ray Diffraction Analysis and Theoretical Considerations. *RSC Adv.* **2014**, *4*, 35959−35965.
(326) Menard, L. D.; Xu, H.; Gao, S.-P.; Twesten, R. D.; Harper, A. S.; Song, Y.; Wang, G.; Douglas, A. D.; Yang, J. C.; Frenkel, A. I.; et al. Metal Core Bonding Motifs of Monodisperse Icosahedral Au_{13} and Larger Au Monolayer-Protected Clusters As Revealed by X-ray Absorption Spectroscopy and Transmission Electron Microscopy. *J. Phys. Chem. B* **2006**, *110*, 14564−14573.
(327) Ino, S. Stability of Multiply-Twinned Particles. *J. Phys. Soc. Jpn.* **1969**, *27*, 941−953.
(328) Shichibu, Y.; Negishi, Y.; Watanabe, T.; Chaki, N. K.; Kawaguchi, H.; Tsukuda, T. Biicosahedral Gold Clusters $[Au_{25}(PPh_3)_{10}(SC_nH_{2n+1})_5Cl_2]^{2+}$ (n = 2−18): A Stepping Stone to Cluster-Assembled Materials. *J. Phys. Chem. C* **2007**, *111*, 7845−7847.
(329) Li, Y.; Cheng, H.; Yao, T.; Sun, Z.; Yan, W.; Jiang, Y.; Xie, Y.; Sun, Y.; Huang, Y.; Liu, S.; et al. Hexane-Driven Icosahedral to Cuboctahedral Structure Transformation of Gold Nanoclusters. *J. Am. Chem. Soc.* **2012**, *134*, 17997−18003.
(330) Niekiel, F.; Bitzek, E.; Spiecker, E. Combining Atomistic Simulation and X-ray Diffraction for the Characterization of Nanostructures: A Case Study on Fivefold Twinned Nanowires. *ACS Nano* **2014**, *8*, 1629−1638.
(331) Sanchez, S. I.; Small, M. W.; Bozin, E. S.; Wen, J.-G.; Zuo, J.-M.; Nuzzo, R. G. Metastability and Structural Polymorphism in Noble Metals: The Role of Composition and Metal Atom Coordination in Mono- and Bimetallic Nanoclusters. *ACS Nano* **2013**, *7*, 1542−1557.
(332) Heinemann, K.; Poppa, H. In-situ TEM Evidence of Lattice Expansion of Very Small Supported Palladium Particles. *Surf. Sci.* **1985**, *156*, 265−274.
(333) Neder, R. B.; Korsunskiy, V. I.; Chory, C.; Müller, G.; Hofmann, A.; Dembski, S.; Graf, C.; Rühl, E. Structural Characterization of II-VI Semiconductor Nanoparticles. *Phys. Status Solidi C* **2007**, *4*, 3221−3233.
(334) Thanh, N. T. K.; Maclean, N.; Mahiddine, S. Mechanisms of Nucleation and Growth of Nanoparticles in Solution. *Chem. Rev.* **2014**, *114*, 7610−7630.
(335) Wang, F.; Richards, V. N.; Shields, S. P.; Buhro, W. E. Kinetics and Mechanisms of Aggregative Nanocrystal Growth. *Chem. Mater.* **2014**, *26*, 5−21.
(336) Loubat, A.; Impéror-Clerc, M.; Pansu, B.; Meneau, F.; Raquet, B.; Viau, G.; Lacroix, L.-M. Growth and Self-Assembly of Ultrathin Au Nanowires into Expanded Hexagonal Superlattice Studied by in Situ SAXS. *Langmuir* **2014**, *30*, 4005−4012.
(337) Jena, B. K.; Raj, C. R. Shape-Controlled Synthesis of Gold Nanoprism and Nanoperiwinkles with Pronounced Electrocatalytic Activity. *J. Phys. Chem. C* **2007**, *111*, 15146−15153.
(338) Navaladian, S.; Janet, C. M.; Viswanathan, B.; Varadarajan, T. K.; Viswanath, R. P. A Facile Room-Temperature Synthesis of Gold Nanowires by Oxalate Reduction Method. *J. Phys. Chem. C* **2007**, *111*, 14150−14156.
(339) Kline, S. Reduction and Analysis of SANS and USANS Data using IGOR Pro. *J. Appl. Crystallogr.* **2006**, *39*, 895−900.
(340) Plech, A.; Kotaidis, V.; Lorenc, M.; Boneberg, J. Femtosecond Laser Near-Field Ablation from Gold Nanoparticles. *Nat. Phys.* **2006**, *2*, 44−47.
(341) Plech, A.; Kotaidis, V.; Lorenc, M.; Wulff, M. Thermal Dynamics in Laser Excited Metal Nanoparticles. *Chem. Phys. Lett.* **2005**, *401*, 565−569.
(342) Plech, A.; Kürbitz, S.; Berg, K. J.; Graener, H.; Berg, G.; Grésillon, S.; Kaempfe, M.; Feldmann, J.; Wulff, M.; Plessen, G. V. Time-Resolved X-ray Diffraction on Laser-Excited Metal Nanoparticles. *Europhys. Lett.* **2003**, *61*, 762−768.
(343) Ibrahimkutty, S.; Wagener, P.; Menzel, A.; Plech, A.; Barcikowski, S. Nanoparticle Formation in a Cavitation Bubble after Pulsed laser Ablation in Liquid Studied with High Time Resolution Small Angle X-ray Scattering. *Appl. Phys. Lett.* **2012**, *101*, 103104.
(344) Wu, H.; Wang, Z.; Fan, H. Stress-Induced Nanoparticle Crystallization. *J. Am. Chem. Soc.* **2014**, *136*, 7634−7636.
(345) Bremholm, M.; Jensen, H.; Iversen, S. B.; Iversen, B. B. Reactor Design for In Situ X-ray Scattering Studies of Nanoparticle Formation in Supercritical Water Syntheses. *J. Supercrit. Fluids* **2008**, *44*, 385−390.
(346) Takesue, M.; Tomura, T.; Yamada, M.; Hata, K.; Kuwamoto, S.; Yonezawa, T. Size of Elementary Clusters and Process Period in Silver Nanoparticle Formation. *J. Am. Chem. Soc.* **2011**, *133*, 14164−14167.
(347) Polte, J.; Erler, R.; Thünemann, A. F.; Sokolov, S.; Ahner, T. T.; Rademann, K.; Emmerling, F.; Kraehnert, R. Nucleation and Growth of Gold Nanoparticles Studied via In Situ Small Angle X-ray Scattering at Millisecond Time Resolution. *ACS Nano* **2010**, *4*, 1076−1082.
(348) Grillo, I. Applications of stopped-flow in SAXS and SANS. *Curr. Opin. Colloid Interface Sci.* **2009**, *14*, 402−408.
(349) Polte, J.; Tuaev, X.; Wuithschick, M.; Fischer, A.; Thuenemann, A. F.; Rademann, K.; Kraehnert, R.; Emmerling, F. Formation Mechanism of Colloidal Silver Nanoparticles: Analogies and Differences to the Growth of Gold Nanoparticles. *ACS Nano* **2012**, *6*, 5791−5802.
(350) Harada, M.; Tamura, N.; Takenaka, M. Nucleation and Growth of Metal Nanoparticles during Photoreduction Using In Situ Time-Resolved SAXS Analysis. *J. Phys. Chem. C* **2011**, *115*, 14081−14092.
(351) Polte, J.; Erler, R.; Thunemann, A. F.; Emmerling, F.; Kraehnert, R. SAXS in Combination with a Free Liquid Jet for Improved Time-Resolved In Situ Studies of the Nucleation and Growth of Nanoparticles. *Chem. Commun.* **2010**, *46*, 9209−9211.
(352) Abécassis, B.; Testard, F.; Spalla, O.; Barboux, P. Probing in situ the Nucleation and Growth of Gold Nanoparticles by Small-Angle X-ray Scattering. *Nano Lett.* **2007**, *7*, 1723−1727.

DOI: 10.1021/acs.chemrev.5b00690
Chem. Rev. XXXX, XXX, XXX−XXX

(353) LaGrow, A. P.; Ingham, B.; Toney, M. F.; Tilley, R. D. Effect of Surfactant Concentration and Aggregation on the Growth Kinetics of Nickel Nanoparticles. *J. Phys. Chem. C* **2013**, *117*, 16709−16718.
(354) Becker, J.; Bremholm, M.; Tyrsted, C.; Pauw, B.; Jensen, K. M. O.; Eltzholt, J.; Christensen, M.; Iversen, B. B. Experimental Setup for In Situ X-ray SAXS/WAXS/PDF Studies of the Formation and Growth of Nanoparticles in Near- and Supercritical Fluids. *J. Appl. Crystallogr.* **2010**, *43*, 729−736.
(355) Abécassis, B.; Bouet, C.; Garnero, C.; Constantin, D.; Lequeux, N.; Ithurria, S.; Dubertret, B.; Pauw, B. R.; Pontoni, D. Real-Time in Situ Probing of High-Temperature Quantum Dots Solution Synthesis. *Nano Lett.* **2015**, *15*, 2620−2626.
(356) Mi, J.-L.; Jensen, T. N.; Christensen, M.; Tyrsted, C.; Jørgensen, J. E.; Iversen, B. B. High-Temperature and High-Pressure Aqueous Solution Formation, Growth, Crystal Structure, and Magnetic Properties of $BiFeO_3$ Nanocrystals. *Chem. Mater.* **2011**, *23*, 1158−1165.
(357) Smith, R. L., Jr; Fang, Z. Techniques, Applications and Future Prospects of Diamond Anvil Cells for Studying Supercritical Water Systems. *J. Supercrit. Fluids* **2009**, *47*, 431−446.
(358) Bremholm, M.; Becker-Christensen, J.; Iversen, B. B. High-Pressure, High-Temperature Formation of Phase-Pure Monoclinic Zirconia Nanocrystals Studied by Time-Resolved in situ Synchrotron X-Ray Diffraction. *Adv. Mater.* **2009**, *21*, 3572−3575.
(359) Caetano, B. L.; Santilli, C. V.; Meneau, F.; Briois, V.; Pulcinelli, S. H. In Situ and Simultaneous UV−Vis/SAXS and UV−Vis/XAFS Time-Resolved Monitoring of ZnO Quantum Dots Formation and Growth. *J. Phys. Chem. C* **2011**, *115*, 4404−4412.
(360) Polte, J.; Ahner, T. T.; Delissen, F.; Sokolov, S.; Emmerling, F.; Thünemann, A. F.; Kraehnert, R. Mechanism of Gold Nanoparticle Formation in the Classical Citrate Synthesis Method Derived from Coupled In Situ XANES and SAXS Evaluation. *J. Am. Chem. Soc.* **2010**, *132*, 1296−1301.
(361) Beale, A. M.; van der Eerden, A. M. J.; Jacques, S. D. M.; Leynaud, O.; O'Brien, M. G.; Meneau, F.; Nikitenko, S.; Bras, W.; Weckhuysen, B. M. A Combined SAXS/WAXS/XAFS Setup Capable of Observing Concurrent Changes Across the Nano-to-Micrometer Size Range in Inorganic Solid Crystallization Processes. *J. Am. Chem. Soc.* **2006**, *128*, 12386−12387.
(362) Bentrup, U.; Radnik, J.; Armbruster, U.; Martin, A.; Leiterer, J.; Emmerling, F.; Brückner, A. Linking Simultaneous In Situ WAXS/SAXS/Raman with Raman/ATR/UV−Vis Spectroscopy: Comprehensive Insight into the Synthesis of Molybdate Catalyst Precursors. *Top. Catal.* **2009**, *52*, 1350−1359.
(363) Chen, X.; Schröder, J.; Hauschild, S.; Rosenfeldt, S.; Dulle, M.; Förster, S. Simultaneous SAXS/WAXS/UV−Vis Study of the Nucleation and Growth of Nanoparticles: A Test of Classical Nucleation Theory. *Langmuir* **2015**, *31*, 11678−11691.
(364) Eustis, S.; Hsu, H.-Y.; El-Sayed, M. A. Gold Nanoparticle Formation from Photochemical Reduction of Au3+ by Continuous Excitation in Colloidal Solutions. A Proposed Molecular Mechanism. *J. Phys. Chem. B* **2005**, *109*, 4811−4815.
(365) Khodakov, A. Y.; Zholobenko, V. L.; Impéror-Clerc, M.; Durand, D. Characterization of the Initial Stages of SBA-15 Synthesis by in Situ Time-Resolved Small-Angle X-ray Scattering. *J. Phys. Chem. B* **2005**, *109*, 22780−22790.
(366) Amstad, E.; Gopinadhan, M.; Holtze, C.; Osuji, C. O.; Brenner, M. P.; Spaepen, F.; Weitz, D. A. Production of Amorphous Nanoparticles by Supersonic Spray-Drying with a Microfluidic Nebulator. *Science* **2015**, *349*, 956−960.
(367) Merlin, A.; Angly, J.; Daubersies, L.; Madeira, C.; Schöder, S.; Leng, J.; Salmon, J. B. Time-resolved Microfocused Small-Angle X-ray Scattering Investigation of the Microfluidic Concentration of Charged Nanoparticles. *Eur. Phys. J. E: Soft Matter Biol. Phys.* **2011**, *34*, 58.
(368) Marmiroli, B.; Grenci, G.; Cacho-Nerin, F.; Sartori, B.; Laggner, P.; Businaro, L.; Amenitsch, H. Experimental Set-Up for Time Resolved Small Angle X-ray Scattering Studies of Nanoparticles Formation using a Free-Jet Micromixer. *Nucl. Instrum. Methods Phys. Res., Sect. B* **2010**, *268*, 329−333.
(369) Hendel, T.; Wuithschick, M.; Kettemann, F.; Birnbaum, A.; Rademann, K.; Polte, J. In Situ Determination of Colloidal Gold Concentrations with UV−Vis Spectroscopy: Limitations and Perspectives. *Anal. Chem.* **2014**, *86*, 11115−11124.
(370) Abécassis, B.; Testard, F.; Kong, Q.; Francois, B.; Spalla, O. Influence of Monomer Feeding on a Fast Gold Nanoparticles Synthesis: Time-Resolved XANES and SAXS Experiments. *Langmuir* **2010**, *26*, 13847−13854.
(371) Peng, S.; Okasinski, J. S.; Almer, J. D.; Ren, Y.; Wang, L.; Yang, W.; Sun, Y. Real-Time Probing of the Synthesis of Colloidal Silver Nanocubes with Time-Resolved High-Energy Synchrotron X-ray Diffraction. *J. Phys. Chem. C* **2012**, *116*, 11842−11847.
(372) Harada, M.; Kamigaito, Y. Nucleation and Aggregative Growth Process of Platinum Nanoparticles Studied by in Situ Quick XAFS Spectroscopy. *Langmuir* **2012**, *28*, 2415−2428.
(373) LaMer, V. K.; Dinegar, R. H. Theory, Production and Mechanism of Formation of Monodispersed Hydrosols. *J. Am. Chem. Soc.* **1950**, *72*, 4847−4854.
(374) Koerner, H.; MacCuspie, R. I.; Park, K.; Vaia, R. A. In Situ UV/Vis, SAXS, and TEM Study of Single-Phase Gold Nanoparticle Growth. *Chem. Mater.* **2012**, *24*, 981−995.
(375) Watzky, M. A.; Finke, R. G. Transition Metal Nanocluster Formation Kinetic and Mechanistic Studies. A New Mechanism When Hydrogen Is the Reductant: Slow, Continuous Nucleation and Fast Autocatalytic Surface Growth. *J. Am. Chem. Soc.* **1997**, *119*, 10382−10400.
(376) Zheng, H.; Smith, R. K.; Jun, Y.-W.; Kisielowski, C.; Dahmen, U.; Alivisatos, A. P. Observation of Single Colloidal Platinum Nanocrystal Growth Trajectories. *Science* **2009**, *324*, 1309−1312.
(377) Baumgartner, J.; Dey, A.; Bomans, P. H. H.; Le Coadou, C.; Fratzl, P.; Sommerdijk, N. A. J. M.; Faivre, D. Nucleation and Growth of Magnetite from Solution. *Nat. Mater.* **2013**, *12*, 310−314.
(378) Yao, T.; Sun, Z.; Li, Y.; Pan, Z.; Wei, H.; Xie, Y.; Nomura, M.; Niwa, Y.; Yan, W.; Wu, Z.; et al. Insights into Initial Kinetic Nucleation of Gold Nanocrystals. *J. Am. Chem. Soc.* **2010**, *132*, 7696−7701.
(379) Reiss, H. The Statistical Mechanical Theory of Irreversible Condensation. I. *J. Chem. Phys.* **1952**, *20*, 1216−1227.
(380) Uyeda, N.; Nishino, M.; Suito, E. Nucleus Interaction and Fine Structures of Colloidal Gold Particles. *J. Colloid Interface Sci.* **1973**, *43*, 264−276.
(381) Turkevich, J. Colloidal gold. Part I. *Gold Bull.* **1985**, *18*, 86−91.
(382) Van Hyning, D. L.; Klemperer, W. G.; Zukoski, C. F. Silver Nanoparticle Formation: Predictions and Verification of the Aggregative Growth Model. *Langmuir* **2001**, *17*, 3128−3135.
(383) Sholl, D. S.; Skodje, R. T. Late-Stage Coarsening of Adlayers by Dynamic Cluster Coalescence. *Phys. A* **1996**, *231*, 631−647.
(384) Pontoni, D.; Narayanan, T.; Rennie, A. R. Time-Resolved SAXS Study of Nucleation and Growth of Silica Colloids. *Langmuir* **2002**, *18*, 56−59.
(385) Kellermann, G.; Craievich, A. F. Isothermal Aggregation of Ag Atoms in Sodium Borate Glass. *Phys. Rev. B: Condens. Matter Mater. Phys.* **2004**, *70*, 054106.
(386) Meli, L.; Green, P. F. Aggregation and Coarsening of Ligand-Stabilized Gold Nanoparticles in Poly(methyl methacrylate) Thin Films. *ACS Nano* **2008**, *2*, 1305−1312.
(387) Woehl, T. J.; Park, C.; Evans, J. E.; Arslan, I.; Ristenpart, W. D.; Browning, N. D. Direct Observation of Aggregative Nanoparticle Growth: Kinetic Modeling of the Size Distribution and Growth Rate. *Nano Lett.* **2014**, *14*, 373−378.
(388) O'Brien, M. N.; Jones, M. R.; Brown, K. A.; Mirkin, C. A. Universal Noble Metal Nanoparticle Seeds Realized Through Iterative Reductive Growth and Oxidative Dissolution Reactions. *J. Am. Chem. Soc.* **2014**, *136*, 7603−7606.
(389) Lu, F.; Yager, K. G.; Zhang, Y.; Xin, H.; Gang, O. Superlattices Assembled through Shape-Induced Directional Binding. *Nat. Commun.* **2015**, *6*, 6912.
(390) Liu, H.; Hsu, C.-H.; Lin, Z.; Shan, W.; Wang, J.; Jiang, J.; Huang, M.; Lotz, B.; Yu, X.; Zhang, W.-B.; et al. Two-Dimensional

DOI: 10.1021/acs.chemrev.5b00690
Chem. Rev. XXXX, XXX, XXX−XXX

Nanocrystals of Molecular Janus Particles. *J. Am. Chem. Soc.* **2014**, *136*, 10691−10699.
(391) Huang, M.; Hsu, C.-H.; Wang, J.; Mei, S.; Dong, X.; Li, Y.; Li, M.; Liu, H.; Zhang, W.; Aida, T.; et al. Selective Assemblies of Giant Tetrahedra via Precisely Controlled Positional Interactions. *Science* **2015**, *348*, 424−428.
(392) Urban, J. J.; Talapin, D. V.; Shevchenko, E. V.; Kagan, C. R.; Murray, C. B. Synergism in Binary Nanocrystal Superlattices Leads to Enhanced p-type Conductivity in Self-Assembled PbTe/Ag2Te Thin Films. *Nat. Mater.* **2007**, *6*, 115−121.
(393) Sun, S.; Murray, C. B.; Weller, D.; Folks, L.; Moser, A. Monodisperse FePt Nanoparticles and Ferromagnetic FePt Nanocrystal Superlattices. *Science* **2000**, *287*, 1989−1992.
(394) Ross, M. B.; Ku, J. C.; Vaccarezza, V. M.; Schatz, G. C.; Mirkin, C. A. Nanoscale form Dictates MesoscaleFunction in Plasmonic DNA−Nanoparticle Superlattices. *Nat. Nanotechnol.* **2015**, *10*, 453−458.
(395) Jones, M. R.; Seeman, N. C.; Mirkin, C. A. Programmable Materials and the Nature of the DNA Bond. *Science* **2015**, *347*, 1260901.
(396) Mirkin, C. A.; Letsinger, R. L.; Mucic, R. C.; Storhoff, J. J. A DNA-based Method for Rationally Assembling Nanoparticles into Macroscopic Materials. *Nature* **1996**, *382*, 607−609.
(397) Alivisatos, A. P.; Johnsson, K. P.; Peng, X.; Wilson, T. E.; Loweth, C. J.; Bruchez, M. P.; Schultz, P. G. Organization of 'Nanocrystal Molecules' using DNA. *Nature* **1996**, *382*, 609−611.
(398) Park, S.-J.; Lazarides, A. A.; Storhoff, J. J.; Pesce, L.; Mirkin, C. A. The Structural Characterization of Oligonucleotide-Modified Gold Nanoparticle Networks Formed by DNA Hybridization. *J. Phys. Chem. B* **2004**, *108*, 12375−12380.
(399) Macfarlane, R. J.; O'Brien, M. N.; Petrosko, S. H.; Mirkin, C. A. Nucleic Acid-Modified Nanostructures as Programmable Atom Equivalents: Forging a New "Table of Elements. *Angew. Chem., Int. Ed.* **2013**, *52*, 5688−5698.
(400) Auyeung, E.; Li, T. I. N. G.; Senesi, A. J.; Schmucker, A. L.; Pals, B. C.; de la Cruz, M. O.; Mirkin, C. A. DNA-Mediated Nanoparticle Crystallization into Wulff Polyhedra. *Nature* **2014**, *505*, 73−77.
(401) Auyeung, E.; Cutler, J. I.; Macfarlane, R. J.; Jones, M. R.; Wu, J.; Liu, G.; Zhang, K.; Osberg, K. D.; Mirkin, C. A. Synthetically Programmable Nanoparticle Superlattices using a Hollow Three-Dimensional Spacer Approach. *Nat. Nanotechnol.* **2012**, *7*, 24−28.
(402) Zhang, C.; Macfarlane, R. J.; Young, K. L.; Choi, C. H. J.; Hao, L.; Auyeung, E.; Liu, G.; Zhou, X.; Mirkin, C. A. A General Approach to DNA-Programmable Atom Equivalents. *Nat. Mater.* **2013**, *12*, 741−746.
(403) Cigler, P.; Lytton-Jean, A. K. R.; Anderson, D. G.; Finn, M. G.; Park, S. Y. DNA-Controlled Assembly of a NaTl Lattice Structure from Gold Nanoparticles and Protein Nanoparticles. *Nat. Mater.* **2010**, *9*, 918−922.
(404) Zhang, Y.; Lu, F.; Yager, K. G.; van der Lelie, D.; Gang, O. A General Strategy for the DNA-Mediated Self-Assembly of Functional Nanoparticles into Heterogeneous Systems. *Nat. Nanotechnol.* **2013**, *8*, 865−872.
(405) Maye, M. M.; Kumara, M. T.; Nykypanchuk, D.; Sherman, W. B.; Gang, O. Switching Binary States of Nanoparticle Superlattices and Dimer Clusters by DNA Strands. *Nat. Nanotechnol.* **2010**, *5*, 116−120.
(406) Kim, Y.; Macfarlane, R. J.; Mirkin, C. A. Dynamically Interchangeable Nanoparticle Superlattices Through the Use of Nucleic Acid-Based Allosteric Effectors. *J. Am. Chem. Soc.* **2013**, *135*, 10342−10345.
(407) Zhang, Y.; Pal, S.; Srinivasan, B.; Vo, T.; Kumar, S.; Gang, O. Selective Transformations between Nanoparticle Superlattices via the Reprogramming of DNA-Mediated Interactions. *Nat. Mater.* **2015**, *14*, 840−847.
(408) Hellstrom, S. L.; Kim, Y.; Fakonas, J. S.; Senesi, A. J.; Macfarlane, R. J.; Mirkin, C. A.; Atwater, H. A. Epitaxial Growth of DNA-Assembled Nanoparticle Superlattices on Patterned Substrates. *Nano Lett.* **2013**, *13*, 6084−6090.
(409) Norsten, T. B.; Frankamp, B. L.; Rotello, V. M. Metal Directed Assembly of Terpyridine-Functionalized Gold Nanoparticles. *Nano Lett.* **2002**, *2*, 1345−1348.
(410) Hirai, K.; Yeom, B.; Chang, S.-H.; Chi, H.; Mansfield, J. F.; Lee, B.; Lee, S.; Uher, C.; Kotov, N. A. Coordination Assembly of Discoid Nanoparticles. *Angew. Chem., Int. Ed.* **2015**, *54*, 8966−8970.
(411) Zeng, X.; Liu, F.; Fowler, A. G.; Ungar, G.; Cseh, L.; Mehl, G. H.; Macdonald, J. E. 3D Ordered Gold Strings by Coating Nanoparticles with Mesogens. *Adv. Mater.* **2009**, *21*, 1746−1750.
(412) Lewandowski, W.; Jatczak, K.; Pociecha, D.; Mieczkowski, J. Control of Gold Nanoparticle Superlattice Properties via Mesogenic Ligand Architecture. *Langmuir* **2013**, *29*, 3404−3410.
(413) Mischler, S.; Guerra, S.; Deschenaux, R. Design of Liquid-Crystalline Gold Nanoparticles by Click Chemistry. *Chem. Commun.* **2012**, *48*, 2183−2185.
(414) Yu, C. H.; Schubert, C. P. J.; Welch, C.; Tang, B. J.; Tamba, M. G.; Mehl, G. H. Design, Synthesis, and Characterization of Mesogenic Amine-Capped Nematic Gold Nanoparticles with Surface-Enhanced Plasmonic Resonances. *J. Am. Chem. Soc.* **2012**, *134*, 5076−5079.
(415) Mang, X.; Zeng, X.; Tang, B.; Liu, F.; Ungar, G.; Zhang, R.; Cseh, L.; Mehl, G. H. Control of Anisotropic Self-assembly of Gold Nanoparticles Coated with Mesogens. *J. Mater. Chem.* **2012**, *22*, 11101−11106.
(416) Marx, V. M.; Girgis, H.; Heiney, P. A.; Hegmann, T. Bent-Core Liquid Crystal (LC) Decorated Gold Nanoclusters: Synthesis, Self-assembly, and Effects in Mixtures with Bent-Core LC Hosts. *J. Mater. Chem.* **2008**, *18*, 2983−2994.
(417) Kanie, K.; Matsubara, M.; Zeng, X.; Liu, F.; Ungar, G.; Nakamura, H.; Muramatsu, A. Simple Cubic Packing of Gold Nanoparticles through Rational Design of Their Dendrimeric Corona. *J. Am. Chem. Soc.* **2012**, *134*, 808−811.
(418) Wojcik, M. M.; Gora, M.; Mieczkowski, J.; Romiszewski, J.; Gorecka, E.; Pociecha, D. Temperature-Controlled Liquid Crystalline Polymorphism of Gold Nanoparticles. *Soft Matter* **2011**, *7*, 10561−10564.
(419) Scheele, M.; Hanifi, D.; Zherebetskyy, D.; Chourou, S. T.; Axnanda, S.; Rancatore, B. J.; Thorkelsson, K.; Xu, T.; Liu, Z.; Wang, L.-W.; et al. PbS Nanoparticles Capped with Tetrathiafulvalenetetracarboxylate: Utilizing Energy Level Alignment for Efficient Carrier Transport. *ACS Nano* **2014**, *8*, 2532−2540.
(420) Kao, J.; Thorkelsson, K.; Bai, P.; Zhang, Z.; Sun, C.; Xu, T. Rapid Fabrication of Hierarchically Structured Supramolecular Nanocomposite Thin Films in One Minute. *Nat. Commun.* **2014**, *5*, 4053.
(421) Kao, J.; Jeong, S.-J.; Jiang, Z.; Lee, D. H.; Aissou, K.; Ross, C. A.; Russell, T. P.; Xu, T. Direct 3-D Nanoparticle Assemblies in Thin Films via Topographically Patterned Surfaces. *Adv. Mater.* **2014**, *26*, 2777−2781.
(422) Kao, J.; Thorkelsson, K.; Bai, P.; Rancatore, B. J.; Xu, T. Toward Functional Nanocomposites: Taking the Best of Nanoparticles, Polymers, and Small Molecules. *Chem. Soc. Rev.* **2013**, *42*, 2654−2678.
(423) Lee, B.; Lo, C.-T.; Seifert, S.; Dietz Rago, N. L.; Winans, R. E.; Thiyagarajan, P. Anomalous Small-Angle X-ray Scattering Characterization of Bulk Block Copolymer/Nanoparticle Composites. *Macromolecules* **2007**, *40*, 4235−4243.
(424) Zhao, Y.; Thorkelsson, K.; Mastroianni, A. J.; Schilling, T.; Luther, J. M.; Rancatore, B. J.; Matsunaga, K.; Jinnai, H.; Wu, Y.; Poulsen, D.; et al. Small-Molecule-Directed Nanoparticle Assembly towards Stimuli-Responsive Nanocomposites. *Nat. Mater.* **2009**, *8*, 979−985.
(425) Asakura, S.; Oosawa, F. Interaction between Particles Suspended in Solutions of Macromolecules. *J. Polym. Sci.* **1958**, *33*, 183−192.
(426) Baranov, D.; Fiore, A.; van Huis, M.; Giannini, C.; Falqui, A.; Lafont, U.; Zandbergen, H.; Zanella, M.; Cingolani, R.; Manna, L. Assembly of Colloidal Semiconductor Nanorods in Solution by Depletion Attraction. *Nano Lett.* **2010**, *10*, 743−749.
(427) Sacanna, S.; Irvine, W. T. M.; Chaikin, P. M.; Pine, D. J. Lock and Key Colloids. *Nature* **2010**, *464*, 575−578.

DOI: 10.1021/acs.chemrev.5b00690
Chem. Rev. XXXX, XXX, XXX−XXX

(428) Li, T.; Zan, X.; Winans, R. E.; Wang, Q.; Lee, B. Biomolecular Assembly of Thermoresponsive Superlattices of the Tobacco Mosaic Virus with Large Tunable Interparticle Distances. *Angew. Chem., Int. Ed.* **2013**, *52*, 6638−6642.
(429) Henzie, J.; Grünwald, M.; Widmer-Cooper, A.; Geissler, P. L.; Yang, P. Self-Assembly of Uniform Polyhedral Silver Nanocrystals into Densest Packings and Exotic Superlattices. *Nat. Mater.* **2012**, *11*, 131−137.
(430) Dong, A.; Chen, J.; Vora, P. M.; Kikkawa, J. M.; Murray, C. B. Binary Nanocrystal Superlattice Membranes Self-Assembled at the Liquid-Air Interface. *Nature* **2010**, *466*, 474−477.
(431) Korgel, B. A.; Zaccheroni, N.; Fitzmaurice, D. Melting Transition" of A Quantum Dot Solid: Collective Interactions Influence the Thermally-Induced Order−Disorder Transition of A Silver Nanocrystal Superlattice. *J. Am. Chem. Soc.* **1999**, *121*, 3533−3534.
(432) Goodfellow, B. W.; Patel, R. N.; Panthani, M. G.; Smilgies, D.-M.; Korgel, B. A. Melting and Sintering of a Body-Centered Cubic Superlattice of PbSe Nanocrystals Followed by Small Angle X-ray Scattering. *J. Phys. Chem. C* **2011**, *115*, 6397−6404.
(433) Chan, H.; Demortière, A.; Vukovic, L.; Král, P.; Petit, C. Colloidal Nanocube Supercrystals Stabilized by Multipolar Coulombic Coupling. *ACS Nano* **2012**, *6*, 4203−4213.
(434) Weidman, M. C.; Yager, K. G.; Tisdale, W. A. Interparticle Spacing and Structural Ordering in Superlattice PbS Nanocrystal Solids Undergoing Ligand Exchange. *Chem. Mater.* **2015**, *27*, 474−482.
(435) Podsiadlo, P.; Lee, B.; Prakapenka, V. B.; Krylova, G. V.; Schaller, R. D.; Demortière, A.; Shevchenko, E. V. High-Pressure Structural Stability and Elasticity of Supercrystals Self-Assembled from Nanocrystals. *Nano Lett.* **2011**, *11*, 579−588.
(436) Bian, K.; Wang, Z.; Hanrath, T. Comparing the Structural Stability of PbS Nanocrystals Assembled in FCC and BCC Superlattice Allotropes. *J. Am. Chem. Soc.* **2012**, *134*, 10787−10790.
(437) Podsiadlo, P.; Krylova, G.; Lee, B.; Critchley, K.; Gosztola, D. J.; Talapin, D. V.; Ashby, P. D.; Shevchenko, E. V. The Role of Order, Nanocrystal Size, and Capping Ligands in the Collective Mechanical Response of Three-Dimensional Nanocrystal Solids. *J. Am. Chem. Soc.* **2010**, *132*, 8953−8960.
(438) Lee, B.; Podsiadlo, P.; Rupich, S.; Talapin, D. V.; Rajh, T.; Shevchenko, E. V. Comparison of Structural Behavior of Nanocrystals in Randomly Packed Films and Long-Range Ordered Superlattices by Time-Resolved Small Angle X-ray Scattering. *J. Am. Chem. Soc.* **2009**, *131*, 16386−16388.
(439) Wu, H.; Bai, F.; Sun, Z.; Haddad, R. E.; Boye, D. M.; Wang, Z.; Huang, J. Y.; Fan, H. Nanostructured Gold Architectures Formed through High Pressure-Driven Sintering of Spherical Nanoparticle Arrays. *J. Am. Chem. Soc.* **2010**, *132*, 12826−12828.
(440) Goodfellow, B. W.; Rasch, M. R.; Hessel, C. M.; Patel, R. N.; Smilgies, D.-M.; Korgel, B. A. Ordered Structure Rearrangements in Heated Gold Nanocrystal Superlattices. *Nano Lett.* **2013**, *13*, 5710−5714.
(441) Murray, C. B.; Kagan, C. R.; Bawendi, M. G. Synthesis and Characterization of Monodisperse Nanocrystals and Close-packed Nanocrystal Assemblies. *Annu. Rev. Mater. Sci.* **2000**, *30*, 545−610.
(442) Byelov, D. V.; Hilhorst, J.; Leferink op Reinink, A. B. G. M.; Snigireva, I.; Snigirev, A.; Vaughan, G. B. M.; Portale, G.; Petukhov, A. V. Diffuse Scattering in Random-Stacking Hexagonal Close-Packed Crystals of Colloidal Hard Spheres. *Phase Transitions* **2010**, *83*, 107−114.
(443) Balogh, L.; Ribárik, G.; Ungár, T. Stacking Faults and Twin Boundaries in FCC Crystals Determined by X-ray Diffraction Profile Analysis. *J. Appl. Phys.* **2006**, *100*, 023512.
(444) Baranov, A. V.; Ushakova, E. V.; Golubkov, V. V.; Litvin, A. P.; Parfenov, P. S.; Fedorov, A. V.; Berwick, K. Self-Organization of Colloidal PbS Quantum Dots into Highly Ordered Superlattices. *Langmuir* **2015**, *31*, 506−513.
(445) Wan, Y.; Goubet, N.; Albouy, P.-A.; Schaeffer, N.; Pileni, M.-P. Hierarchy in Au Nanocrystal Ordering in a Supracrystal: II. Control of Interparticle Distances. *Langmuir* **2013**, *29*, 13576−13581.
(446) Murray, C. B.; Kagan, C. R.; Bawendi, M. G. Self-Organization of CdSe Nanocrystallites into Three-Dimensional Quantum Dot Superlattices. *Science* **1995**, *270*, 1335−1338.
(447) Hamley, I. W.; Daniel, C.; Mingvanish, W.; Mai, S.-M.; Booth, C.; Messe, L.; Ryan, A. J. From Hard Spheres to Soft Spheres: The Effect of Copolymer Composition on the Structure of Micellar Cubic Phases Formed by Diblock Copolymers in Aqueous Solution. *Langmuir* **2000**, *16*, 2508−2514.
(448) Damasceno, P. F.; Engel, M.; Glotzer, S. C. Predictive Self-Assembly of Polyhedra into Complex Structures. *Science* **2012**, *337*, 453−457.
(449) Disch, S.; Wetterskog, E.; Hermann, R. P.; Salazar-Alvarez, G.; Busch, P.; Brückel, T.; Bergström, L.; Kamali, S. Shape Induced Symmetry in Self-Assembled Mesocrystals of Iron Oxide Nanocubes. *Nano Lett.* **2011**, *11*, 1651−1656.
(450) Zhang, Y.; Lu, F.; van der Lelie, D.; Gang, O. Continuous Phase Transformation in Nanocube Assemblies. *Phys. Rev. Lett.* **2011**, *107*, 135701.
(451) Boles, M. A.; Talapin, D. V. Self-Assembly of Tetrahedral CdSe Nanocrystals: Effective "Patchiness" via Anisotropic Steric Interaction. *J. Am. Chem. Soc.* **2014**, *136*, 5868−5871.
(452) Javon, E.; Gaceur, M.; Dachraoui, W.; Margeat, O.; Ackermann, J.; Saba, M. I.; Delugas, P.; Mattoni, A.; Bals, S.; Van Tendeloo, G. Competing Forces in the Self-Assembly of Coupled ZnO Nanopyramids. *ACS Nano* **2015**, *9*, 3685−3694.
(453) Diroll, B. T.; Doan-Nguyen, V. V. T.; Cargnello, M.; Gaulding, E. A.; Kagan, C. R.; Murray, C. B. X-ray Mapping of Nanoparticle Superlattice Thin Films. *ACS Nano* **2014**, *8*, 12843−12850.
(454) Petukhov, A. V.; Meijer, J.-M.; Vroege, G. J. Particle Shape Effects in Colloidal Crystals and Colloidal Liquid Crystals: Small-Angle X-ray Scattering Studies with Microradian Resolution. *Curr. Opin. Colloid Interface Sci.* **2015**, *20*, 272−281.
(455) Zhao, K.; Mason, T. G. Twinning of Rhombic Colloidal Crystals. *J. Am. Chem. Soc.* **2012**, *134*, 18125−18131.
(456) Chen, C.-F.; Tzeng, S.-D.; Chen, H.-Y.; Lin, K.-J.; Gwo, S. Tunable Plasmonic Response from Alkanethiolate-Stabilized Gold Nanoparticle Superlattices: Evidence of Near-Field Coupling. *J. Am. Chem. Soc.* **2008**, *130*, 824−826.
(457) He, J.; Kanjanaboos, P.; Frazer, N. L.; Weis, A.; Lin, X.-M.; Jaeger, H. M. Fabrication and Mechanical Properties of Large-Scale Freestanding Nanoparticle Membranes. *Small* **2010**, *6*, 1449−1456.
(458) Cargnello, M.; Johnston-Peck, A. C.; Diroll, B. T.; Wong, E.; Datta, B.; Damodhar, D.; Doan-Nguyen, V. V. T.; Herzing, A. A.; Kagan, C. R.; Murray, C. B. Substitutional Doping in Nanocrystal Superlattices. *Nature* **2015**, *524*, 450−453.
(459) Greshnykh, D.; Frömsdorf, A.; Weller, H.; Klinke, C. On the Electric Conductivity of Highly Ordered Monolayers of Monodisperse Metal Nanoparticles. *Nano Lett.* **2009**, *9*, 473−478.
(460) Min, Y.; Akbulut, M.; Kristiansen, K.; Golan, Y.; Israelachvili, J. The Role of Interparticle and External Forces in Nanoparticle Assembly. *Nat. Mater.* **2008**, *7*, 527−538.
(461) Mueggenburg, K. E.; Lin, X.-M.; Goldsmith, R. H.; Jaeger, H. M. Elastic Membranes of Close-Packed Nanoparticle Arrays. *Nat. Mater.* **2007**, *6*, 656−660.
(462) Terrill, R. H.; Postlethwaite, T. A.; Chen, C.-h.; Poon, C.-D.; Terzis, A.; Chen, A.; Hutchison, J. E.; Clark, M. R.; Wignall, G. Monolayers in Three Dimensions: NMR, SAXS, Thermal, and Electron Hopping Studies of Alkanethiol Stabilized Gold Clusters. *J. Am. Chem. Soc.* **1995**, *117*, 12537−12548.
(463) Beard, M. C.; Midgett, A. G.; Law, M.; Semonin, O. E.; Ellingson, R. J.; Nozik, A. J. Variations in the Quantum Efficiency of Multiple Exciton Generation for a Series of Chemically Treated PbSe Nanocrystal Films. *Nano Lett.* **2009**, *9*, 836−845.
(464) Luther, J. M.; Beard, M. C.; Song, Q.; Law, M.; Ellingson, R. J.; Nozik, A. J. Multiple Exciton Generation in Films of Electronically Coupled PbSe Quantum Dots. *Nano Lett.* **2007**, *7*, 1779−1784.
(465) Talapin, D. V.; Murray, C. B. PbSe Nanocrystal Solids for n- and p-Channel Thin Film Field-Effect Transistors. *Science* **2005**, *310*, 86−89.

DOI: 10.1021/acs.chemrev.5b00690
Chem. Rev. XXXX, XXX, XXX−XXX

(466) Shevchenko, E.; Talapin, D.; Kornowski, A.; Wiekhorst, F.; Kötzler, J.; Haase, M.; Rogach, A.; Weller, H. Colloidal Crystals of Monodisperse FePt Nanoparticles Grown by a Three-Layer Technique of Controlled Oversaturation. *Adv. Mater.* **2002**, *14*, 287−290.

(467) Gilbert, J. A.; Kariuki, N. N.; Wang, X.; Kropf, A. J.; Yu, K.; Groom, D. J.; Ferreira, P. J.; Morgan, D.; Myers, D. J. Pt Catalyst Degradation in Aqueous and Fuel Cell Environments Studied via In-Operando Anomalous Small-Angle X-ray Scattering. *Electrochim. Acta* **2015**, *173*, 223−234.

(468) Park, G. O.; Yoon, J.; Park, E.; Park, S. B.; Kim, H.; Kim, K. H.; Jin, X.; Shin, T. J.; Kim, H.; Yoon, W.-S.; et al. In Operando Monitoring of the Pore Dynamics in Ordered Mesoporous Electrode Materials by Small Angle X-ray Scattering. *ACS Nano* **2015**, *9*, 5470−5477.

(469) Wiaderek, K. M.; Borkiewicz, O. J.; Pereira, N.; Ilavsky, J.; Amatucci, G. G.; Chupas, P. J.; Chapman, K. W. Mesoscale Effects in Electrochemical Conversion: Coupling of Chemistry to Atomic- and Nanoscale Structure in Iron-Based Electrodes. *J. Am. Chem. Soc.* **2014**, *136*, 6211−6214.

(470) Goesten, M. G.; Stavitski, E.; Juan-Alcañiz, J.; Martiñez-Joaristi, A.; Petukhov, A. V.; Kapteijn, F.; Gascon, J. Small-Angle X-ray Scattering Documents the Growth of Metal-Organic Frameworks. *Catal. Today* **2013**, *205*, 120−127.

(471) Gilbert, J. A.; Kariuki, N. N.; Subbaraman, R.; Kropf, A. J.; Smith, M. C.; Holby, E. F.; Morgan, D.; Myers, D. J. In Situ Anomalous Small-Angle X-ray Scattering Studies of Platinum Nanoparticle Fuel Cell Electrocatalyst Degradation. *J. Am. Chem. Soc.* **2012**, *134*, 14823−14833.

(472) Chen, Z.; Higgins, D.; Yu, A.; Zhang, L.; Zhang, J. A Review on Non-Precious Metal Electrocatalysts for PEM Fuel Cells. *Energy Environ. Sci.* **2011**, *4*, 3167−3192.

(473) Gilbert, J. A.; Kropf, A. J.; Kariuki, N. N.; DeCrane, S.; Wang, X.; Rasouli, S.; Yu, K.; Ferreira, P. J.; Morgan, D.; Myers, D. J. In-Operando Anomalous Small-Angle X-Ray Scattering Investigation of Pt_3Co Catalyst Degradation in Aqueous and Fuel Cell Environments. *J. Electrochem. Soc.* **2015**, *162*, F1487−F1497.

(474) Wyrzgol, S. A.; Schafer, S.; Lee, S.; Lee, B.; Vece, M. D.; Li, X.; Seifert, S.; Winans, R. E.; Stutzmann, M.; Lercher, J. A.; et al. Combined TPRx, In Situ GISAXS and GIXAS Studies of Model Semiconductor-Supported Platinum Catalysts in the Hydrogenation of Ethene. *Phys. Chem. Chem. Phys.* **2010**, *12*, 5585−5595.

(475) Lee, S.; Vece, M. D.; Lee, B.; Seifert, S.; Winans, R. E.; Vajda, S. Oxidative Dehydrogenation of Cyclohexene on Size Selected Subnanometer Cobalt Clusters: Improved Catalytic Performance via Evolution of Cluster-Assembled Nanostructures. *Phys. Chem. Chem. Phys.* **2012**, *14*, 9336−9342.

(476) Winans, R. E.; Vajda, S.; Lee, B.; Riley, S. J.; Seifert, S.; Tikhonov, G. Y.; Tomczyk, N. A. Thermal Stability of Supported Platinum Clusters Studied by in Situ GISAXS. *J. Phys. Chem. B* **2004**, *108*, 18105−18107.

(477) Laoufi, I.; Saint-Lager, M. C.; Lazzari, R.; Jupille, J.; Robach, O.; Garaudée, S.; Cabailh, G.; Dolle, P.; Cruguel, H.; Bailly, A. Size and Catalytic Activity of Supported Gold Nanoparticles: An in Operando Study during CO Oxidation. *J. Phys. Chem. C* **2011**, *115*, 4673−4679.

(478) Chaâbane, N.; Lazzari, R.; Jupille, J.; Renaud, G.; Avellar Soares, E. CO-Induced Scavenging of Supported Pt Nanoclusters: A GISAXS Study. *J. Phys. Chem. C* **2012**, *116*, 23362−23370.

(479) Vajda, S.; Pellin, M. J.; Greeley, J. P.; Marshall, C. L.; Curtiss, L. A.; Ballentine, G. A.; Elam, J. W.; Catillon-Mucherie, S.; Redfern, P. C.; Mehmood, F.; et al. Subnanometre Platinum Clusters as Highly Active and Selective Catalysts for the Oxidative Dehydrogenation of Propane. *Nat. Mater.* **2009**, *8*, 213−216.

(480) Lee, S.; Molina, L. M.; López, M. J.; Alonso, J. A.; Hammer, B.; Lee, B.; Seifert, S.; Winans, R. E.; Elam, J. W.; Pellin, M. J.; et al. Selective Propene Epoxidation on Immobilized Au6−10 Clusters: The Effect of Hydrogen and Water on Activity and Selectivity. *Angew. Chem., Int. Ed.* **2009**, *48*, 1467−1471.

(481) Lei, Y.; Mehmood, F.; Lee, S.; Greeley, J.; Lee, B.; Seifert, S.; Winans, R. E.; Elam, J. W.; Meyer, R. J.; Redfern, P. C.; et al. Increased Silver Activity for Direct Propylene Epoxidation via Subnanometer Size Effects. *Science* **2010**, *328*, 224−228.

(482) Candelaria, S. L.; Shao, Y.; Zhou, W.; Li, X.; Xiao, J.; Zhang, J.-G.; Wang, Y.; Liu, J.; Li, J.; Cao, G. Nanostructured Carbon for Energy Storage and Conversion. *Nano Energy* **2012**, *1*, 195−220.

(483) Dierolf, M.; Menzel, A.; Thibault, P.; Schneider, P.; Kewish, C. M.; Wepf, R.; Bunk, O.; Pfeiffer, F. Ptychographic X-ray Computed Tomography at the Nanoscale. *Nature* **2010**, *467*, 436−439.

(484) Miao, J.; Ishikawa, T.; Robinson, I. K.; Murnane, M. M. Beyond Crystallography: Diffractive Imaging using Coherent X-ray Light Sources. *Science* **2015**, *348*, 530−535.

(485) Liebi, M.; Georgiadis, M.; Menzel, A.; Schneider, P.; Kohlbrecher, J.; Bunk, O.; Guizar-Sicairos, M. Nanostructure Surveys of Macroscopic Specimens by Small-Angle Scattering Tensor Tomography. *Nature* **2015**, *527*, 349−352.

(486) Schaff, F.; Bech, M.; Zaslansky, P.; Jud, C.; Liebi, M.; Guizar-Sicairos, M.; Pfeiffer, F. Six-Dimensional Real and Reciprocal Space small-Angle X-ray Scattering Tomography. *Nature* **2015**, *527*, 353−356.

(487) Stehle, R.; Goerigk, G.; Wallacher, D.; Ballauff, M.; Sieffert, S. Small-angle X-ray scattering in droplet-based microfluidics. *Lab Chip* **2013**, *13*, 1529−1537.

DOI: 10.1021/acs.chemrev.5b00690
Chem. Rev. XXXX, XXX, XXX−XXX